University of California
Los Angeles

Vortex-Based Aero- and Hydrodynamic Estimation

A dissertation submitted in partial satisfaction
of the requirements for the degree
Doctor of Philosophy in Mechanical Engineering

by

Maziar Sam Hemati

2013

ProQuest LLC.
789 East Eisenhower Parkway
P.O. Box 1346
Ann Arbor, MI 48106 - 1346

Abstract of the Dissertation

Vortex-Based
Aero- and Hydrodynamic Estimation

by

Maziar Sam Hemati

Doctor of Philosophy in Mechanical Engineering
University of California, Los Angeles, 2013
Professor Jeff D. Eldredge, Co-chair
Professor Jason L. Speyer, Co-chair

Flow control strategies often require knowledge of unmeasurable quantities, thus presenting a need to reconstruct flow states from measurable ones. In this thesis, the modeling, simulation, and estimator design aspects of flow reconstruction are considered. First, a vortex-based aero- and hydrodynamic estimation paradigm is developed to design a wake sensing algorithm for aircraft formation flight missions. The method assimilates wing distributed pressure measurements with a vortex-based wake model to better predict the state of the flow. The study compares Kalman-type algorithms with particle filtering algorithms, demonstrating that the vortex nonlinearities require particle filters to yield adequate performance. Furthermore, the observability structure of the wake is shown to have a negative impact on filter performance regardless of the algorithm applied. It is demonstrated that relative motions can alleviate the filter divergence issues associated with this observability structure.

In addition to estimator development, the dissertation addresses the need for an efficient unsteady multi-body aerodynamics testbed for estimator and controller validation studies. A pure vortex particle implementation of a vortex panel-particle method is developed to satisfy this need. The numerical method is demonstrated on the impulsive startup of a flat plate as well as the impulsive startup of a multi-wing formation. It is clear, from these validation studies, that the method is able to accommodate the unsteady wake effects that arise in formation flight missions.

Lastly, successful vortex-based estimation is highly dependent on the reliability of the low-order vortex model used in representing the flow of interest. The present treatise establishes a systematic framework for vortex model improvement, grounded in optimal control theory and the calculus of variations. By minimizing model predicted errors with respect to empirical data, the shortcomings of the baseline vortex model can be revealed and reconciled. Here, the method is demonstrated on an impulse matching model for canonical unsteady wing maneuvers and reveals the shortcomings of the Kutta condition in such flows. The resulting analysis sheds light on the governing physical processes and provides guidance for model improvement for the unsteady aerodynamics associated with these canonical wing maneuvers.

The dissertation of Maziar Sam Hemati is approved.

Andrea L. Bertozzi
John Kim
Jason L. Speyer, Committee Co-chair
Jeff D. Eldredge, Committee Co-chair

University of California, Los Angeles
2013

“Vortices of pure energy can exist and, if my theories are right, can compose the bodily form of an intelligent species.”

—Sir William Thomas, 1st Baron Kelvin

Table of Contents

1 Introduction **1**

1.1 Flow Control 2

1.2 Reduced Order Modeling 3

1.2.1 Mathematical ROM 4

1.2.2 Physics-Based ROM 7

1.3 Vortex-Based Aero- and Hydrodynamic Estimation 8

1.4 Overview of Contributions 11

2 Aero- and Hydrodynamics **13**

2.1 The Navier-Stokes Equations and the Euler Limit 13

2.2 Flow Kinematics 14

2.2.1 Helmholtz Decomposition 14

2.2.2 Biot-Savart Law 15

2.2.3 Line Vortices 16

2.3 Flow Kinetics and Vorticity Transport 17

2.4 Kelvin-Helmholtz Theorems 19

2.5 Vortex Sheets 20

2.6 Kutta Condition and Vorticity Shedding 23

3 Vortex Model Optimization **25**

3.1 Introduction 26

3.2 Vortex Model Formulation 28

3.2.1 Complex Potential: System of Vortices in the Presence of a Flat Plate 28

3.2.2 Force on the Plate 30
3.2.3 Impulse Matching Model 31
3.3 A Variational Approach to Vortex Model Improvement 32
3.3.1 Constrained Optimization Formulation 33
3.3.2 Method of Solution 34
3.3.3 True Force Histories: High-Fidelity Viscous Vortex Particle Simulation 35
3.4 Results and Discussion 36
3.4.1 Pitching Kinematics 36
3.4.2 Impulsive Translation 43
3.5 Remaining Challenges and Paths to Enhancement 54
3.5.1 Convergence for Large Time Windows and Early Times 54
3.5.2 Extending Time Windows via Stitching 58
3.5.3 A Framework for Subsequent Vortex Shedding 59
3.5.4 Distilling a Modified Kutta Condition 65
3.6 Conclusions 66

4 Simulation Testbed: A Vortex Panel-Particle Method 73
4.1 Coordinate Systems 73
4.2 The Mathematical Problem 74
4.3 Discretization of Vortex Sheets 77
4.3.1 Vortex Particle Representation of Line Vortex Segments 79
4.4 Unsteady Trailing Edge Kutta Condition 80
4.5 Wake Modeling 82
4.6 Aerodynamic Loads 83
4.7 Code Validation 84

4.7.1 Simulation Specifications . . . 85
4.7.2 Impulsive Start of a Flat Plate . . . 85
4.7.3 Impulsive Start of a Two Flat Plate Formation . . . 85
4.8 Conclusions . . . 88

5 Nonlinear Estimation and Filtering . . . 91
5.1 Kalman Filtering . . . 93
5.1.1 Linear Kalman Filtering . . . 93
5.1.2 Extended Kalman Filtering . . . 95
5.1.3 Variations of Extended Kalman Filtering . . . 97
5.2 Bayesian Estimation . . . 98
5.2.1 Particle Filtering . . . 100
5.3 Bias and Divergence Issues . . . 103
5.3.1 Modeling Errors . . . 104
5.3.2 Observability Problems . . . 104

6 Wake Estimation for Formation Flight . . . 105
6.1 Introduction . . . 106
6.2 Aerodynamic Modeling . . . 109
6.2.1 Lead Aircraft and Wake Representation . . . 109
6.2.2 Trailing Aircraft Representation . . . 111
6.3 Wake Observability . . . 116
6.3.1 System Observability and Conditioning . . . 117
6.3.2 Lifting Line Based Measurement Jacobian . . . 118
6.3.3 Wake Observability and Conditioning Comparison . . . 122

6.4 Wake Estimation Algorithm 124
6.4.1 States and Measurements 125
6.4.2 Measurement and Process Noise 126
6.4.3 Kalman-Type Filtering: Measurement Function Linearization 126
6.4.4 Particle Filtering Procedure 127
6.4.5 Offline Calibration 127
6.4.6 System Dynamics 128
6.5 Performance Results and Discussion 129
6.5.1 Two-Aircraft Static Configuration 132
6.5.2 Two-Aircraft with Relative Motions 135
6.6 Conclusions 136

7 Conclusions and Future Directions 151

References 154

List of Figures

2.1 Vortex Sheet 20

3.1 Schematic of mapping from physical plane to circle plane 29

3.2 Comparison of force histories by various methods 32

3.3 Schematic of pitching wing 36

3.4 Pitching plate ($K = 0.2$) force histories 39

3.5 Pitching plate ($K = 0.2$) optimal input histories 40

3.6 Pitching plate ($K = 0.2$) vortex strength histories 40

3.7 Pitching plate ($K = 0.2$) vortex trajectories 41

3.8 Pitching plate ($K = 0.2$) streamlines 42

3.9 Pitching plate ($K = 0.7$) force histories 43

3.10 Pitching plate ($K = 0.7$) optimal input histories 44

3.11 Pitching plate ($K = 0.7$) vortex strength histories 44

3.12 Pitching plate ($K = 0.7$) vortex trajectories 45

3.13 Pitching plate ($K = 0.7$) streamlines 46

3.14 Impulsively translating plate ($\alpha = 10^o$) force histories 47

3.15 Impulsively translating plate ($\alpha = 10^o$) optimal input histories 48

3.16 Impulsively translating plate ($\alpha = 10^o$) vortex strength histories 48

3.17 Impulsively translating plate ($\alpha = 10^o$) vortex trajectories 49

3.18 Impulsively translating plate ($\alpha = 10^o$) streamlines 50

3.19 Impulsively translating plate ($\alpha = 45^o$) force histories 51

3.20 Impulsively translating plate ($\alpha = 45^o$) optimal input histories 51

3.21 Impulsively translating plate ($\alpha = 45^o$) vortex strength histories 52

3.22 Impulsively translating plate ($\alpha = 45^o$) vortex trajectories 52

3.23 Impulsively translating plate ($\alpha = 45^o$) streamlines 53

3.24 Impulsively translating plate ($\alpha = 90^o$) force histories 54

3.25 Impulsively translating plate ($\alpha = 90^o$) optimal input histories 55

3.26 Impulsively translating plate ($\alpha = 90^o$) vortex strength histories 55

3.27 Impulsively translating plate ($\alpha = 90^o$) vortex trajectories 56

3.28 Impulsively translating plate ($\alpha = 90^o$) streamlines 57

3.29 Time window decomposition for the stitching procedure 59

3.30 Pitching plate ($K = 0.2$) stitch-optimized force histories 60

3.31 Pitching plate ($K = 0.2$) stitch-optimized input histories 60

3.32 Pitching plate ($K = 0.2$) stitch-optimized strength histories 61

3.33 Pitching plate ($K = 0.7$) stitch-optimized force histories 61

3.34 Pitching plate ($K = 0.7$) stitch-optimized input histories 62

3.35 Pitching plate ($K = 0.7$) stitch-optimized strength histories 62

3.36 Stagnation point specification for a pitch-up maneuver ($K = 0.2$) 67

3.37 Stagnation point specification for a pitch-up maneuver ($K = 0.7$) 68

3.38 Stagnation point specification for impulsive translation ($\alpha = 45^o$) 69

3.39 Stagnation point specification for impulsive translation ($\alpha = 90^o$) 70

4.1 Vortex Sheet Discretization 78

4.2 Rolled-Up Wake of a Flat Plate 86

4.3 Flat Plate Transient Lift Comparison 86

4.4 Flat Plate Transient Induced Drag Comparison 87

4.5 Flat Plate Transient Induced Drag Comparison (Zoomed-In) 88

4.6 Rolled-Up Wake of a Two Flat Plate Formation 89

4.7 Transient Lift and Induced Drag Curves of a Two Flat Plate Formation . . . 90

5.1 Kalman Filter Block Diagram 94
5.2 Particle Filter Block Diagram 102
5.3 Resampling by Cumulative Sum of Weights (CSW) 103

6.1 Rotation of Force Vector in Formation Flight 105
6.2 Wake Vortex Coordinate System 111
6.3 Lifting Line Coordinate System 112
6.4 Augmented Lifting Line Coordinate System 115
6.5 Observability Conditioning Based on Various Sensor-Types 123
6.6 Vortex Lattice Aircraft Configuration 132
6.7 EKF: Static Wake Simulation Results (Case 1) 139
6.8 EKF: Static Wake Simulation Results (Case 2a) 140
6.9 EKF: Results from Multiple Initial Estimates (Case 2a) 141
6.10 IEKF: Static Wake Simulation Results (Case 2b) 142
6.11 IEKF: Results from Multiple Initial Estimates (Case 2b) 143
6.12 SOEKF: Static Wake Simulation Results (Case 2c) 144
6.13 SOEKF: Results from Multiple Initial Estimates (Case 2c) 145
6.14 PF: Static Wake Simulation Results (Case 2d) 146
6.15 PF: Results from Multiple Initial Estimates (Case 2d) 147
6.16 EKF: Relative Motion Simulation Results (Case 3) 148
6.17 EKF: Relative Motion Simulation Results (Case 4a) 149
6.18 EKF: Relative Motion Simulation Results (Case 4b) 150

LIST OF TABLES

6.1 Specifications of Cases Studied 131

ACKNOWLEDGMENTS

First and foremost, I would like to thank my advisors Professors Jeff Eldredge and Jason Speyer for their intellectual and personal guidance. Both have challenged me as a scholar, taught me many valuable lessons, and made themselves available on countless occasions. Thank you both for all of your support. Of course, I thank my committee members for their participation in the process. I will single out Professor John Kim for introducing me to fluid mechanics in an undergraduate classroom in the Spring of 2005. Additionally, I am indebted to Professors Sungtaek Ju and Pirouz Kavehpour who were generous enough to introduce me to university research early in my academic career. Special thanks to all of my labmates, past and present, who made everyday of this endeavor enjoyable, even when times got tough.

Funding and support, in varying capacities, were graciously provided by the Air Force Office of Scientific Research, DARPA, The Boeing Company, SySense Incorporated, and UCLA. Stefan Bieniawski and Brian Whitehead, of The Boeing Company, were considerably helpful with inputs and discussions during my involvement on the autonomous formation flight project. I would especially like to thank Professor Don Browne for providing me numerous opportunities to grow as a teacher and for continuously lending an ear and advice when it was most needed.

A special thanks to the UCLA Cycling Team for getting me away from my desk and up into the Santa Monica Mountains. Rail and Bail! Los Angeles has never felt the same since I began experiencing it from on two wheels. Thank you David, Nina, and Scott (a.k.a Dr. Pain and the Pain Train) for dragging me out of bed during the cold dark mornings and for the the much needed encouragement during all those grueling climbs.

Thank you to my friends and family. To my closest friends—you know who you are—these years would not have been nearly as fun without all the antics. Neda, you have been nothing short of inspirational over the last decade. You have experienced my journey by proxy, and I could not have done it without you. Finally, thank you mom and dad. Your unwavering support and guidance have been instrumental in my success and happiness.

Vita

2003	High School Diploma, Saratoga High School, Saratoga, CA.
2004–2005	Undergraduate Researcher, Multiscale Thermosciences Laboratory, Department of Mechanical and Aerospace Engineering, UCLA.
2005–2006	Associate Engineer, Northrop Grumman, Marine Systems, Sunnyvale, CA.
2005–2007	Undergraduate Researcher, Complex Fluids and Interfacial Physics Laboratory, Department of Mechanical and Aerospace Engineering, UCLA.
2007	B.S. (Aerospace Engineering), UCLA, Los Angeles, California.
2007	Associate Guidance, Navigation, and Control Engineer, The Aerospace Corporation, El Segundo, CA.
2007–2013	Graduate Student Researcher, SOFIA Laboratory, Department of Mechanical and Aerospace Engineering, UCLA.
2007–2012	Advanced Algorithms Engineer, SySense, Inc., El Segundo, CA.
2007–2008	First-Year Departmental Fellow, Department of Mechanical and Aerospace Engineering, UCLA.
2008	Teaching Assistant, Department of Mechanical and Aerospace Engineering, UCLA. Taught sections for MAE 153A (Engineering Acoustics) and MAE 154S (Flight Mechanics, Stability, and Control of Aircraft).
2009	M.S. (Mechanical Engineering), UCLA, Los Angeles, CA.

2009–2011	Teaching Associate, Henry Samueli School of Engineering and Applied Sciences, UCLA. Taught sections for ENGR 183 (Engineering and Society) and ENGR 185 (The Art of Engineering Endeavors), team oriented courses in engineering ethics and technical communication.
2011–2013	Teaching Assistant Consultant, Department of Mechanical and Aerospace Engineering, UCLA.
2012–2013	Dissertation Year Fellow, UCLA.

PUBLICATIONS

Aircraft Wake Sensing
Maziar S. Hemati, Jeff D. Eldredge, and Jason L. Speyer
AIAA Paper 2012-4768
August 2012

Improving Vortex Models via Optimal Control Theory
Maziar S. Hemati, Jeff D. Eldredge, and Jason L. Speyer
AIAA Paper 2013-0351
January 2013

Aircraft Wake Sensing
Maziar S. Hemati, Jeff D. Eldredge, and Jason L. Speyer
Submitted to Journal of Guidance, Control, and Dynamics
2013

CHAPTER 1

Introduction

Flow control, the notion of using active and passive devices to control the state of a flow field, has the potential to surmount hurdles in areas where traditional engineering methods have provided meager solutions. Some of the needs to be addressed by flow control are drag reduction in air, ground, and maritime transportation systems, efficient power harvesting in wind turbines and wind farms, as well as defense strategies against biological and chemical terrorist attacks [TN11]. Though the potential and promise of such technology is great, development of control strategies and algorithms for real-world applications is currently limited due to the high-dimensionality of fluid mechanical systems. Additionally, practical control strategies often rely upon knowledge of unmeasurable states of a system, thus presenting the need to reconstruct these states from the measured ones. Finally, all of this must be conducted in a world filled with uncertainty; our physical models live in the realm of determinism, whereas the real-world presents us with stochasticity.

The present work considers aero- and hydrodynamical systems in which vortical structures are dominant and the assumptions of potential flow are relevant. Attention is given to the task of low-order modeling by means of simple vortex entities, where “low” refers to a dimensionality sufficiently small for controller design and real-time implementation. These low-order models are then used in the development of vortex estimation algorithms, in which the state of a flow is predicted by assimilating a sequence of noisy sensor measurements with a vortex model developed for the system of interest. The vortex estimator predicts the strengths and locations of all the vortex elements, thus defining the state of the flow at a given instant. In turn, this information enables a flow control system to determine the proper actuation to achieve a desired outcome.

1.1 Flow Control

Flow control is the notion of achieving a desired objective as a function of space and time by some means of flow manipulation [Gad00]. For example, the desired objective function may be drag reduction, delayed separation, mixing enhancement, increased lift, or noise suppression. Methods by which these objectives may be achieved can be separated into three categories:

1. Passive Flow Control
2. Active (i.e. Open-Loop) Flow Control
3. Reactive (i.e. Closed-Loop with Feedback) Flow Control

Although passive flow control techniques generally have the advantage of being less costly, less bulky, and less complex than active and reactive strategies, they cannot respond to changes in the flow state. As such, they are often less effective in comparison to active and reactive strategies.

Active and reactive flow control implementations, on the other hand, tend to be more expensive and complex because they require appropriate actuation to inject energy into the flow as a means of achieving the desired outcome. Reactive strategies tend to be more complex than active strategies because they make use of measurements to infer changes in the flow state. Accounting for changes in the states allows for greater robustness to both internal and external disturbances. Unfortunately, the states of fluid-mechanical systems are often not directly accessible for measurement and must be estimated in some manner (e.g. by means of nonlinear stochastic estimation schemes). Applying these schemes through high-fidelity simulations is impractical due to time restrictions in real-time applications. These restrictions motivate the development of reduced order models for use within reactive flow control schemes.

Reduced order descriptions of a system are not always effective in accurately simulating a flow; however, they do tend to be useful in the design and implementation of flow control and estimation strategies. It is useful to note that the model employed in the design of a control system does not need to capture all of the fine details of a flow [KB07]. Instead, the model needs to provide a sufficient input-output relation for the system and its influence on the cost function used in measuring the system's optimal state.

Vortex-based aero- and hydrodynamic estimation is motivated by the fact that simple vortex representations can, often times, adequately approximate vortex dominated flows. Such representations provide one means of reliable real-time estimation and merit further investigation. The present treatise addresses the notion of vortex-based flow estimation by considering the modeling, simulation, and estimation of several vortex dominated flows in a variety of application areas.

1.2 Reduced Order Modeling

The Navier-Stokes equations are a class of infinite-dimensional partial differential equations that often times possess no closed-form solution. Even when these flows are discretized for numerical simulation, they represent very high-dimensional systems. It is this inherent high-dimensionality of fluid mechanical systems that leads to difficulties in both analyzing and understanding them. Moreover, there are few mathematical tools at our disposal in analyzing infinite-dimensional systems, whereas there is a large set of methods available for the analysis of low-order, finite-dimensional systems. As such, it is reasonable to consider methods for reducing the solutions of fluid mechanical flows to relatively low-dimensional spaces in the interest of understanding, analyzing, and controlling such phenomena. Reduced order modeling (ROM) is a rich area of research in many varying disciplines and, in general, can be classified into two different paradigms or methods of approach:

1. Mathematical ROM

2. Physics-Based ROM

The objective of any form of model order reduction is to reduce the expense associated with solving the governing equations while capturing the essential physics at play. The degree to which this physics must be captured is dictated by the final application and varies from problem to problem.

1.2.1 Mathematical ROM

A typical mathematical approach to ROM begins with access to input-output data from the system of interest. An appropriate set of basis functions is determined and the flow-field is represented as a linear combination of these basis functions. The order of the model is finally reduced by projecting the flow-field onto a truncated set of these basis functions in some manner. One such approach, which has become fairly common in the fluid mechanics literature, ever since Lumley introduced it in the context of turbulence in 1967 [HLB97], is to use the proper orthogonal decomposition (POD) in conjunction with the Galerkin projection. A notable short-coming of this method, and many others like it, is that the most energetic POD modes (i.e. the ones of interest in POD approaches to ROM) are not necessarily the most important modes in terms of the underlying physics of the flow. As a result, such methods only have a limited use for flow control applications.

One means of overcoming this issue is to consider a Balanced POD (BPOD) formulation, where the controllability and observability characteristics of the resulting system are "balanced." BPOD was first considered in the context of fluid mechanical systems in [Row05] and has been successful in a variety of fluid mechanical applications. An example of BPOD in flow control and estimation applications can be found in [AR10]. In the paper, Ahuja and Rowley developed an algorithm for constructing reduced-order models of input-output dynamics of *unstable* state-space representations of the linearized Navier-Stokes equations with actuation and sensing. They successfully demonstrated their algorithm by stabilizing the unstable steady states of a two-dimensional low Reynolds number flow past a flat plate at large angles of attack via estimator-based control. The estimation scheme consisted of a reduced-order Kalman filter, which estimated the velocity-field from measurements of vertical velocity taken at various sensor locations. The velocity-field reconstruction was fed-back to the linear quadratic regulator (LQR) controller to determine the necessary actuation in the form of localized body forcing near the trailing edge of the flat plate. The model used in the Kalman filter was the *linear* ROM developed through balanced truncation of the POD modes, while the nonlinear aspects of the dynamics were modeled as white noise processes. The authors acknowledge the limitations of this approach and suggest future research be conducted on algorithms for computing *nonlinear* balanced modes. Nonetheless, they demonstrated successful results in their simulations.

Ahuja and Rowley cite extensive research on controlling the flow past a cylinder using both open-loop and closed-loop control strategies. They compare their algorithm for ROM development to other POD-type methods, noting the advantages of BPOD. The authors report that BPOD improves upon traditional POD schemes, having extended it to be valid for unstable state-space systems. Despite the improved performance over traditional POD approaches, the authors note the complexity of their algorithm as a disadvantage. They claim that their approach requires adjoint simulations which can be expensive and are often times unavailable. Although the computational expense of BPOD can make the method impractical in certain application area, it has been demonstrated that the Eigensystem Realization Algorithm (ERA) can replicate the BPOD modes with enhanced computational efficiency. This arises because ERA performs adjoint-free balancing (i.e. it does not require access to adjoint simulations), which also makes the approach suitable for extracting low-order models from experimental data. The interested reader may consult [HLB12], [NMT11], and citations therein for additional developments of POD, BPOD, ERA, and Galerkin methods as well as discussions of their application in the context of flow control.

In addition to the Ahuja and Rowley study, many others have considered the closed-loop control of bluff bodies. Among them, many have used various methods of mathematical ROM with a fair amount of success [NAM03, TLN11, LLN05, LTL06]. One study that takes a slightly different approach from the mathematical ROM methods discussed here comes from Anderson et al., who use a system identification algorithm to determine a mathematical input-output representation of the flow [ACG00]. A vortex blob method is used to simulate flow about a flat plate oriented perpendicular to the flow direction. The wake is modeled by an evolving set of regularized point vortices, which are shed according to an unsteady Kutta condition. An auto-regressive with exogenous input (ARX) model is identified from the hydrodynamic simulation to provide a discrete-time input-output description of the system. The ARX model is constructed with various degrees of dimensionality (i.e. $n = 3$ to 30), while the final model is chosen such that its frequency response best fits the frequency response of the vortex simulation. The authors note that the ARX model must be reconstructed every time the sensor configuration changes, but also point out that the method can be used to guide the placement of sensors. As demonstrated in the paper, suitable control laws can also be designed around models developed by means of system identification practices.

Due to its promise in better handling nonlinear systems, a final remark must be made about the application of Dynamic Mode Decomposition (DMD) to fluid mechanical systems. DMD approximates a linear infinite-dimensional operator, known as the "Koopman operator," which is able to represent nonlinear finite-dimensional dynamics without linearization. In essence, the method leads to a linear model that is capable of approximating the nonlinear dynamics of the system under consideration. Chen et al. successfully demonstrate DMD on the two-dimensional flow over a cylinder in [CTR12]. In comparing the resulting DMD model with empirical data, the authors report success in extracting salient systems attributes. Despite the positive results reported, there remains much work to be done in applying DMD to fluid mechanical systems. The method shows a great deal of promise and will likely become a prominent tool for mathematical ROM in the future.

Mathematical ROM for fluid mechanical systems has come a long way since its inception. It is clear that despite all of the progress, there is still much work to be done. However, such methods seem to provide a viable approach by which to model flows for control and estimation applications. They also provide an alternative perspective to the physics-based ones engineers are accustomed to, thus providing additional insights to physics which may have otherwise been overlooked.

1.2.2 Physics-Based ROM

Physics-based approaches to ROM are one that are more familiar. Many of the techniques common in fluid dynamic analysis can be classified as physics-based approaches. For example, each of the following models can be implemented to approximate the full Navier-Stokes equations and provide insight into a specific flow under an appropriate set of conditions:

- Potential flow analysis
- Boundary layer equations
- Euler equations
- Reynolds Averaged Navier-Stokes (RANS) simulations
- Large Eddy Simulations (LES)

Physics-based ROMs come about by neglecting certain physical processes, deemed unimportant for the physics being modeled. The choice to model a given flow as incompressible or compressible provides a good example of this notion. The modeler's physical intuition of a given process or system can allow simplification of the governing equations without losing considerable accuracy in the solution, under the appropriate conditions. Vortex-based methods fall under the physics-based classification of reduced order modeling paradigms. It is the engineer's job to determine when the application of such models is appropriate in the context of a given problem. The following section provides a brief review of studies to date on vortex-based ROMs for use in state estimation and control for fluid mechanical systems.

1.3 Vortex-Based Aero- and Hydrodynamic Estimation

The primary objective of the current work is to develop a framework for estimating the state of a vortex dominated flow by means of vortex models. By estimating the dynamical state of the vortex system modeling the flow, a control scheme can be designed to achieve a desired objective. The basis of the methods considered in this treatise combines existing algorithms from nonlinear stochastic estimation theory with physically motivated vortex models used in aero- and hydrodynamic analysis.

The first consideration of vortex-based control and estimation was made by Cortelezzi et al. in formulating a strategy for actively controlling the circulation associated with a semi-infinite plate [CLD94]. The authors chose to model the rolled-up shear layer as a point vortex with time-dependent strength, predicted by an unsteady Kutta condition. The transverse motion of the plate was used for actuation. The team also considered the problem of vortex detection and developed a strategy for estimating the location and strength of the vortex based on measurements of the velocity-field near the tip of the flat plate. The estimation method makes use of conformal transformations to directly invert the velocity-field into the vortex parameters. Such an approach is typically unreliable in the presence of noise and uncertainty. The study tested the control strategy using the same aerodynamic model for simulation as was used to derive the controller, meaning that considerations of modeling error and noise were not accounted for. The performance results attained from more realistic simulation environments and experiments are, therefore, not guaranteed to match those presented in the paper due to the potential mismatch between model and truth signals. Nonetheless, this study engendered interest in the notion of vortex-based methods for flow control and estimation.

In 2002, Vainchtein and Mezić considered the problem of controlling the position of a point vortex using a strain-field or a single point source/sink [VM02]. The authors invoked singular control methods and dynamical system perturbation theory in the controller design, assuming full state-feedback. No consideration was given to the estimation problem in the development of their optimal control law, making practical considerations quite dubious.

A couple of years later, Noack et al. developed a control strategy to optimize mixing through the use of a point vortex model [NMT04]. Their control strategy aimed to maximize the flux across the recirculation zone under the side-constraints of bounded vortex motion and bounded actuation. The authors maintain that their controller "requires knowledge of the vortex position at all times." As a result, the team designed a local observer to estimate the vortex position from a single-component fluid velocity sensor near the wall. The authors point out that "a global observer is difficult to construct because of the level of nonlinearity in the vortex model." Their observer was designed for operation in the neighborhood of the equilibrium point. There is no doubt that the control strategy would benefit from a global vortex estimation scheme.

Much research on vortex-based data assimilation techniques has come from the atmospheric and oceanic science communities. Many researchers have considered Lagrangian approaches to vortex estimation. For example, Kuznetsov et al. present a technique for assimilating Lagrangian tracer positions, observed at discrete times, to augment a flow model by means of an extended Kalman filter (EKF) [KIJ03]. The method is tested on several different point vortex flows with varying degrees of complexity. Their numerical experiments demonstrate successful tracking for specific configurations; however, it is reported that the filter's performance "strongly depends on initial tracer positions." Further analysis shows that the initial tracer positions leading to good filter behavior are separated from those leading to poor performance by Lagrangian flow structures, specifically by the separatrices or invariant manifolds of the velocity-field.

Systems of two and four point vortices, subject to stochastic forcing, were tracked by a combination of Lagrangian vortex position observations and Eulerian fluid velocity observations at a set of fixed points in free-space in the papers of Ide and Ghil [IG97a, IG97b]. An EKF was used to assimilate measurements with the point vortex model. The authors report excellent tracking "when initial data are properly given and (Lagrangian) vortex observations are made frequently," [IG97a]. There is no doubt that Lagrangian observations of the vortex improve the EKF performance because such observations tend to orbit the vortex cores, more or less "telling" the filter where the vortices are positioned. Unfortunately, Lagrangian observations are generally not available in most engineering applications; however, such notions may be useful for particle image velocimetry (PIV) experiments. Such considerations are outside the scope of this work, so no further development will be made in the area of Lagrangian observations, though the general improvements in filter performance by such means is important to note.

Some researchers have also considered improving existing estimates for hurricane position and strength from legacy atmospheric forecasting models by assimilating the legacy models with vortex estimation paradigms. For example, Chen et al. use an ensemble Kalman filter (EnKF) to improve estimates of hurricane position using knowledge of its vorticity-field [CS06]. The observation operator $\mathcal{H}$ acts on the vorticity-field, obtained from satellites, to provide measurements associated with an elliptic vortex. The group considered cases of increasing complexity. In some scenarios, only the vortex centroid was measured (i.e. a point vortex position was measured from the vorticity-field). In the higher-order models, the satellite data was used to fit an elliptic vortex defined by its major and minor axes as well as its rotational angle with respect to a global coordinate frame. In addition to position, shape, and orientation, the vorticity-field can be used to provide measurements of the vortex strength. The researchers reported improvements in estimating hurricane characteristics by applying these strategies, especially the ones with higher-order vortex descriptions.

The most noteworthy work in vortex-based estimation, based on its semblance to the approaches considered in the present study, comes from Suzuki and Colonius [SC03]. They apply a least-squares algorithm to estimate the position and strength of a single vortex convected in a channel. An array of pressure sensors distributed along the channel walls provides measurements for the correction step of their algorithm. The scheme uses a simple point vortex model with conformal transformations to model the channel walls. The algorithm's detection and tracking of the vortex in direct numerical simulations (DNS) proves successful. The authors also report success in detecting two vortices in a curvilinear channel. However, it is noted that “the algorithm for multiple vortices indicates that finding the optimum parameters becomes more sensitive to the initial values as the number of parameters increases.” The authors also point out the promise of vortex detection over other techniques such as POD.

> Active flow control techniques suffer from obtaining reduced order representations of the flowfields. Flow reconstruction techniques, such as the proper orthogonal decomposition or the stochastic estimation [*sic*], can characterize unsteady flow patterns; however, they require the information of the entire flowfield in most cases. In contrast, when the key structures of the flowfield are somewhat known this inverse algorithm can reconstruct an approximate flowfield only from the information on the boundary [SC03].

This statement is in line with the aspirations of the current work, though here we demonstrate that “the stochastic estimation” can be a reliable means of flow reconstruction from boundary information. If a reliable vortex-based aero- and hydrodynamic estimation paradigm can be developed, then certain classes of fluid flows can be reconstructed for use in feedback control schemes for flow control applications.

More extensive discussions of existing work in vortex-based methods for control and estimation can be found in the 2008 review paper by Protas [Pro08]. In the following section, the specific contributions of this dissertation to the state-of-the-art in modeling, simulation, and algorithm development for vortex-based aero- and hydrodynamic estimation are outlined.

1.4 Overview of Contributions

This dissertation contributes to the state-of-the-art in a number of areas important to vortex-based aero- and hydrodynamic estimation. The primary contributions are as follows:

- Developed a systematic framework for vortex model improvement and optimization grounded in optimal control theory and the calculus of variations.

- Optimized the Eldredge-Wang impulse matching model for canonical unsteady wing maneuvers and showed that a two point vortex model can accurately predict the force response of a maneuvering wing.
- Highlighted the shortcomings of applying a Kutta condition at both the leading and trailing edges in flows with leading and trailing edge vortex evolution.
- Developed a pure vortex particle implementation of the vortex panel-particle method that requires only a single invocation of a fast multipole solver at each time-step, thus leading to reduced computational time.
- Devised a vortex-based strategy for wake sensing by means of distributed aerodynamic sensor measurements for use in aircraft formation flight missions.
- Identified and reconciled causes of filter bias and divergence in the vortex estimation problem by studying Kalman-type and Bayesian estimation algorithms.

The present dissertation begins by reviewing fundamental aero- and hydrodynamic theory in Chapter 2. Chapter 3 focuses on the development and implementation of a novel framework for vortex model optimization. This framework can be classified as a hybrid mathematical/physics-based approach for reduced order modeling, and is introduced in the context of a vortex model for flapping wing aerodynamics. A numerical testbed for unsteady multi-body aerodynamics, namely the vortex panel-particle method, is developed in Chapter 4. This testbed provides an efficient, yet accurate, environment for validating vortex-based estimator performance. A brief summary of nonlinear estimation and filtering theory follows in Chapter 5, mainly focused on outlining specific filtering paradigms and algorithms to be used in Chapter 6. Various aspects of vortex-based aero- and hydrodynamic estimation are presented in the context of wake sensing for aircraft formation flight in Chapter 6. Finally, Chapter 7 summarizes the main conclusions drawn in the dissertation and identifies future directions for research.

CHAPTER 2

Aero- and Hydrodynamics

Classical aerodynamic theory is an essential tool in the modeling and analysis of aircraft and modern hydrodynamic systems. In the present section, a brief review of relevant topics is introduced. It is assumed that much of the material to be presented is already familiar to the reader. A majority of the discussion pertaining to vortex elements (e.g. point and line vortices) is necessary in constructing the vortex models used within the context of low-order aero- and hydrodynamic modeling, which are a basis for vortex-based state estimation. Additional material presented should serve as a primer of classical aerodynamic theory essential to the development of the panel-particle method discussed in Chapter 4. The reader with a strong background in classical aero- and hydrodynamics may wish to skip over this chapter and return to it only as necessary.

2.1 The Navier-Stokes Equations and the Euler Limit

The continuity and Navier-Stokes equations for an incompressible fluid

$$\nabla \cdot \mathbf{u} = 0 \tag{2.1}$$

$$\frac{\partial \mathbf{u}}{\partial t} + (\mathbf{u} \cdot \nabla)\mathbf{u} = -\frac{1}{\rho}\nabla p + \nu \nabla^2 \mathbf{u} + \mathbf{f} \tag{2.2}$$

form a set of four scalar differential equations for the unknowns $\mathbf{u}(\mathbf{x}, t)$ and $p(\mathbf{x}, t)$, provided that appropriate initial and boundary conditions are known. For problems of aero- and hydrodynamic interest, the “no-slip” condition is most commonly employed. For problems involving an infinite domain, conditions at infinity must also be specified.

2.2 Flow Kinematics

The kinematic problem is one of relating the velocity and vorticity fields to one another. This can be done by invoking the continuity equation (2.1) and the definition of vorticity (2.21). It is useful to emphasize that this is purely a kinematic relation. Although the term "induce" is typically used in describing the velocity field associated with a given vorticity field, no actual cause and effect is implied; both the velocity and vorticity field coexist and are simply different representations of the same flow.

2.2.1 Helmholtz Decomposition

In fluid mechanics, the Helmholtz decomposition is often used to decompose the velocity field into the so-called *scalar* and *vector potentials* (i.e. ϕ and $\boldsymbol{\psi}$, respectively). The Helmholtz decomposition is characterized as a decomposition of a vector field into an irrotational part (i.e. curl-free) and a solenoidal part (i.e. divergence-free)

$$\mathbf{u}(\mathbf{x}, t) = \nabla\phi + \nabla \times \boldsymbol{\psi}. \tag{2.3}$$

Since $\mathbf{u}$ is composed of three independent components, we choose ϕ to represent one of them, and constrain $\boldsymbol{\psi}$ such that it has only two independent variables. This constraint equation, sometimes referred to as a "gauge condition," is for the vector potential to be divergence-free

$$\nabla \cdot \boldsymbol{\psi} = 0. \tag{2.4}$$

Taking the divergence and curl of (2.3) and accounting for this gauge condition yields the two Poisson equations

$$\nabla^2\phi = \vartheta \tag{2.5}$$

$$\nabla^2\boldsymbol{\psi} = -\boldsymbol{\omega} \tag{2.6}$$

which can be solved for ϕ and $\boldsymbol{\psi}$ for a specified ϑ and $\boldsymbol{\omega}$, respectively, under the appropriate set of boundary conditions. Of course, the first of these reduces to Laplace's equation for the scalar potential in incompressible flows, since the dilatation rate is zero (i.e. $\vartheta = 0$ in incompressible flow). This can be seen by substituting (2.3) into the continuity equation (2.1):

$$\begin{aligned} \nabla \cdot \mathbf{u} &= 0 \\ \nabla \cdot (\nabla \phi + \nabla \times \boldsymbol{\psi}) &= 0 \\ \nabla \cdot \nabla \phi &= 0 \\ \nabla^2 \phi &= 0 \end{aligned} \tag{2.7}$$

We are left with a Laplace equation and a Poisson equation to be solved in determining the resultant velocity field.

2.2.2 Biot-Savart Law

The kinematic relationship from vorticity to velocity is commonly referred to as the "Biot-Savart law" due to its analogy with the law of the same name in the field of electromagnetics. It allows the velocity field to be reconstructed from a given vorticity field. The Biot-Savart law can be derived by beginning with the Green's function solution to the vorticity-streamfunction Poisson equation which can be expressed as [Mar01]

$$\boldsymbol{\psi}(\mathbf{x}, t) = -\int_V G(\mathbf{x} - \mathbf{x}')\boldsymbol{\omega}(\mathbf{x}', t)\mathrm{d}v' \tag{2.8}$$

where the Green's function for the Possion equation is

$$G(\mathbf{r}) = \begin{cases} \frac{1}{2\pi}\ln(r) & \text{for } r \in \mathbb{R}^2 \\ -\frac{1}{4\pi r} & \text{for } r \in \mathbb{R}^3 \end{cases} \tag{2.9}$$

with $\mathbf{r} = \mathbf{x} - \mathbf{x}'$ and $r = |\mathbf{r}|$. Taking the curl of both sides of (2.8) yields an expression for the velocity-field associated with the vorticity-field

$$\mathbf{u}(\mathbf{x}, t) = \begin{cases} -\frac{1}{2\pi}\int_A \frac{\mathbf{r}\times\boldsymbol{\omega}(\mathbf{x}', t)}{r^2}\mathrm{d}a' & \text{for } r \in \mathbb{R}^2 \\ -\frac{1}{4\pi}\int_V \frac{\mathbf{r}\times\boldsymbol{\omega}(\mathbf{x}', t)}{r^3}\mathrm{d}v' & \text{for } r \in \mathbb{R}^3 \end{cases} \tag{2.10}$$

This final relation between vorticity and velocity (i.e. the Biot-Savart law) allows for the determination of the velocity induced by various vortex elements, as shown in the following section.

2.2.3 Line Vortices

A line vortex represents a singularity of infinite vorticity concentrated along a single curve in space, such that the circulation associated with a closed-circuit pierced by it one time is finite. This circulation defines the strength of the line vortex.

2.2.3.1 Infinite Line Vortices

Consider a single infinite line vortex of concentrated strength Γ. Then the velocity induced at a field point $\mathbf{x}$ relative to some origin on the axis of the line vortex is given by the Biot-Savart integral [Kar80],

$$\mathbf{u}(\mathbf{x}) = \frac{-\Gamma}{4\pi}\int_{-\infty}^{\infty}\frac{(\mathbf{x}-\mathbf{s})\times \mathrm{d}\mathbf{s}}{|\mathbf{x}-\mathbf{s}|^3} \tag{2.11}$$

where $\mathrm{d}\mathbf{s}$ is an element of the filament at $\mathbf{s}$.

Denote $(\mathbf{x}-\mathbf{s})$ by $\mathbf{r}$ and the direction of $(\mathbf{r}\times \mathrm{d}\mathbf{s})$ by $\hat{\mathbf{e}}$. If θ is the angle measured from $\mathrm{d}\mathbf{s}$ to $\mathbf{r}$,

$$\mathbf{r}\times \mathrm{d}\mathbf{s} = -\left(r\sin\theta \mathrm{d}s\right)\hat{\mathbf{e}} \tag{2.12}$$

then the above expression for velocity becomes

$$\mathbf{u}(\mathbf{x}) = \left[\frac{\Gamma}{4\pi}\int_{-\infty}^{\infty}\frac{\sin\theta}{r^2}\mathrm{d}s\right]\hat{\mathbf{e}}. \tag{2.13}$$

We now let h denote the normal distance between $\mathbf{x}$ and the filament. We also denote the point of intersection of h with the filament as $\mathbf{s}_1$. Then,

$$r = h\ \mathrm{cosec}\theta \tag{2.14}$$

$$s_1 - s = h\ \cot\theta \tag{2.15}$$

$$\mathrm{d}s = h\ \mathrm{cosec}^2\theta \mathrm{d}\theta \tag{2.16}$$

and we can rewrite the integral of interest as,

$$\int_{-\infty}^{\infty}\frac{\sin\theta}{r^2}\mathrm{d}s = \frac{1}{h}\int_{0}^{\pi}\sin\theta \mathrm{d}\theta = \frac{2}{h}. \tag{2.17}$$

Hence, we have shown that

$$\mathbf{u}(\mathbf{x}) = \frac{\Gamma}{2\pi h}\hat{\mathbf{e}}, \tag{2.18}$$

thus concluding that the flow field of an infinite line vortex is equivalent to that of a two-dimensional point vortex as long as we consider planes orthogonal to the filament axis.

2.2.3.2 Finite Length Line Vortices

Consider a single line vortex segment with end-points a and b. We define a local orthogonal coordinate system by the triad $(\hat{\mathbf{s}}, \hat{\mathbf{m}}, \hat{\mathbf{n}})$, where $\hat{\mathbf{s}}$ is the unit tangent vector oriented in the direction of positive circulation, while $\hat{\mathbf{m}}$ and $\hat{\mathbf{n}}$ represent unit normal vectors along the curve. The concentrated vorticity distribution can be formally expressed in terms of the Dirac delta function and the curvilinear coordinate system defined above as

$$\boldsymbol{\omega}(s, m, n) = \Gamma\delta(m)\delta(n)\hat{\mathbf{s}}(s) \tag{2.19}$$

where (s, m, n) denote coordinate positions with respect to the curve. Invoking the Biot-Savart law (2.10) and accounting for the fact that $\mathrm{d}v' = \mathrm{d}s \cdot \mathrm{d}m \cdot \mathrm{d}n$, yields

$$\mathbf{u}(\mathbf{x}) = \frac{\Gamma}{4\pi}\int_a^b \frac{[\mathbf{x} - x(s)] \times \frac{\mathrm{d}\mathbf{x}}{\mathrm{d}\mathrm{s}}\mathrm{d}s}{|\mathbf{x} - \mathbf{x}(s)|^3}. \tag{2.20}$$

Equation (2.20) represents the velocity-field associated with a single finite segment of a line vortex with strength Γ.

2.3 Flow Kinetics and Vorticity Transport

It is often convenient to introduce the vorticity field of a flow $\boldsymbol{\omega}(\mathbf{x}, t)$ defined as

$$\boldsymbol{\omega} = \nabla \times \mathbf{u} = \text{curl } \mathbf{u}. \tag{2.21}$$

In homogeneous fluids, vorticity is only generated where there are shear-stresses (e.g. at solid boundaries). Vorticity can also be produced in the interior of inhomogeneous fluids or at free surfaces when gravity is acting. However, we restrict our attention to homogeneous incompressible flows for our discussions.

The vorticity transport equations can be derived by taking the curl of both sides of the momentum equations in Navier-Stokes. Here, we assume constant density ρ and constant kinematic viscosity ν subject to irrotational body forces (i.e. $\nabla \times \mathbf{f} = 0$):

$$\frac{\partial \boldsymbol{\omega}}{\partial t} = \nabla \times (\mathbf{u} \times \boldsymbol{\omega}) + \nu \nabla^2 \boldsymbol{\omega} \tag{2.22}$$

This can be rewritten as

$$\frac{D\boldsymbol{\omega}}{Dt} = \frac{\partial \boldsymbol{\omega}}{\partial t} + \mathbf{u} \cdot \nabla \boldsymbol{\omega} = \boldsymbol{\omega} \cdot \nabla \mathbf{u} + \nu \nabla^2 \boldsymbol{\omega} \tag{2.23}$$

after making use of the following vector identities

$$\begin{aligned} \mathbf{a} \times (\mathbf{b} \times \mathbf{c}) &= (\mathbf{a} \cdot \mathbf{c})\mathbf{b} - (\mathbf{a} \cdot \mathbf{b})\mathbf{c} & (2.24) \\ \mathbf{b} \cdot \nabla \mathbf{a} &= \frac{1}{2}[\nabla(\mathbf{b} \cdot \mathbf{a}) - \mathbf{b} \times (\nabla \times \mathbf{a}) - \mathbf{a} \times (\nabla \times \mathbf{b}) \\ &\quad - \nabla \times (\mathbf{b} \times \mathbf{a}) + \mathbf{b}(\nabla \cdot \mathbf{a}) - \mathbf{a}(\nabla \cdot \mathbf{b})] & (2.25) \end{aligned}$$

along with the fact that both $\mathbf{u}$ and $\boldsymbol{\omega}$ are divergence-free.

The left hand side of (2.23), the vorticity transport equation, represents the material derivative of vorticity in the flow. Another interpretation would be to decompose the material derivative into two components (i.e. $D\boldsymbol{\omega}/Dt = \partial\boldsymbol{\omega}/\partial t + \mathbf{u} \cdot \nabla\boldsymbol{\omega}$). Then, the first term (i.e. $\partial\boldsymbol{\omega}/\partial t$) represents the time rate of change of vorticity, while the second term (i.e. $\mathbf{u} \cdot \nabla\boldsymbol{\omega}$) represents the contribution to the rate of change due to fluid convection of vorticity. On the right hand side of (2.23) we have the vortex stretching term (i.e. $\boldsymbol{\omega} \cdot \nabla\mathbf{u}$), which represents the rate of change due to the deformation of line vortices. As the line vortex stretches, it results in more concentrated vorticity and increased velocity fluctuations in the flow. Of course, this term in not present in $\mathbb{R}^2$ since the vorticity in that case is always orthogonal to the velocity field. Finally, the viscous diffusion term (i.e. $\nu\nabla^2\boldsymbol{\omega}$) represents the rate of change due to the molecular diffusion of vorticity.

With the vorticity transport equations, the momentum-equation in Navier-Stokes can be replaced. Now, the unknowns to be solved for are $\mathbf{u}(\mathbf{x}, t)$ and $\boldsymbol{\omega}(\mathbf{x}, t)$, rather than $\mathbf{u}(\mathbf{x}, t)$ and $p(\mathbf{x}, t)$. Such a representation is useful because it conveniently separates the problem into two parts: (1) a kinetic part which handles the time changing vorticity field $\boldsymbol{\omega}(\mathbf{x}, t)$, and (2) a kinematic part which determines the velocity field $\mathbf{u}(\mathbf{x}, t)$ associated with the vorticity field $\boldsymbol{\omega}(\mathbf{x}, t)$ at a given time t. This separation will allow the problem to be reduced to an integral representation, which is the basis of the panel-particle method to be discussed in Chapter 4.

The representation above is also useful because it reduces the problem of determining the velocity field in an incompressible flow to one that depends only upon the regions with vorticity (i.e. the viscous regions of the problem). This is noteworthy because it makes such an approach especially appealing for problems involving confined regions of vorticity and large separation distances between bodies. Finally, upon noting the circulation theory of lift and the inherent relationship between circulation and vorticity, we can conclude that it is the vorticity of the flow that is responsible for generating the forces and moments exerted by the fluid on a solid body.

2.4 Kelvin-Helmholtz Theorems

The following theorems, attributed to Helmholtz and Kelvin, are necessary considerations in vortex modeling. The following summaries are taken from [Mar01].

Theorem: Helmholtz Vortex Laws

1. The strength of a vortex tube is uniform along the tube.
2. Vortex lines are material lines.
3. The strength of a vortex tube is invariant in time.

The first of these laws applies to all fluids, the second applies only to inviscid fluids, while the third applies only to inviscid fluids of uniform density.

Theorem: Kelvin's Circulation Theorem

- The circulation about a material closed-circuit is independent of time in a uniform-density, inviscid flow.

2.5 Vortex Sheets

There is sufficient vorticity present in the layer of fluid next to the surface of the body to change the fluid velocity in such a way as to satisfy the no-slip condition at the body's surface. The viscous nature of a fluid acts to diffuse this layer away from the surface, resulting in the well known boundary layer. A common perspective is to consider high Reynolds number flows as being made up of two flow regions. The first is the irrotational outer flow field, which is separated from the body surface by a second region of flow, namely a thin fluid layer comprised of highly rotational flow. Standard analytical approaches consider these regions separately, subject to appropriate matching conditions.

In the limit of infinite Reynolds number, the boundary layer thickness approaches zero (i.e. due to the reduction of viscous diffusion to zero). In this limit, the body surface will be covered with an infinitely thin vortex sheet of strength γ. For a body at rest, the fluid velocity will change discontinuously from zero beneath the sheet on the body surface to U_∞ parallel to the surface just outside of the sheet. We note here that surfaces of infinite vorticity are kinematically possible and do not violate any dynamical principles [Saf92]. Such surfaces are referred to as vortex sheets and are characterized by a discontinuous jump in velocity. Saffman provides a thorough treatment of the topic in [Saf92].

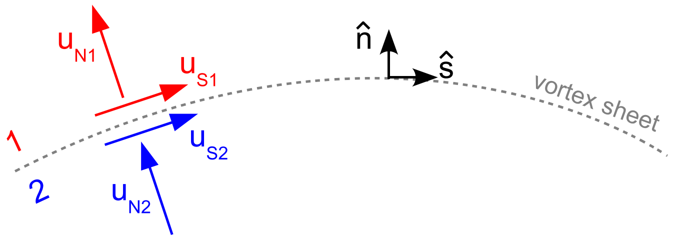

Figure 2.1: Vortex Sheet

We now consider free and bound vortex sheets more closely. For any vortex sheet, we require the mass flux across the sheet to be zero,

$$[\mathbf{u}] \cdot \hat{\mathbf{n}} = 0, \tag{2.26}$$

where $[\mathbf{u}] = \mathbf{u}_1 - \mathbf{u}_2$. That is, $[\mathbf{u}]$ must be oriented tangent to the sheet. We use the convention that the unit normal vector $\hat{\mathbf{n}}$ points from side 2 of S into side 1 of S (c.f. Figure 2.1). Then, the sheet strength $\boldsymbol{\gamma}$ and the velocity jump $[\mathbf{u}]$ are related by,

$$\gamma = \hat{\mathbf{n}} \times [\mathbf{u}], \;\; [\mathbf{u}] = \boldsymbol{\gamma} \times \hat{\mathbf{n}}. \tag{2.27}$$

Let $\mathbf{u}_\gamma(\mathbf{x}, t)$ denote the velocity of the vortex sheet. According to Wu et al. [WMZ06], imposing conservation of mass and momentum across the discontinuity surface, we arrive at the two basic features of a free vortex sheet:

1. $[p] = 0$
2. $\mathbf{u}_\gamma \cdot \hat{\mathbf{n}} = \frac{1}{2}(\mathbf{u}_1 + \mathbf{u}_2) = \overline{\mathbf{u}} \cdot \hat{\mathbf{n}}$

For the remainder of the discussion, we shall consider an incompressible flow that is irrotational everywhere away from the vortex sheet. Let P be a point on the sheet's surface S, and consider a curve C which connects P^+ and P^-. If the sheet has an edge, the curve can be drawn to go across S only once. Then the circulation along C is,

$$\Gamma = \oint_C \nabla\phi \cdot \mathrm{d}\mathbf{x} = \oint_C \mathrm{d}\phi = [\phi_P] \tag{2.28}$$

This construction is significant to our panel-particle method. Unlike the circulation along a generic loop, now Γ is a *point function* independent of the shape of C, so we can consider $\mathrm{D}\Gamma/\mathrm{D}t$. We can now write,

$$\boldsymbol{\gamma} = \hat{\mathbf{n}} \times \nabla_\pi[\phi] = \hat{\mathbf{n}} \times \nabla_\pi \Gamma \tag{2.29}$$

and

$$\nabla_\pi \Gamma = \boldsymbol{\gamma} \times \hat{\mathbf{n}}. \tag{2.30}$$

Noting that $\partial\Gamma/\partial n = [\mathbf{u}\cdot\hat{\mathbf{n}}] = 0$, we have $\nabla_\pi \Gamma = \nabla\Gamma$, so

$$\boldsymbol{\gamma} = \hat{\mathbf{n}} \times \nabla\Gamma \quad \text{and} \quad \nabla\Gamma = \boldsymbol{\gamma} \times \hat{\mathbf{n}}. \tag{2.31}$$

We now assume that the potential flow on both sides of the sheet comes from the same upstream flow (in order to keep a single reference point for the evaluation of velocity potential). Here this merely implies that the vortex sheet is not a free surface, thus enabling the sustenance of a pressure difference. Then, applying the unsteady Bernoulli equation,

$$\frac{\partial\phi}{\partial t} + \frac{p}{\rho} + \frac{1}{2}|\mathbf{u}|^2 = F(t), \tag{2.32}$$

on both sides of the sheet yields

$$\rho\left(\frac{\partial\Gamma}{\partial t} + \frac{1}{2}[|\mathbf{u}|^2]\right) = \begin{cases} -[p] & \text{for a bound vortex sheet} \\ 0 & \text{for a free vortex sheet} \end{cases} \tag{2.33}$$

where

$$\begin{aligned} \frac{1}{2}[|\mathbf{u}|^2] &= \frac{1}{2}(\mathbf{u}^+ + \mathbf{u}^-)\cdot(\mathbf{u}^+ - \mathbf{u}^-) \\ &= \overline{\mathbf{u}}\cdot[\mathbf{u}] \\ &= \overline{\mathbf{u}}\cdot\nabla\Gamma \\ &= -\hat{\mathbf{n}}\cdot(\boldsymbol{\gamma}\times\overline{\mathbf{u}}). \end{aligned} \tag{2.34}$$

Hence, we can write (2.33) as

$$\rho\left(\frac{\partial\Gamma}{\partial t} - \hat{\mathbf{n}}\cdot(\boldsymbol{\gamma}\times\overline{\mathbf{u}})\right) = \begin{cases} -[p] & \text{for a bound vortex sheet} \\ 0 & \text{for a free vortex sheet} \end{cases}. \tag{2.35}$$

This result contains some valuable information.

1. It confirms $\Gamma = [\phi]$ is Lagrangian invariant for a free vortex sheet, as put forth by Kelvin's circulation theorem.

2. If the flow is steady, then $\mathbf{u}\cdot\hat{\mathbf{n}} = 0$, so $\boldsymbol{\gamma}$ and $\overline{\mathbf{u}}$ must be aligned. In contrast, for an unsteady flow, we have

$$\boldsymbol{\gamma}\times\overline{\mathbf{u}} = \hat{\mathbf{n}}\frac{\partial\Gamma}{\partial t}. \tag{2.36}$$

3. Since the dynamics come from the Bernoulli equation, we have a close relationship between the pressure jump across a thin wing and the behavior of the bound and the free vortex sheet. This is the basis of lifting surface theory in classical aerodynamics and of the panel-particle method to be discussed in Chapter 4.

Considering the limiting processes described above and ignoring instabilities associated with boundary layers at high Reynolds numbers, it is easy to see that potential flows can be thought of as a special type of infinite Reynolds number flow. From this viewpoint, the surface vorticity model accurately represents physical reality at very large Reynolds number for attached flows. Numerical methods based on vortex sheet representations of body surfaces are thus among the "more natural" methods for such analyses.

2.6 Kutta Condition and Vorticity Shedding

Since the flow models discussed so far have been founded in potential theory, the role of viscosity has been assumed away in previous discussions through the assumption of large Reynolds numbers. However, we know that in any viscous fluid (i.e. all real fluids), the no-slip condition must be satisfied. This no-slip condition is responsible for the creation of vorticity in the boundary layer which is later shed into the wake and onward downstream. However, only one condition can be imposed at the body surface because we are dealing with the Euler equations of fluid flow, and that condition is the no-flow-penetration condition. As such, the no-slip condition is not accounted for in our model as of yet, meaning there is no mechanism for transferring the vorticity generated at the body into the wake.

Traditional approaches to reconciling the transfer of vorticity from the body to the fluid have considered conditions to be imposed at the salient edges of the body (e.g. at the trailing edge for attached flow). Such edge conditions, commonly referred to as "Kutta conditions", manifest themselves in a number of ways, all of which are consistent with one another. For example, some authors attempt to satisfy zero pressure-jump across the wake to guarantee that it remains a free vortex-sheet (i.e. it remains force-free). Others impose the condition of finite velocity flow “smoothly” leaving the body edges. In general, the Kutta condition requires that the vorticity created along an edge be convected with the flow. For an inviscid flow, this eliminates discontinuities in pressure and guarantees a finite fluid velocity that leaves each edge smoothly. Thus imposing the Kutta condition introduces a means of vorticity shedding in an otherwise inviscid flow model.

CHAPTER 3

Vortex Model Optimization

As discussed in Chapter 1, model reduction can lead to improvements in our understanding and analysis of fluid mechanical systems. Additionally, the availability of low-order flow representations is requisite to the design and implementation of closed-loop flow control technologies. In Section 1.2 we classified two distinct forms of model reduction, namely (1) mathematical and (2) physics-based techniques. Here we present a novel hybrid approach to model reduction for vortex dominated flows. A low-order representation of the flow can be attained by projecting empirical data onto a physically inspired vortex model. Attention of the current study will be devoted to formulating the optimization framework in the context of biologically inspired unsteady wing aerodynamics.

A brief survey of the literature is presented in Section 3.1. We then introduce Eldredge and Wang's impulse matching model in Section 3.2, which will serve as the baseline vortex model for the minimization procedure. The minimization problem is formulated in Section 3.3, which also details the method of solution and the viscous vortex particle method used in acquiring "truth" data for the optimization procedure. In Section 3.4 we apply the optimization procedure to two canonical wing maneuvers: (1) pitch-up and (2) impulsive translation at a fixed angle of attack. The models resulting from the optimization procedure demonstrate that a two point vortex representation *is* capable of accurately predicting the aerodynamic forces arising from agile wing maneuvers. Next, in Section 3.5, we discuss some of the remaining challenges in vortex model optimization. We close the chapter by offering some concluding remarks in Section 3.6.

3.1 Introduction

Biological mechanisms of flight have been the subject of much recent interest, namely for the technological advancement potential their understanding can serve to small-scale flight vehicle systems. The underlying wing motions associated with biological flight systems (e.g. flapping, pitch-up) exploit the leading edge vortex (LEV) for lift enhancement, as opposed to leading to the stall experienced by fixed-wing systems. Despite the current understanding of biological flight mechanics, low-order models for predicting the aerodynamic forces are still inadequate for designing control systems for agile flight vehicle maneuvers.

Low-order modeling of unsteady aerodynamics initially started with the work of Wagner in 1925 and Theodorsen in 1935. These early studies established a precedent for analyzing such problems by decomposing the forces and moments on the wing into contributions from circulatory (i.e. vortex induced) and non-circulatory (i.e. inertial reaction, or added mass) effects. Many researchers have taken similar phenomenological approaches to modeling. For example, many potential flows models have been developed to solve problems in this arena. These potential flow models account for the circulatory forces by modeling shed vorticity through simple vortex representations (e.g. vortex sheets [Wag25, The35, KS38, PW04, Kra91, Jon03, SE07, NK94, AS08], continuous sequences of point vortices [KW78, JP00, AZK06], or finite sets of point vortices with evolving strengths [BM54, Gra80, CL93, MS09]). Recently, two studies have made use of this sort of phenomenological approach. First, Ramesh and Gopalarathnam have made strides in modeling unsteady aerodynamics by means of continuous shedding of point vortices from the leading and trailing edges [RG12]. Their model is novel in that it makes use of a leading-edge suction parameter to determine the production of vorticity at the leading edge. Another recent study, by Pitt Ford and Babinsky, makes use of empirical data to determine the strength and position of a stationary LEV/TEV pair [FB12]. The approach can be seen as a parameter optimization based on experimental measurements.

Another approach to modeling can be classified under "dynamical systems approaches".

Goman and Khrabrov developed a state-space model that makes use of empirical relations between time constants and static separation points as a function of the the instantaneous angle of attack [GK94]. More recently, Brunton and Rowley developed a generalized Theodorsen model [BR11]. This state-space model is able to capture the effects of added mass as well as quasi-steady and unsteady wake effects. Most recently, Taha and Hajj devised a model based on extending the Duhamel Superposition Principle to nonlinear C_l versus α curves [TH13]. The main assumption was to represent the indicial response of the circulatory forces at all angles of attack, no matter how large, by means of the Wagner function. In doing so, they finally arrived at a convolution integral for the response of a wing undergoing arbitrary maneuvers. This response is then transformed to finite aspect ratio wings by means of strip theory. The performance of the Taha-Hajj model is quite remarkable for a flapping finite aspect ratio wing operating at a wide range of frequencies, though the author's have yet to report on their model's capabilities for other classes of kinematics.

Despite the promising results Taha and Hajj have demonstrated for their finite aspect ratio wing model, there is certainly still room for better modeling in terms of both prediction accuracy and applicability across a multitude of kinematics. For example, many classical potential flow models perform incredibly well for low angle of attack aerodynamics, but fail to provide reliable force predictions when the angle of attack is increased to the point that a LEV plays a significant role. Over the last few years, Eldredge and Wang have addressed this issue through the development of a low-order varying-strength vortex model [EW10, EW11, WE12]. Their model, which makes use of a Kutta condition at the wing's leading and trailing edges, provides reasonable force predictions in many cases; however, the model still remains inadequate for aerodynamic control and estimation. This is not entirely surprising, since the Kutta conditions are primarily used due to the lack of a better model. In reality viscous and curvature effects play a significant role, especially at the leading edge, thus making the Kutta condition an ill-suited model for maneuvers with LEV development.

In the present work, we relax the Kutta conditions imposed at the leading and trailing edges of Eldredge and Wang's impulse matching vortex model [EW11, WE12] and formulate a constrained minimization problem, with respect to high fidelity simulation data, to aid in the improvement and understanding of edge conditions associated with unsteadily maneuvering wings. We find that, as expected, the Kutta condition is not the best choice for modeling such flows. Our model optimizations reveal that the fore-wing stagnation point is actually located slightly aft of the leading edge, with its position varying throughout the maneuver. Ultimately, the framework developed here generalizes to other classes of vortex systems where model improvement is desired. Having such a tool available will lead to improved vortex models for a wide variety of vortex dominated flows, thus making vortex-based aero- and hydrodynamic estimation more tractable and alluring in future flow control and flight control applications.

3.2 Vortex Model Formulation

In the present section, we briefly describe the impulse matching vortex model for predicting the aerodynamic forces of a pitching and/or translating airfoil. The following discussion summarizes the formulation presented in [EW11] and [WE12]. The reader is referred to these sources for a more detailed development of the model.

3.2.1 Complex Potential: System of Vortices in the Presence of a Flat Plate

In seeking the forces and moments associated with the arbitrary motion of an infinitely thin flat plate in the presence of point vortices, we focus on the impulse matching model developed by Eldredge and Wang in [EW11] and [WE12]. The formulation makes use of complex potentials, such that the plate can be mapped from the circle plane (i.e. $\zeta = \xi + i\eta$) via the Joukowski mapping, as depicted in Figure 3.1.

The complex mapping for a plate of semi-chord a can be expressed as

$$z(\zeta) = z_c + \tilde{z}(\zeta)e^{i\alpha} \tag{3.1}$$

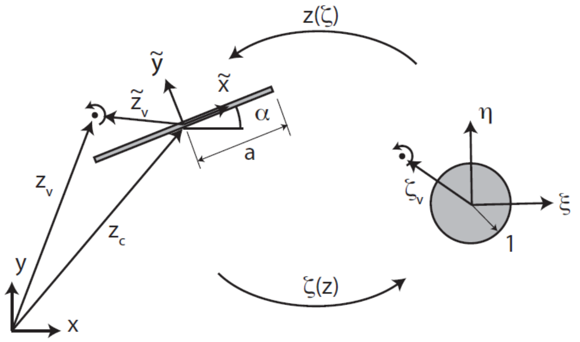

Figure 3.1: Schematic of plate mapping to circle of unit radius in the ζ-plane.

where

$$\tilde{z}(\zeta) = \frac{a}{2}\left(\zeta + \frac{1}{\zeta}\right). \tag{3.2}$$

The plate is mapped into a circle of unit radius in the ζ-plane, that is $\zeta = e^{i\theta}$ describes its surface for $\theta = [0, 2\pi)$. The leading edge is denoted by z_{10}, which is located at $\zeta = 1$ (i.e. $\tilde{z}_{10} = a$). Similarly, the trailing edge is denoted by z_{20} which corresponds to $\zeta = -1$ (i.e. $\tilde{z}_{20} = -a$). The Jacobian of this mapping is

$$z'(\zeta) = \frac{a}{2}e^{i\alpha}\left(1 - \frac{1}{\zeta^2}\right) \tag{3.3}$$

where $(\cdot)'$ denotes differentiation with respect to the argument.

For a plate in arbitrary rigid body motion in the presence of N-vortices, the complex potential in the circle plane is [Mil96]

$$\tilde{F}(\zeta) = -\frac{ia\tilde{V}}{\zeta} - \frac{i\Omega a^2}{4\zeta^2} + \sum_{v=1}^{N} \frac{\Gamma_v}{2\pi i}\left[\log\left(\zeta - \zeta_v\right) - \log\left(\zeta - \zeta_v^{(i)}\right)\right] \tag{3.4}$$

where $\zeta_v^{(i)} = 1/\zeta_v^*$ is the position of the image vortex (and $(\cdot)^*$ denotes complex conjugation), and the leading dipole and quadrupole terms constitute rigid body modes. Here, $\dot{z}_c e^{-i\alpha} = \tilde{U} + i\tilde{V}$ is the complex velocity of the plate in its body-fixed coordinate system, and $\Omega = \dot{\alpha}$ is the angular velocity.

A point vortex of constant strength at position z_v will move with the Kirchhoff velocity (the local fluid velocity minus the vortex's self-contribution), denoted by W_{-v}

$$\frac{\mathrm{d}z_v}{\mathrm{d}t} = W^*_{-v}(z_v) = \left[z'^*(\zeta_v)\right]^{-1} \lim_{\zeta\to\zeta_v} \left[\frac{\partial \tilde{F}}{\partial \zeta} - \frac{\Gamma_v}{2\pi i}\frac{1}{\zeta - \zeta_v} - \frac{\Gamma_v}{4\pi i}\frac{z''(\zeta)}{z'(\zeta)}\right]. \tag{3.5}$$

The final term inside the brackets is the so-called Routh correction [Cle73], which accounts for the curvature of the mapping.

3.2.2 Force on the Plate

The force on the plate can be obtained from the linear impulse

$$F_x + iF_y = -\rho \frac{\mathrm{d}P}{\mathrm{d}t}, \tag{3.6}$$

where the impulse can be obtained from the general vector formula [EW11, WE12]

$$\mathbf{P} = \int_{A_f} \mathbf{x} \times \boldsymbol{\omega} \mathrm{d}A + \oint_{S_b} \mathbf{x} \times \boldsymbol{\gamma}_\omega \mathrm{d}s + \oint_{S_b} \mathbf{x} \times (\boldsymbol{\gamma}_b + \mathbf{n} \times \mathbf{u}_b)\,\mathrm{d}s \tag{3.7}$$

where $\boldsymbol{\omega}$ is the ambient vorticity in the fluid region (denoted by A_f), $\mathbf{u_b}$ is the local surface velocity of the body with outward normal $\mathbf{n}$ on surface S_b, and $\boldsymbol{\gamma}_\omega$ and $\boldsymbol{\gamma}_b$ are the strengths of the vortex sheets that exist on the body surface in response to ambient vorticity and body motion, respectively.

Equation (3.7) can be transformed into complex notation and simplified to the final form [EW11, WE12]

$$\rho P = ie^{i\alpha}\left[\tilde{M}_{yy}\tilde{V} - \sum_{v=1}^{N} \frac{1}{2}\rho a \Gamma_v \left(\zeta_v - \zeta_v^{(i)}\right)\right] \tag{3.8}$$

where $\tilde{M}_{yy} = \rho\pi a^2$ is the sole added-mass coefficient in the body-fixed frame. The first term corresponds to the inertial reaction force in response to linear accelerations and coupled rotations-translations of the plate. The second term represents the contribution from the vortex and its image (or alternatively, from the vortex, modified by the presence of the plate).

3.2.3 Impulse Matching Model

Wang and Eldredge formulated the equations of motion for a vortex system in the presence of a body by means of an impulse matching model, based on the principle that any time variation of the strength of a point vortex should have no direct effect on the force [WE12]. Since the force arises from the rate of change of impulse, this effect can be achieved by considering a virtual "surrogate" vortex at the same instantaneous location and strength as the physical vortex, but moving with constant strength at the Kirchhoff velocity (3.5). The resulting equations of motion for the vortex system considered are

$$\frac{\mathrm{d}z_v}{\mathrm{d}t} + \frac{h(z_v - z_{10}, z_v - z_{20})}{\Gamma_v}\frac{\mathrm{d}\Gamma_v}{\mathrm{d}t} = W^*_{-v}(z_v) \tag{3.9}$$

where

$$h(v,w) = \frac{|v|w + |w|v}{|v| + |w|}. \tag{3.10}$$

We note that this can also be written in a more compact form as

$$\frac{\mathrm{d}\mathbf{x}}{\mathrm{d}t} = \mathbf{f}(\mathbf{x},\mathbf{u},t) \tag{3.11}$$

where $\mathbf{x}$ consists of the real and complex components of the vortex positions as well as the vortex strengths, while $\mathbf{u}$ represents a vector of the time rate of change of the vortex strengths.

For a flat plate with a leading and trailing edge, two developing vortices are considered in addition to any vorticity already existing in the flow. The strengths of these developing point vortices are determined by applying a Kutta condition at each edge. This can be expressed through the set of regularity conditions

$$2\tilde{V}\zeta_{k0} + \Omega a + \sum_{v=1}^{N}\frac{\Gamma_v}{\pi a}\mathrm{Re}\left\{\frac{\zeta_v + \zeta_{k0}}{\zeta_v - \zeta_{k0}}\right\} = 0, \qquad k = 1,2 \tag{3.12}$$

where $\zeta_{10} = 1$ and $\zeta_{20} = -1$. The system of equations in (3.12) is solved for Γ_1 and Γ_2 at each instant, based on the instantaneous states of the plate and the constant-strength vortices.

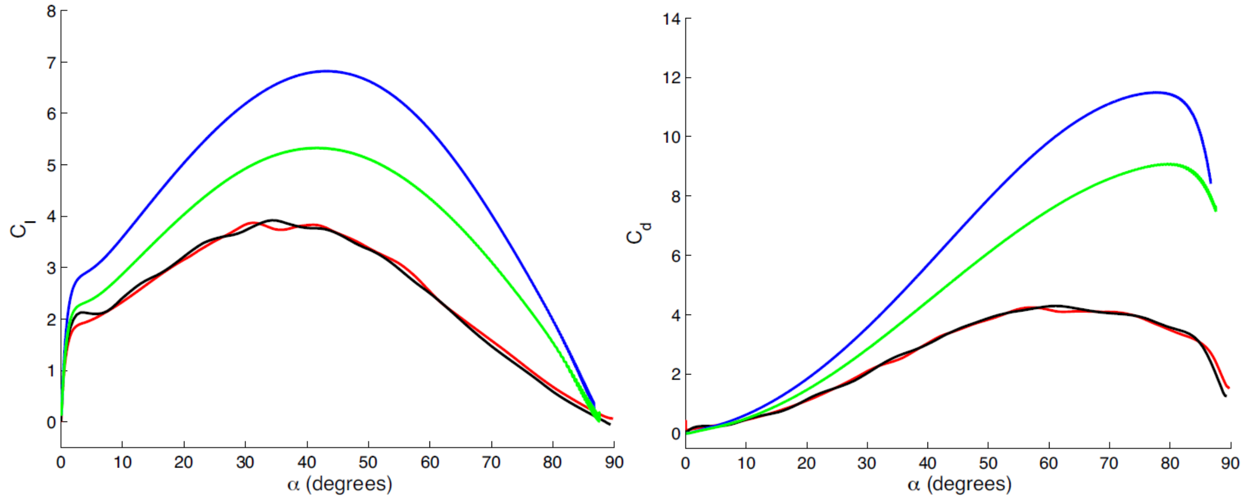

Figure 3.2: Comparison of the force histories for a pitch-up maneuver ($K = 0.2$). The results are taken from the experiments of Granlund et al. (—), the viscous vortex particle method (—), the Brown-Michael vortex model (—), and the impulse matching model (—). Figure courtesy of [EW11].

The capabilities of the impulse matching model are showcased in [EW11] and [WE12]. Significant improvements are made over the Brown-Michael vortex model, developed in [EW10], for the same canonical maneuvers. Figure 3.2, taken from [EW11], provides a comparison of both low-order models with respect to high fidelity numerical results as well as experimental results. It is clear that there is still significant room for making model improvements. In the next section, we develop an approach grounded in optimal control theory and the calculus of variations to guide these efforts.

3.3 A Variational Approach to Vortex Model Improvement

The impulse matching model leads to reasonable aerodynamic force predictions under many circumstances, but these predictions are still inadequate for the purposes of aerodynamic control. In the present section, we formulate a constrained minimization problem with free initial states by which the shortcomings of the imposed Kutta conditions are determined. We outline the steepest descent algorithm used in solving the optimization problem, and we discuss the high-fidelity computations used in determining the true force histories against which the optimization is conducted.

3.3.1 Constrained Optimization Formulation

We seek to improve Eldredge and Wang's impulse matching model by relaxing the Kutta condition at both edges. Instead, we determine the time rate of change of vortex strengths such that the model force predictions more accurately represent the true aerodynamic forces observed. To do so, we consider the nonlinear continuous time optimal control problem with fixed initial and terminal times. We seek the optimal control history $\mathbf{u}^*(t)$ and the parameter vector $\boldsymbol{\theta}^*$ that minimize the mean squared error between the true and the model predicted force histories, while adhering to the governing equations of the vortex model. That is,

$$J^* = \min_{\mathbf{u},\boldsymbol{\theta}} \int_{t_o}^{t_f} g(\mathbf{x},\mathbf{u},t)\mathrm{d}t \tag{3.13}$$

$$= \min_{\mathbf{u},\boldsymbol{\theta}} \int_{t_o}^{t_f} \left\{ \left[F_x^{\text{true}}(t) - F_x^{\text{model}}(\mathbf{x},\mathbf{u},t)\right]^2 - \left[F_y^{\text{true}}(t) - F_y^{\text{model}}(\mathbf{x},\mathbf{u},t)\right]^2 \right\} \mathrm{d}t \tag{3.14}$$

subject to the the vortex evolution equations imposed by the impulse matching model

$$\dot{\mathbf{x}}(t) = \mathbf{f}(\mathbf{x},\mathbf{u},t) \tag{3.15}$$

and the initial and final states

$$\mathbf{x}(t_o) = \mathbf{x}_o(\boldsymbol{\theta}) \tag{3.16}$$

$$\mathbf{x}(t_f) = \mathbf{x}_f(\boldsymbol{\theta}) \tag{3.17}$$

which depend upon the parameter vector $\boldsymbol{\theta}$. In the present development, we simply set $\mathbf{x}_o(\boldsymbol{\theta}) = \mathbf{x}_o$ and $\mathbf{x}_f(\boldsymbol{\theta}) = \mathbf{x}_f$. Moreover, the state and input vectors are defined, respectively, as

$$\mathbf{x}(t) := \begin{bmatrix} \xi_1 & \eta_1 & \xi_2 & \eta_2 & \Gamma_1 & \Gamma_2 \end{bmatrix}^{\mathsf{T}} \in \mathbb{R}^6 \tag{3.18}$$

and

$$\mathbf{u}(t) := \begin{bmatrix} \dot{\Gamma}_1 & \dot{\Gamma}_2 \end{bmatrix}^{\mathsf{T}} \in \mathbb{R}^2 \tag{3.19}$$

where $\zeta_v = \xi_v + i\eta_v$ corresponds to the position coordinates of vortex v in the circle plane. The right hand side of the state update equation follows the impulse matching model for the vortex positions, while the strength propagation of each vortex v is determined from the control input $\dot{\Gamma}_v$.

To solve the above minimization, we construct the Hamiltonian for this system

$$\mathcal{H} = g(\mathbf{x}, \mathbf{u}, t) + \mathbf{p}(\mathbf{x}, \mathbf{u}, t)^{\mathsf{T}} \mathbf{f}(\mathbf{x}, \mathbf{u}, t) \tag{3.20}$$

where $\mathbf{p}(\mathbf{x}, \mathbf{u}, t)$ represents the costate of the system, corresponding to the marginal cost of violating the system constraints. We then seek the optimal input history $\mathbf{u}^*(t)$ and the optimal parameter vector $\boldsymbol{\theta}^*$ such that the first order necessary conditions for optimality are satisfied. That is,

$$\begin{aligned}
\dot{\mathbf{x}} &= \frac{\partial \mathcal{H}}{\partial \mathbf{p}}(\mathbf{x}, \mathbf{u}, t) = \mathbf{f}(\mathbf{x}, \mathbf{u}, t) && (3.21)\\
\dot{\mathbf{p}} &= -\frac{\partial \mathcal{H}}{\partial \mathbf{x}}(\mathbf{x}, \mathbf{u}, t) = -\frac{\partial g}{\partial \mathbf{x}}(\mathbf{x}, \mathbf{u}, t) - \left[\frac{\partial \mathbf{f}}{\partial \mathbf{x}}(\mathbf{x}, \mathbf{u}, t)\right]^{\mathsf{T}} \mathbf{p}(\mathbf{x}, \mathbf{u}, t) && (3.22)\\
0 &= \frac{\partial \mathcal{H}}{\partial \mathbf{u}}(\mathbf{x}, \mathbf{u}, t) = \frac{\partial g}{\partial \mathbf{u}}(\mathbf{x}, \mathbf{u}, t) + \left[\frac{\partial \mathbf{f}}{\partial \mathbf{u}}(\mathbf{x}, \mathbf{u}, t)\right]^{\mathsf{T}} \mathbf{p}(\mathbf{x}, \mathbf{u}, t) && (3.23)\\
0 &= \frac{\partial J}{\partial \boldsymbol{\theta}}. && (3.24)
\end{aligned}$$

Minimizations with respect to both $\mathbf{u}$ and $\boldsymbol{\theta}$ are conducted by means of the steepest descent algorithm, outlined in Section 3.3.2.

3.3.2 Method of Solution

The steepest descent algorithm, tailored to our problem of interest, consists of five steps [BH75, Kir04, SJ10]

1. Uniformly discretize the time interval $[t_0, t_f]$ into N equal subintervals and assume the control takes the form of a zero-order hold $\mathbf{u}^{(0)}(t) = \mathbf{u}^{(0)}(t_k),\ \ t \in [t_k, t_{k+1}],\ k = 0, 1, \ldots, N-1$.

2. Apply the assumed control sequence $\mathbf{u}^{(i)}$ to integrate the state equations forward in time from t_0 to t_f with the current iteration of the initial conditions $\mathbf{x}(0) = \mathbf{x}_o(\boldsymbol{\theta})$ and store the state trajectory $\mathbf{x}^{(i)}$.

3. Apply both $\mathbf{u}^{(i)}$ and $\mathbf{x}^{(i)}$ to integrate the costate equations backward in time from t_f to t_0, where the terminal value of the costate $\mathbf{p}$ is $\mathbf{p}^{(i)}(t_f) = 0$.

4. Evaluate (by finite differences) and store both $\partial J^{(i)}/\partial\boldsymbol{\theta}$ and $\partial\mathcal{H}^{(i)}(t)/\partial\mathbf{u}$, $t \in [t_0, t_f]$.

5. Evaluate the stopping criterion and stop the iterative procedure if

$$\left\|\frac{\partial\mathcal{H}^{(i)}}{\partial\mathbf{u}}\right\| = \left\{\int_{t_0}^{t_f} \left[\partial\mathcal{H}^{(i)}(t)/\partial\mathbf{u}\right]^{\mathsf{T}} \left[\partial\mathcal{H}^{(i)}(t)/\partial\mathbf{u}\right] \mathrm{d}t\right\}^{1/2} \leq \epsilon,$$

   where ϵ is a threshold value for the stopping criterion. Otherwise adjust the control sequence and parameter vector to

$$\mathbf{u}^{(i+1)}(t_k) = \mathbf{u}^{(i)}(t_k) - \kappa_u \frac{\partial\mathcal{H}^{(i)}}{\partial\mathbf{u}}(t_k), \quad k = 0, 1, \ldots, N-1.$$

   and

$$\boldsymbol{\theta}^{(i+1)} = \boldsymbol{\theta}^{(i)} - \kappa_\theta \frac{\partial J^{(i)}}{\partial\boldsymbol{\theta}}$$

   where κ_u and κ_θ are step sizes for the iterations in $\mathbf{u}$ and $\boldsymbol{\theta}$, respectively. Then set $\boldsymbol{\theta}^{(i)} \leftarrow \boldsymbol{\theta}^{(i+1)}$ and $\mathbf{u}^{(i)} \leftarrow \mathbf{u}^{(i+1)}$, and repeat steps 2–5.

3.3.3 True Force Histories: High-Fidelity Viscous Vortex Particle Simulation

In the above formulation, we have assumed the existence of true force history data (i.e. F_x^{true} and F_y^{true}) with respect to which we minimize the error of our model predictions. For the purposes of the present study, we incorporate data from high-fidelity computations performed by way of the viscous vortex particle method (VVPM). VVPM relies upon a discretization of the Navier-Stokes equations by vorticity-bearing particles that advect with the local fluid velocity. The method uses a fractional stepping procedure, in which the fluid convection, fluid diffusion, and vorticity creation are treated in separate substeps of each time increment. The results of the VVPM computations have been verified against the experimental data of

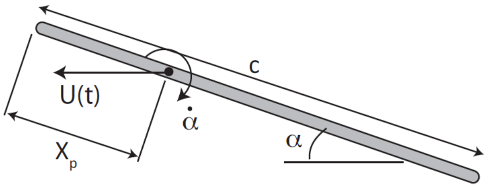

Figure 3.3: Schematic of pitching wing.

Granlund et al. 2010 for the case of a pitching plate [GOG10, EW10, EW11, WE12]. Details of the VVPM algorithm can be found in [Eld07].

3.4 Results and Discussion

The present section reports the results of the optimized impulse matching model for the cases of a pitching plate and an impulsively translating plate at a fixed angle of attack. We compare the results of the optimized model with high-fidelity VVPM simulation data and with the original impulse matching model (i.e. with the Kutta condition imposed at both the leading and trailing edges). We consider the pitch-up maneuver in Section 3.4.1 for pitching maneuvers of varying rates. The impulsively translating plate is studied in Section 3.4.2 for three different fixed angles of attack.

3.4.1 Pitching Kinematics

The pitching wing to be studied in this work is drawn schematically in Figure 3.3. A two-dimensional wing profile of chord $c = 2a$, thickness $0.023c$, and semicircular edges translates rectilinearly at speed $U(t)$ in an incompressible flow with density ρ and kinematic viscosity ν. The wing undergoes a pitch-up maneuver at nominal angular velocity $\dot{\alpha}_0$ from 0^{o} to 90^{o} about an axis situated X_p aft of the leading edge. We consider the case of pitching, in which the translational motion is defined as a constant speed, $U(t) = U_0$.

The angle of attack, α, is prescribed over time with a schedule given by

$$\alpha(t) = \alpha_0 \frac{G(t)}{\max G} \tag{3.25}$$

where the maximum of G is taken over the time interval of interest, so that the maximum angle α_0 is achieved when G reaches this maximum. The function G describes a smoothed pitch-up maneuver starting at zero angle of attack,

$$G(t) = \log \left[\frac{\cosh(a_s U_0 (t - t_1)/c)}{\cosh(a_s U_0 (t - t_2)/c)} \right] - a_s U_0 (t_1 - t_2)/c. \tag{3.26}$$

The parameter a_s controls the speed of the transitions between kinematic intervals, with larger values producing sharper transitions. The times t_1 and t_2 represent transition instants during the maneuver: t_1 is the start of the pitch-up, while $t_2 = t_1 + \alpha_0/\dot{\alpha}_0$ is the end of the pitch-up. In the high-fidelity simulations, the pitch-up starts at $t_1 = c/U_0$, which allows sufficient time for the boundary layers to develop on the plate prior to the initiation of rotation. We note that, for the function G to work as designed, the aforementioned maximum of G should be taken over a time interval $[t_1, t_b]$, where $t_b \geq t_2$. Clearly, this maximum is simply $G(t_b)$ for the function specified here, and if, $t_b \gtrsim t_2 + 2c/(a_s U_0)$, then $\max G \approx 2 a_s U_0 (t_2 - t_1)/c$.

The Reynolds number, $Re = U_0 c/v$, is fixed at 1000 for all high-fidelity simulations. This choice is a compromise between ensuring sufficiently small effects from viscosity and requiring modest computational resources for full resolution of flow phenomena. The nominal pitch rate, $\dot{\alpha}$, is specified via the dimensionless parameter $K = \dot{\alpha}_0 c/(2U_0)$. The pitch axis is located at the leading edge of the plate ($X_p = 0$), and the maximum angle α_0 is $\pi/2$. The smoothing parameter, a_s, in the kinematics described in (3.26) is set to 11 in all cases. The resulting lift and drag are scaled conventionally by $\rho U_0^2 c/2$ to form coefficients C_l and C_d, respectively.

The high-fidelity simulations are conducted throughout this study with particle spacing $\Delta x = 0.0025c$, time-step size $\Delta t = 0.0025c/U_0$, and 1588 panels on the plate. The results were verified to be sufficiently converged with this choice of parameters. Moreover, comparison to experimental results provides assurance of the method's reliability (c.f. Figure 3.2).

We only consider minimizing the mean squared error of the force predictions after the plate has translated forward by 10% of a chord length. It is also useful to note that for the purpose of the impulse matching model presented in Section 3.2, the $\tilde{y}$-velocity component in the plate-fixed coordinate system is given by $\tilde{V} = \Omega(X_p - c/2) - U \sin \alpha$, where $\Omega = \dot{\alpha}$.

3.4.1.1 Pitching Kinematics: K=0.2

The lift and drag coefficients corresponding to the pitch-up maneuver of a flat plate are presented in Figure 3.4. The results of the optimized impulse matching model are presented alongside those of the high-fidelity simulation ($Re = 1000$) and the impulse matching model with Kutta condition imposed at both edges. We see that the optimized model performs significantly better than the original low-order model in predicting the force histories. The accuracy of the optimized model's force prediction is quite remarkable, given the fact that the low-order model possesses only six degrees of freedom, whereas the numerical simulation ultimately uses on the order of 5×10^5 computational particles, each with three degrees of freedom.

Figures 3.5–3.7 present the inputs and states of the system corresponding to the optimized model compared alongside the values resulting from the original model with Kutta conditions imposed. Figure 3.5 presents the control input for both of these models, showing visible differences in the trends of $\dot{\Gamma}_{\text{LEV}}$ and $\dot{\Gamma}_{\text{TEV}}$. The most significant difference between the models arises in the strength predictions, presented in Figure 3.6. We see that the Kutta condition tends to over-predict the magnitude of the strength of both vortices. This is expected, since in reality there are viscous effects at play which lead to a reduction in the net circulation in the vicinity of either edge. This is especially obvious at the leading edge where the LEV undergoes significant interaction with secondary vortices of opposite sign. Figure 3.7 presents the vortex trajectories in the physical plane. The difference in trajectories

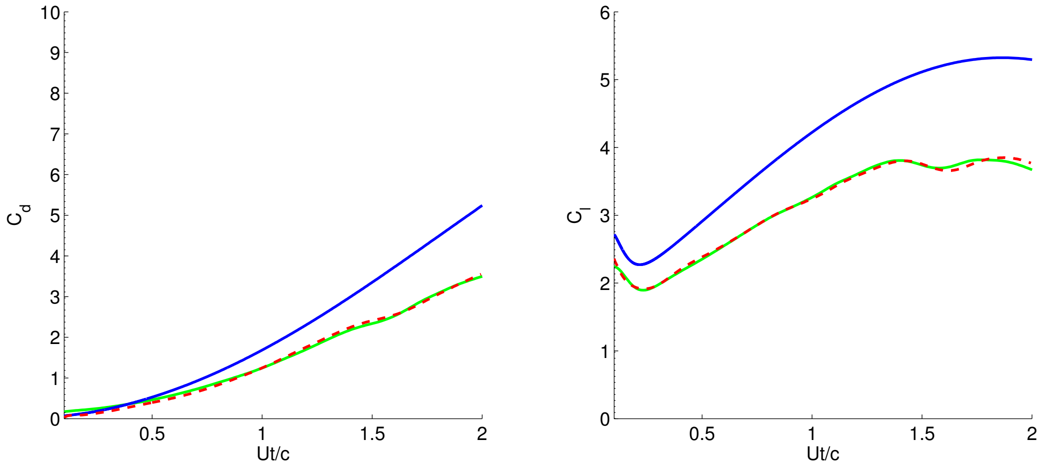

Figure 3.4: Pitching plate ($K = 0.2$) drag and lift coefficient histories associated with the VVPM data —, the impulse matching model with Kutta conditions imposed at both the leading and trailing edge —, and the optimized impulse matching model - -.

arises as a result of the difference in the evolution of the vortex strengths.

Figure 3.8 compares the streamlines of the optimized model with those of the original model at $\alpha = 15^o$, 30^o, and 45^o during the pitching motion. The vorticity contours from the high-fidelity VVPM simulations are also included for comparison. Inspection of the stagnation streamlines in the optimized model highlights the fact that the fore-wing stagnation point is slightly aft of the leading edge in the optimized model, not at the leading edge as constrained by a Kutta condition. The breakdown of the Kutta condition is expected for this maneuver since the flow structures in the vicinity of the leading edge do not resemble the release of a “smooth” thin sheet of vorticity from that edge, as seen in the vorticity contour plot from VVPM.

3.4.1.2 Pitching Kinematics: K=0.7

We now consider a more rapid pitch-up maneuver at $K = 0.7$, for which the lift and drag coefficient time histories are presented in Figure 3.9. Again, we see outstanding improvement

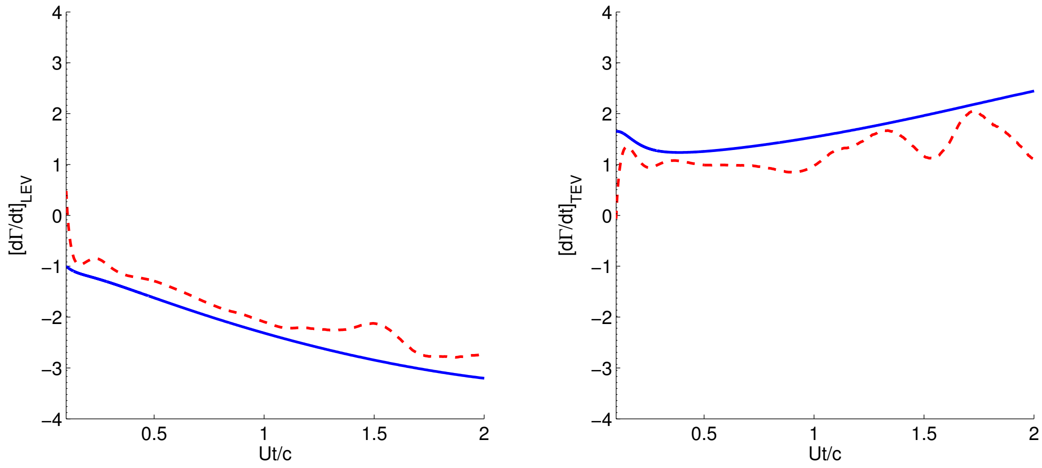

Figure 3.5: Pitching plate ($K = 0.2$) time rate of change of leading and trailing edge vortex strengths from the impulse matching model with Kutta conditions imposed at both the leading and trailing edge — and from the optimized impulse matching model - -.

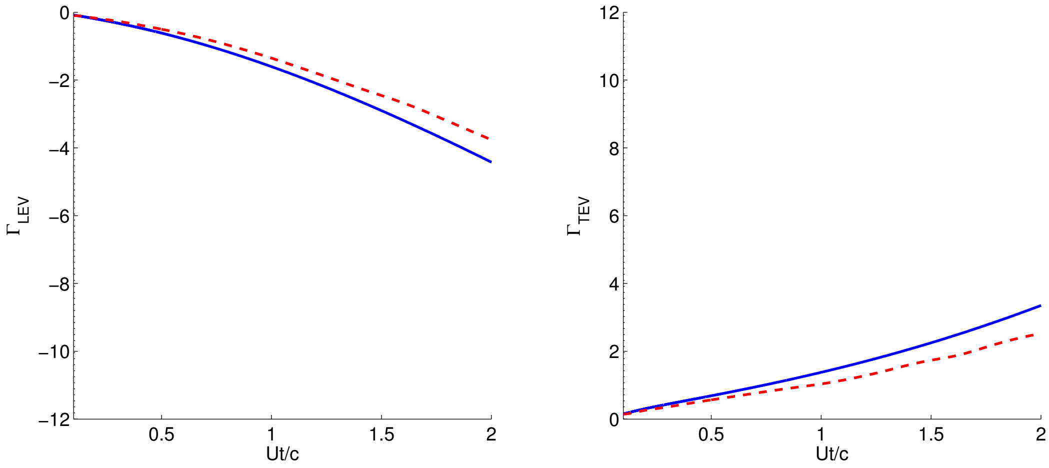

Figure 3.6: Pitching plate ($K = 0.2$) leading and trailing edge vortex strengths from the impulse matching model with Kutta conditions imposed at both the leading and trailing edge — and from the optimized impulse matching model - -.

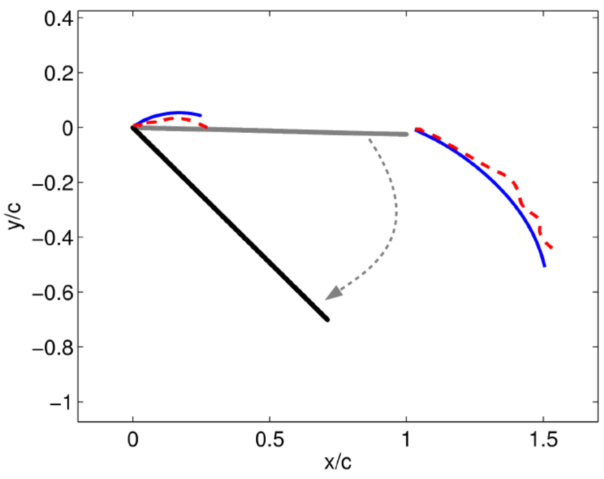

Figure 3.7: Pitching plate ($K = 0.2$) leading and trailing edge vortex trajectories from the impulse matching model with Kutta conditions imposed at both the leading and trailing edge — and from the optimized impulse matching model - -.

compared to the original Kutta-based impulse matching model.

Figure 3.10 presents the control inputs for the optimized model and the Kutta imposed model. Again, the results here demonstrate notable differences $\dot{\Gamma}_{\mathrm{LEV}}$ and $\dot{\Gamma}_{\mathrm{TEV}}$ between the two models. We point out that the final value of the optimal control input aligns with the Kutta-based value as a matter of coincidence (i.e. this condition was not in any way imposed through the optimization procedure).

Figure 3.11 shows the strength histories corresponding to each model. The Kutta condition over-predicts the magnitudes of these values in this case as well. The discrepancy seems to be to a lesser degree for $K = 0.7$ than for $K = 0.2$ because the rapid pitch-up allows less time for viscous effects to play as dominant a role. This fact also accounts for the better accuracy of the force predictions for $K = 0.7$ (Figure 3.9) than for $K = 0.2$ (Figure 3.4). The resulting vortex trajectories corresponding to both models is presented in Figure 3.12. Comparisons of the model streamlines and VVPM vorticity contours are presented in 3.13. We report similar findings as with the $K = 0.2$ pitch-up, namely that the fore-wing stagnation point is actually slightly aft of the leading edge in the optimized model. Additionally,

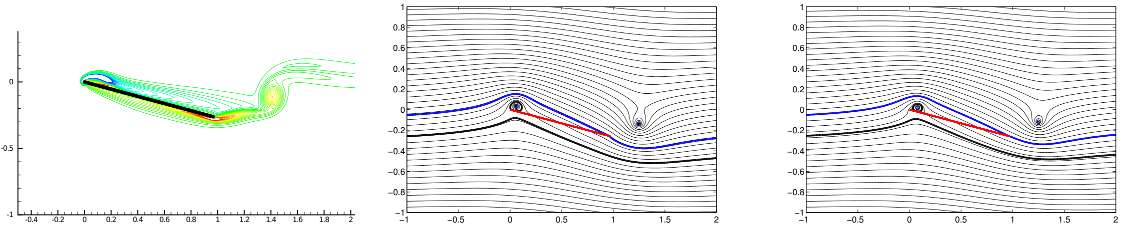

(a) VVPM ($\alpha = 15^o$) (b) IMM ($\alpha = 15^o$) (c) Optimized IMM ($\alpha = 15^o$)

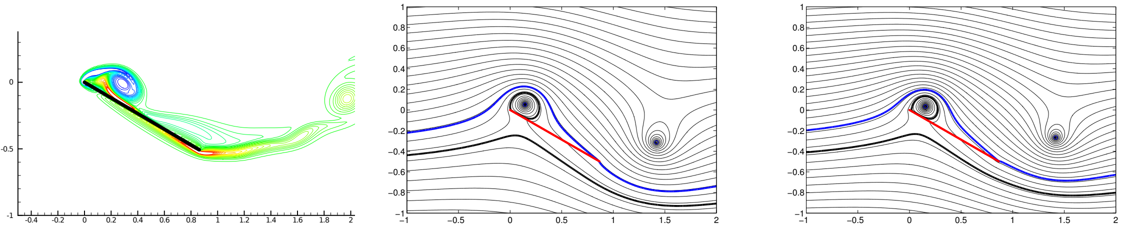

(d) VVPM ($\alpha = 30^o$) (e) IMM ($\alpha = 30^o$) (f) Optimized IMM ($\alpha = 30^o$)

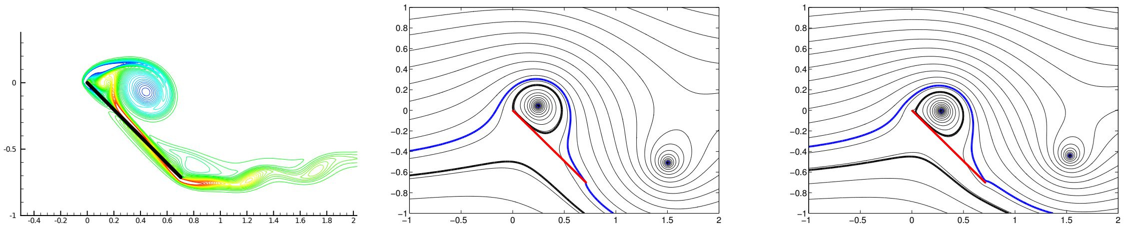

(g) VVPM ($\alpha = 45^o$) (h) IMM ($\alpha = 45^o$) (i) Optimized IMM ($\alpha = 45^o$)

Figure 3.8: Pitching plate ($K = 0.2$) snapshots at $\alpha = 15^o$, 30^o, and 45^o. The first column reports vorticity contours from the viscous vortex particle method (VVPM), while the second and third columns present streamlines from the original impulse matching model with a Kutta condition imposed (IMM) and the optimized impulse matching model (Optimized IMM), respectively. Stagnation streamlines are drawn in bold.

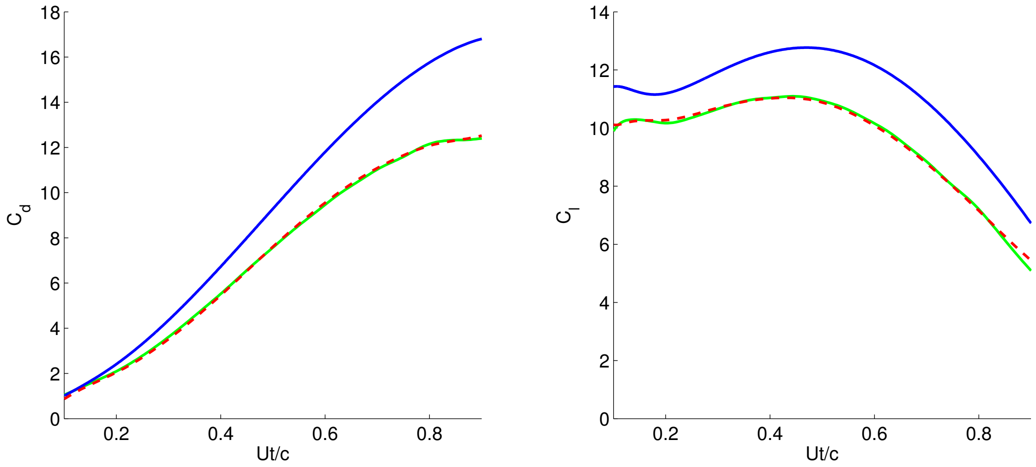

Figure 3.9: Pitching plate ($K = 0.7$) drag and lift coefficient histories associated with the VVPM data —, the impulse matching model with Kutta conditions imposed at both the leading and trailing edge —, and the optimized impulse matching model - -.

this stagnation points tends to move about the fore-wing section throughout the maneuver, never locking in to a single position. We emphasize here, in view of this comment, that these optimization results were not taken to steady-state.

3.4.2 Impulsive Translation

In the previous section, we considered the performance of the optimized model for the pitching problem, for which the aerodynamic forces consist of both inertial and circulatory contributions, and the leading-edge vortex develops in response to both translation and rotation relative to the surrounding fluid. In the present section, we explore the optimized model's performance in the simpler scenario of impulsive translation at a fixed angle of attack at $Re = 1000$. This motion results in an infinitely large inertial reaction force at $t = 0^+$, but at all subsequent times the force is due almost entirely to circulatory effects (with the exception of drag at small angles, which is dominated by skin friction). For the purposes of the optimization, we consider minimizing the mean squared error between force histories after the plate has translated 10% of a chord forward. We evaluate the optimized model for this

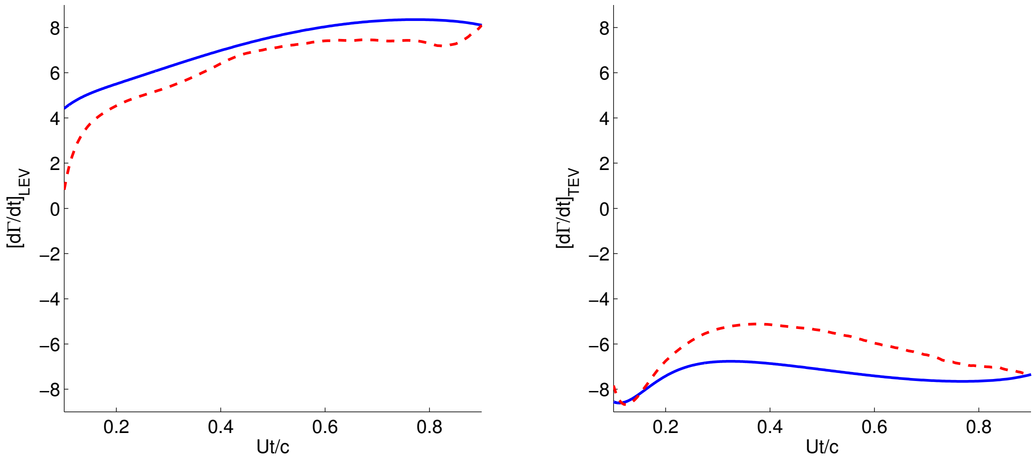

Figure 3.10: Pitching plate ($K = 0.7$) time rate of change of leading and trailing edge vortex strengths from the impulse matching model with Kutta conditions imposed at both the leading and trailing edge — and from the optimized impulse matching model - -.

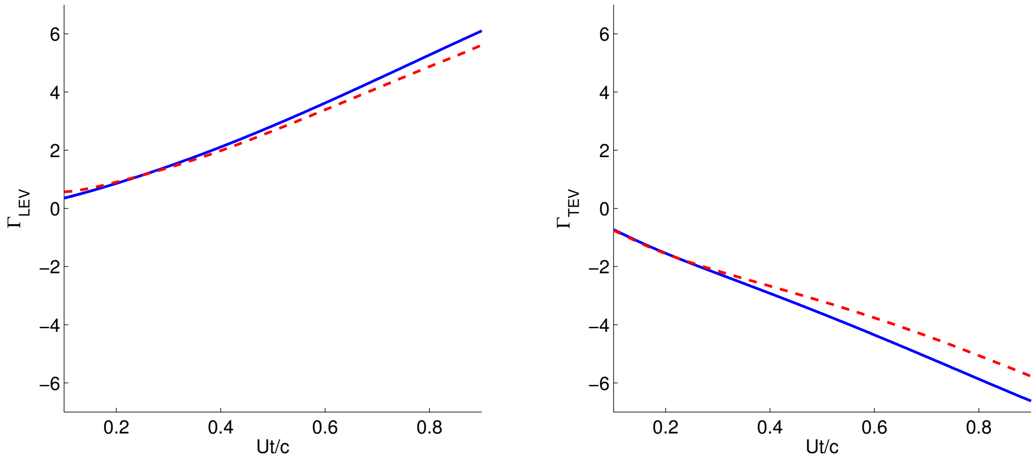

Figure 3.11: Pitching plate ($K = 0.7$) leading and trailing edge vortex strengths from the impulse matching model with Kutta conditions imposed at both the leading and trailing edge — and from the optimized impulse matching model - -.

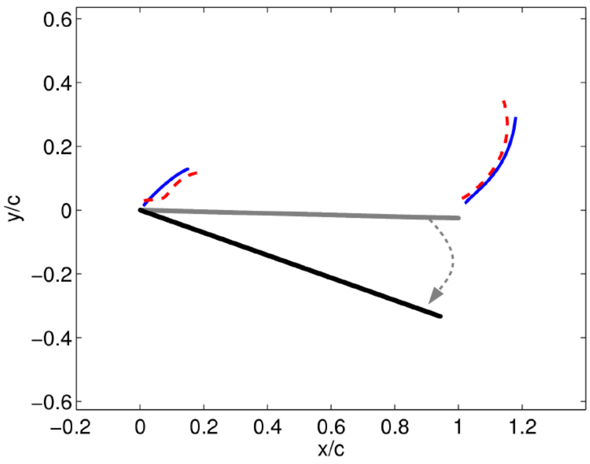

Figure 3.12: Pitching plate ($K = 0.7$) leading and trailing edge vortex trajectories from the impulse matching model with Kutta conditions imposed at both the leading and trailing edge — and from the optimized impulse matching model - -.

problem at three different fixed angles of attack: 10°, 45°, and 90°.

3.4.2.1 Impulsive Translation: $\alpha = 10^\circ$

The resulting forces from the optimized model for 10° angle of attack are presented in Figure 3.14. We find improvements in the lift prediction, but at the expense of the accuracy of the drag history. Since the impulse matching model does not account for skin friction drag, which is a dominant component at low angles of attack, this behavior does not come as a surprise. Including approximations of the viscous contribution in this model, for example by incorporating the Rayleigh problem (i.e. Stokes' first problem), will likely mitigate this issue.

Figures 3.15 and 3.16 present the inputs and states for the optimized model compared to the original. We see in all these figures that the behavior of various quantities corresponding to the LEV remain relatively unaltered. It seems that the optimization is unable to find anything better to do with either vortex, since a two point vortex model is inadequate in predicting skin friction effects. The streamlines for the optimized and original models, as

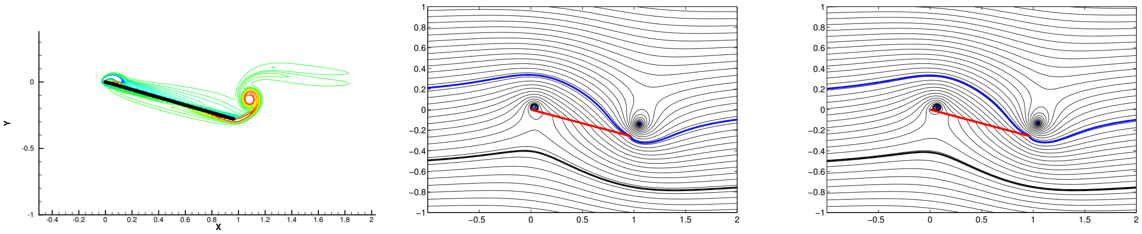

(a) VVPM ($\alpha = 15^o$) (b) IMM ($\alpha = 15^o$) (c) Optimized IMM ($\alpha = 15^o$)

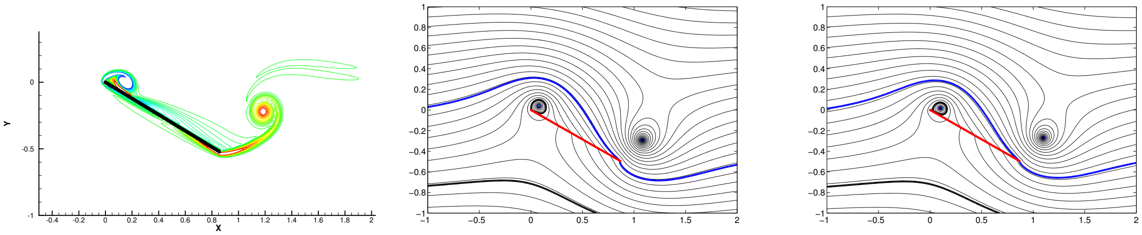

(d) VVPM ($\alpha = 30^o$) (e) IMM ($\alpha = 30^o$) (f) Optimized IMM ($\alpha = 30^o$)

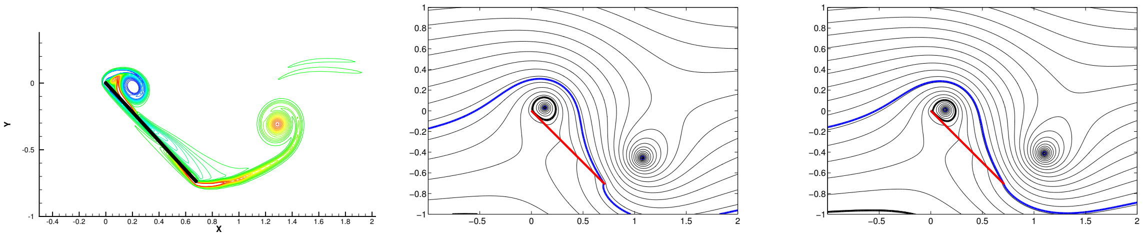

(g) VVPM ($\alpha = 45^o$) (h) IMM ($\alpha = 45^o$) (i) Optimized IMM ($\alpha = 45^o$)

Figure 3.13: Pitching plate ($K = 0.7$) snapshots at $\alpha = 15^o$, 30^o, and 45^o. The first column reports vorticity contours from the viscous vortex particle method (VVPM), while the second and third columns present streamlines from the original impulse matching model with a Kutta condition imposed (IMM) and the optimized impulse matching model (Optimized IMM), respectively. Stagnation streamlines are drawn in bold.

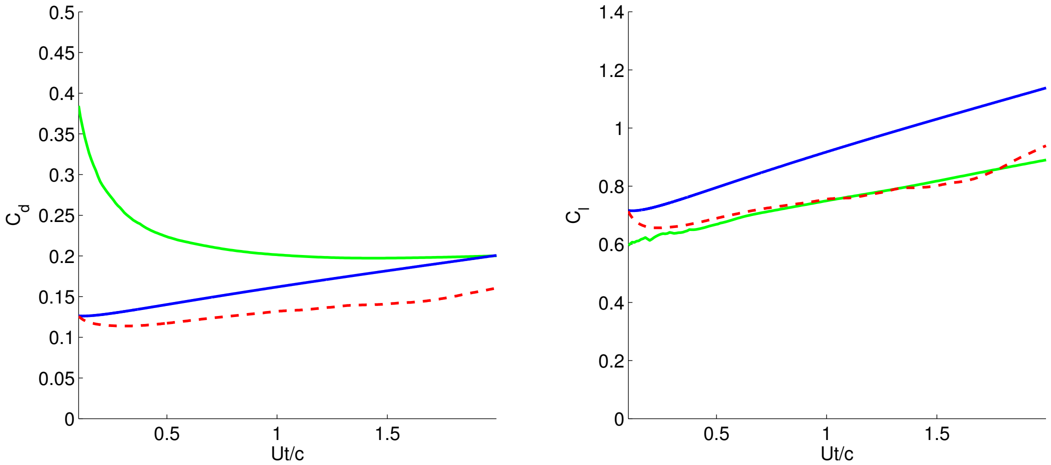

Figure 3.14: Impulsively translating plate ($\alpha = 10^{o}$) drag and lift coefficient histories associated with the VVPM data —, the impulse matching model with Kutta conditions imposed at both the leading and trailing edge —, and the optimized impulse matching model - -.

well as the vorticity contours from VVPM, are presented in Figure 3.18 for $Ut/c = 0.2$, 1.0, and 2.0. The stagnation streamline is overlaid in the vorticity contour plot for convenience.

3.4.2.2 Impulsive Translation: $\alpha = 45^{o}$

The optimized model performs remarkably better when circulatory and inertial effects outweigh skin friction effects, as seen in the force histories for the translating plate at $\alpha = 45^{o}$ in Figure 3.19. Despite the improvements attained through optimization, the quality of the force prediction begins to deteriorate after about one chord-length of travel. This mismatch can be attributed to the growth of the leading edge vortex in the vicinity of the wing. It is evident from the VVPM vorticity contours and stagnation streamlines that the onset of shedding occurs at some point between $Ut/c = 1.0$ and 2.0. The two-vortex model has difficulty capturing the effects associating with this shedding process, which is apparent in the optimal input histories of Figure 3.20. Nonetheless, the optimized model is able to capture the peel-off of the aft end of the stagnation bubble, which is highlighted in bold in Figure 3.23. It is clear that clues for establishing an appropriate shedding criterion for the vortex

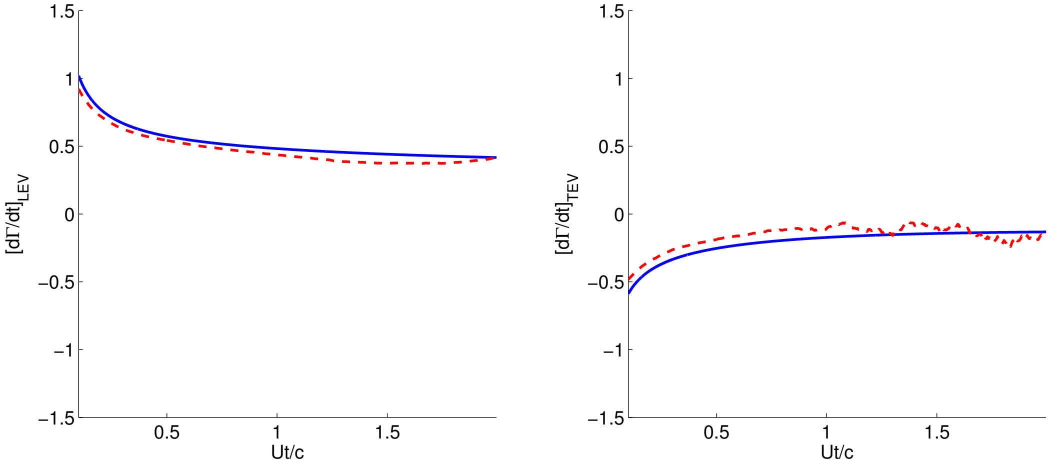

Figure 3.15: Impulsively translating plate ($\alpha = 10^o$) time rate of change of leading and trailing edge vortex strengths from the impulse matching model with the Kutta condition imposed at both the leading and trailing edge —, and the optimized impulse matching model - -.

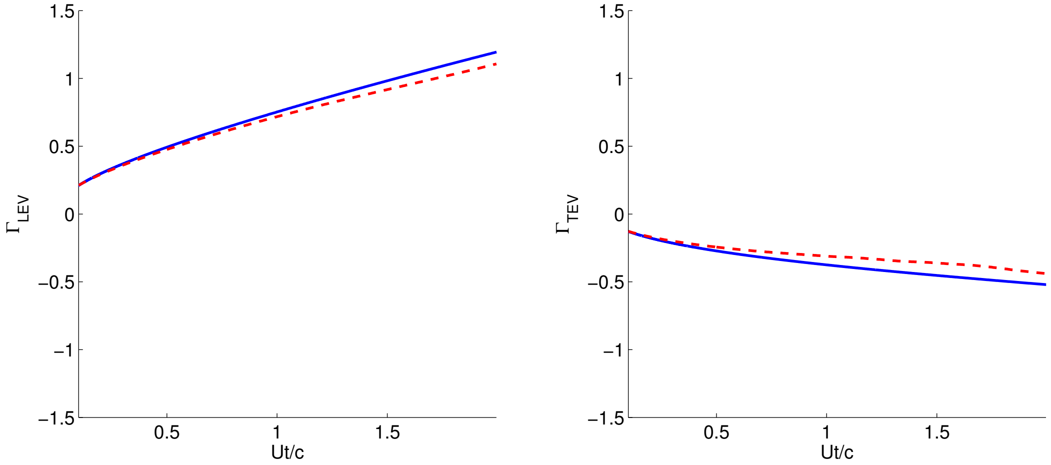

Figure 3.16: Impulsively translating plate ($\alpha = 10^o$) leading and trailing edge vortex strengths from the impulse matching model with the Kutta condition imposed at both the leading and trailing edge —, and the optimized impulse matching model - -.

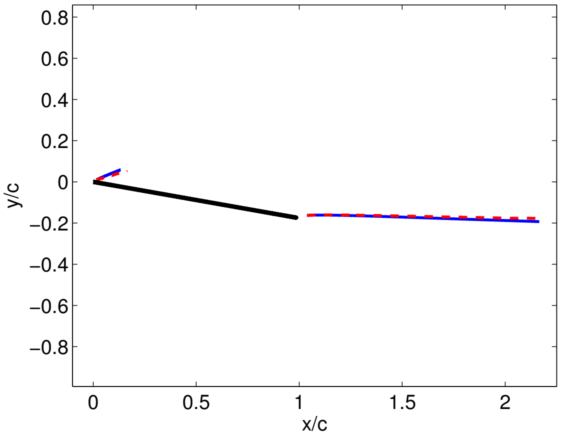

Figure 3.17: Impulsively translating plate ($\alpha = 10^o$) leading and trailing edge vortex trajectories from the impulse matching model with Kutta conditions imposed at both the leading and trailing edge — and from the optimized impulse matching model - -.

model can be extracted from the data spanning $Ut/c = 1.0$ and 2.0.

3.4.2.3 Impulsive Translation: $\alpha = 90^o$

The case of a plate translating at 90° angle of attack results in great agreement between the optimized model and the high-fidelity force curves. Figure 3.24 shows excellent agreement for the drag coefficient at all times. The lift coefficient is slightly larger than zero, even though the Kutta-based model was able to capture the exact lift for this configuration. This can be explained by considering the resulting streamlines in Figure 3.28. We observe slight asymmetries introduced to the flow as a byproduct of the optimization. This asymmetric behavior can be overcome by imposing additional symmetry constraints in the optimization problem formulation. Though doing so would enable the exact solution to be attained for this specific case, it would take away from the generality of the approach.

The time-rates of change of the vortex strengths remain quite close to the Kutta predicted results, as seen in Figure 3.25. The primary contributing factor in achieving better agreement

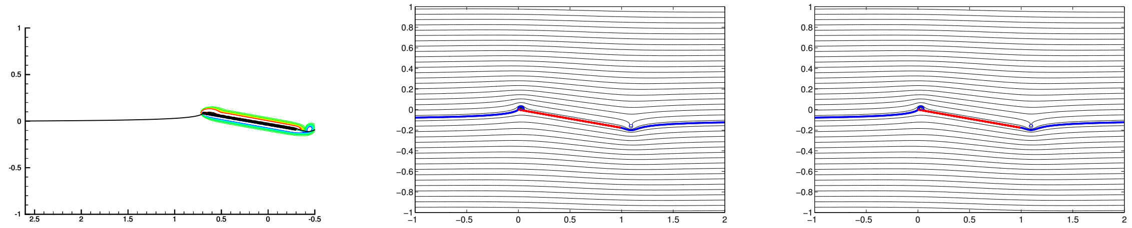

(a) VVPM ($Ut/c = 0.2$) (b) IMM ($Ut/c = 0.2$) (c) Optimized IMM ($Ut/c = 0.2$)

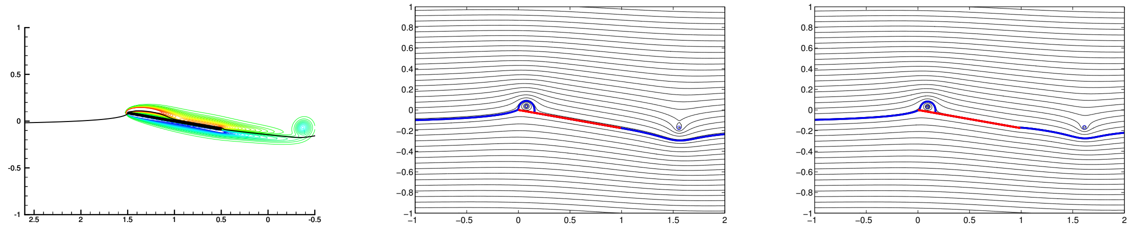

(d) VVPM ($Ut/c = 1.0$) (e) IMM ($Ut/c = 1.0$) (f) Optimized IMM ($Ut/c = 1.0$)

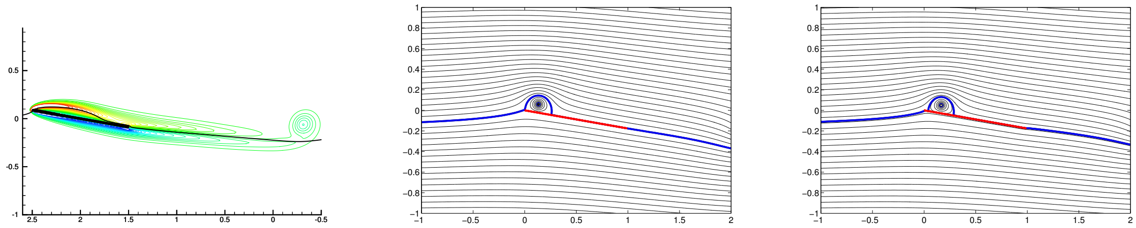

(g) VVPM ($Ut/c = 2.0$) (h) IMM ($Ut/c = 2.0$) (i) Optimized IMM ($Ut/c = 2.0$)

Figure 3.18: Impulsively translating plate ($\alpha = 10^o$) at $Ut/c = 0.2$, 1.0, and 2.0. The first column reports vorticity contours from the viscous vortex particle method (VVPM), while the second and third columns present streamlines from the original impulse matching model with a Kutta condition imposed (IMM) and the optimized impulse matching model (Optimized IMM), respectively. Stagnation streamlines are drawn in bold.

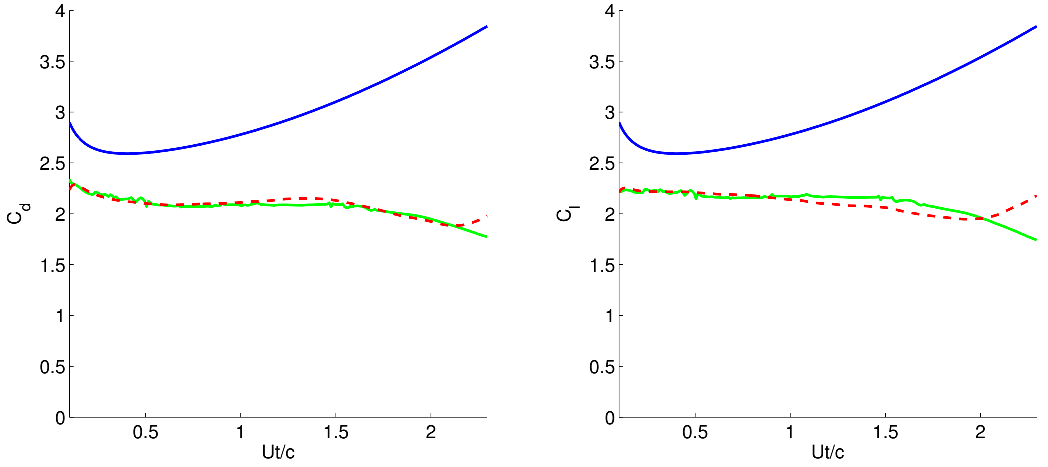

Figure 3.19: Impulsively translating plate ($\alpha = 45^o$) drag and lift coefficient histories associated with the VVPM data —, the impulse matching model with Kutta conditions imposed at both the leading and trailing edge —, and the optimized impulse matching model - -.

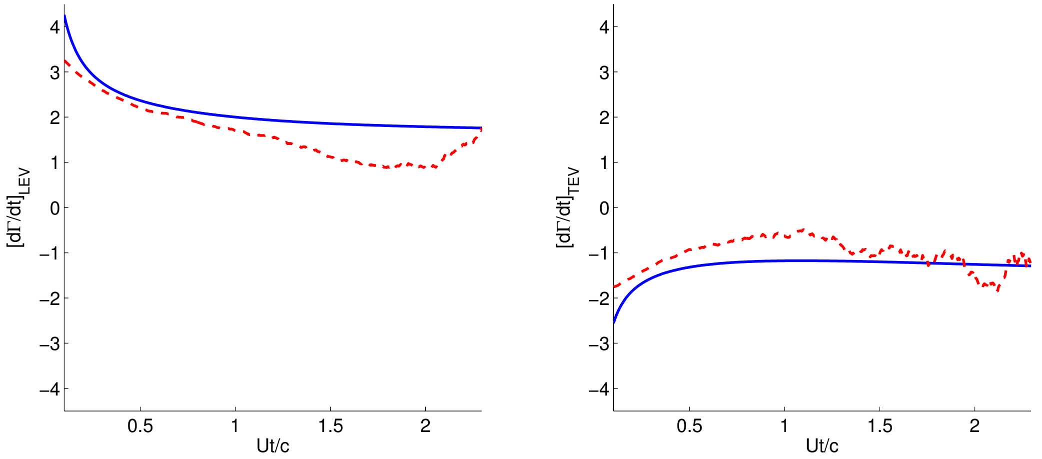

Figure 3.20: Impulsively translating plate ($\alpha = 45^o$) time rate of change of leading and trailing edge vortex strengths from the impulse matching model with the Kutta condition imposed at both the leading and trailing edge —, and the optimized impulse matching model - -.

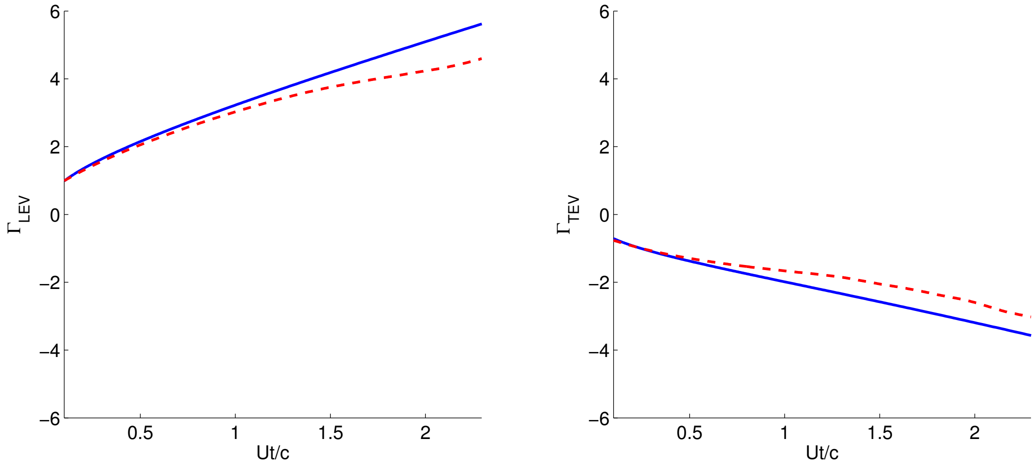

Figure 3.21: Impulsively translating plate ($\alpha = 45^o$) leading and trailing edge vortex strengths from the impulse matching model with the Kutta condition imposed at both the leading and trailing edge —, and the optimized impulse matching model - -.

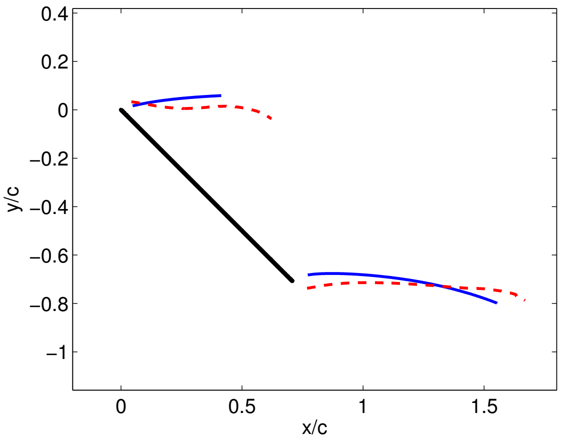

Figure 3.22: Impulsively translating plate ($\alpha = 45^o$) leading and trailing edge vortex trajectories from the impulse matching model with Kutta conditions imposed at both the leading and trailing edge — and from the optimized impulse matching model - -.

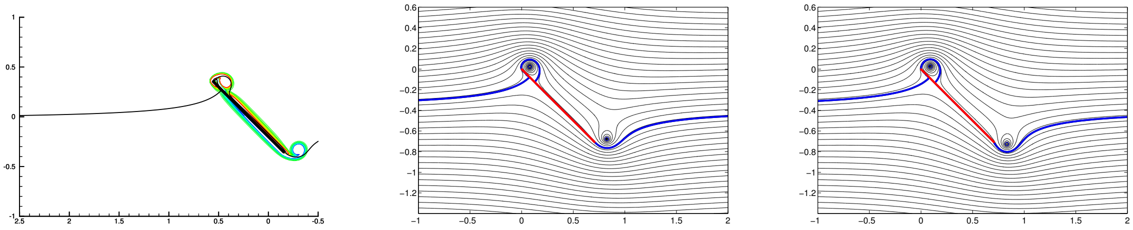

(a) VVPM ($Ut/c = 0.2$) (b) IMM ($Ut/c = 0.2$) (c) Optimized IMM ($Ut/c = 0.2$)

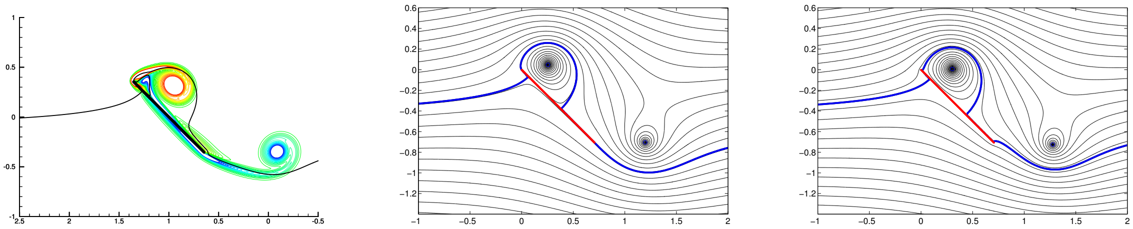

(d) VVPM ($Ut/c = 1.0$) (e) IMM ($Ut/c = 1.0$) (f) Optimized IMM ($Ut/c = 1.0$)

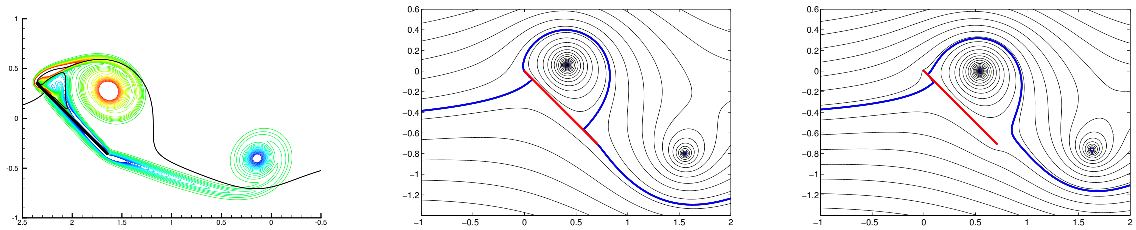

(g) VVPM ($Ut/c = 2.0$) (h) IMM ($Ut/c = 2.0$) (i) Optimized IMM ($Ut/c = 2.0$)

Figure 3.23: Impulsively translating plate ($\alpha = 45^o$) at $Ut/c = 0.2$, 1.0, and 2.0. The first column reports vorticity contours from the viscous vortex particle method (VVPM), while the second and third columns present streamlines from the original impulse matching model with a Kutta condition imposed (IMM) and the optimized impulse matching model (Optimized IMM), respectively. Stagnation streamlines are drawn in bold.

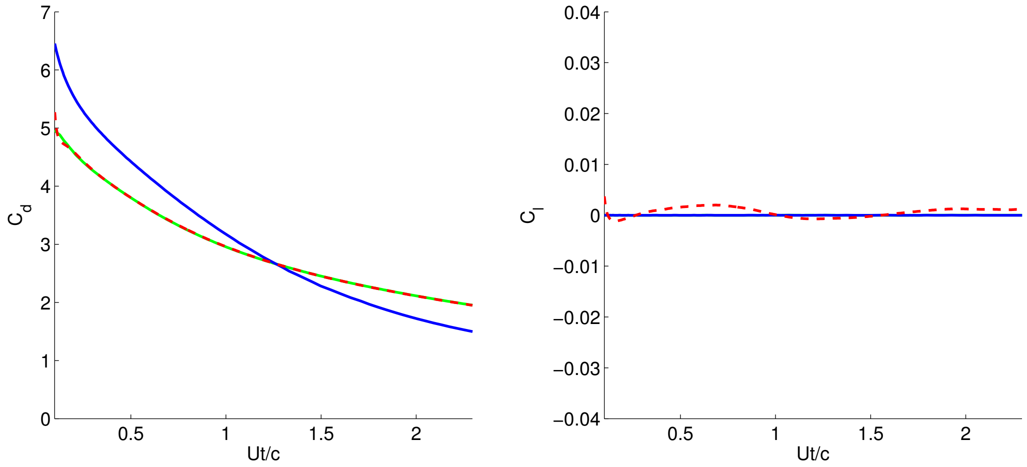

Figure 3.24: Impulsively translating plate ($\alpha = 90^o$) drag and lift coefficient histories associated with the VVPM data —, the impulse matching model with Kutta conditions imposed at both the leading and trailing edge —, and the optimized impulse matching model - -.

in this configuration seems to be the initial position of both edge vortices (c.f. Figure 3.27), though the slight alterations to the time-rate of change of the vortex strengths also play a role.

3.5 Remaining Challenges and Paths to Enhancement

Despite the progress made on vortex model optimization in the present study, several challenges remain to be addressed. In the present section, we address the issues of expanding the optimization time-window, introducing subsequent vortex shedding within the optimization framework, and ascertaining a modified Kutta condition from the optimization results reported.

3.5.1 Convergence for Large Time Windows and Early Times

All of the optimization results presented for the pitch-up maneuver in the previous section spanned a truncated time window. That is to say, the time window of optimization was

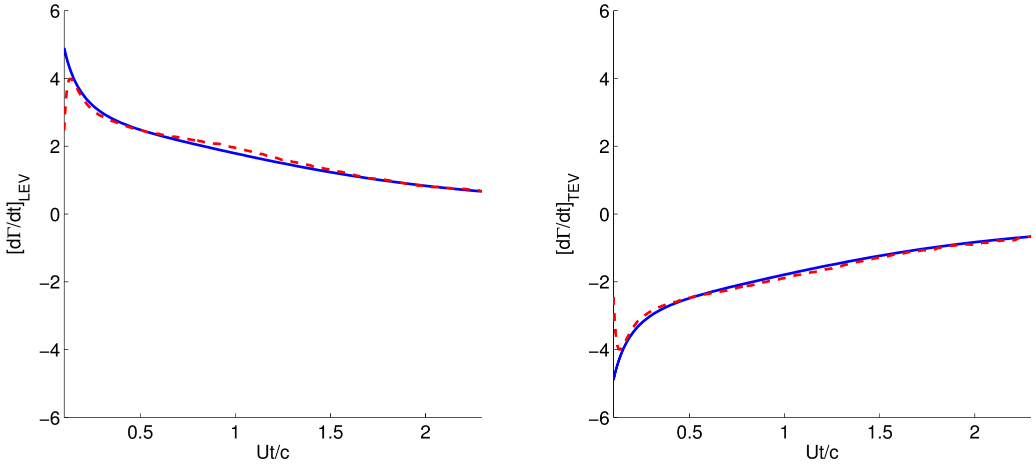

Figure 3.25: Impulsively translating plate ($\alpha = 90^o$) time rate of change of leading and trailing edge vortex strengths from the impulse matching model with the Kutta condition imposed at both the leading and trailing edge —, and the optimized impulse matching model - -.

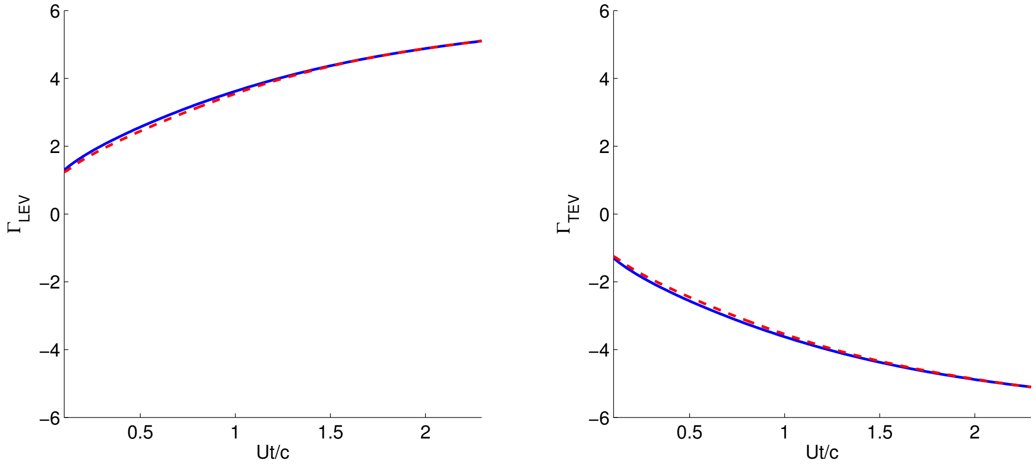

Figure 3.26: Impulsively translating plate ($\alpha = 90^o$) leading and trailing edge vortex strengths from the impulse matching model with the Kutta condition imposed at both the leading and trailing edge —, and the optimized impulse matching model - -.

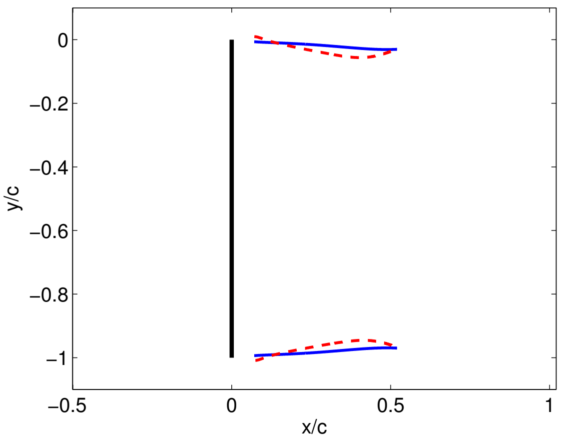

Figure 3.27: Impulsively translating plate ($\alpha = 90^o$) leading and trailing edge vortex trajectories from the impulse matching model with Kutta conditions imposed at both the leading and trailing edge — and from the optimized impulse matching model - -.

not long enough to capture the full completion of the pitch-up to 90°. Additionally, all of the optimizations of both pitch-up and impulsive translation were initiated when the wing had translated forward by 10% of its chord. From the experience gained in conducting the optimization procedure, it was determined that convergence was quite difficult for time windows larger than those reported earlier. Moreover, if convergence did result with an extended time window, the resulting solution was often unsatisfactory and yielded a larger error than deemed acceptable.

For the early-time behavior, part of the challenge can be attributed to the singular nature of the evolution equations at start-up. However, this does not fully account for the difficulty encountered, since acceptable results were difficult to attain for any optimization considering a window beginning before 10% chord of travel. This is not to say that such results are impossible to attain; rather, the sensitivity of the results to the initial iteration of input history and parameter vector was too high to yield an improved model for this early-time window. Future studies may be more fortuitous in their outcomes.

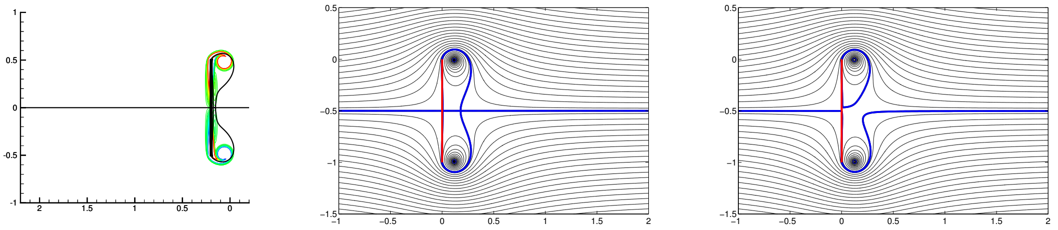

(a) VVPM ($Ut/c = 0.2$) (b) IMM ($Ut/c = 0.2$) (c) Optimized IMM ($Ut/c = 0.2$)

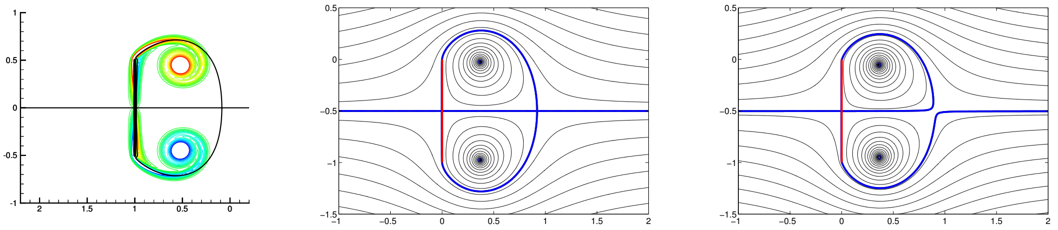

(d) VVPM ($Ut/c = 1.0$) (e) IMM ($Ut/c = 1.0$) (f) Optimized IMM ($Ut/c = 1.0$)

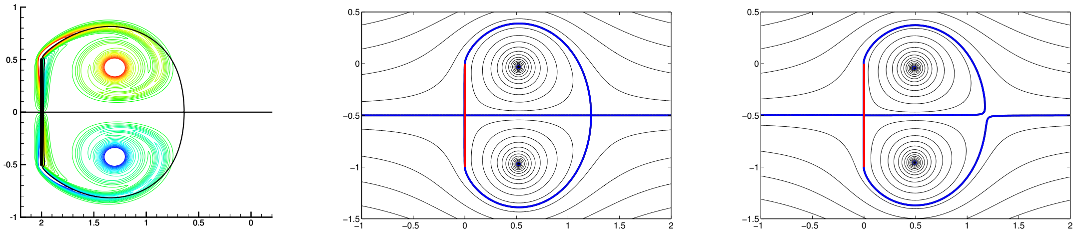

(g) VVPM ($Ut/c = 2.0$) (h) IMM ($Ut/c = 2.0$) (i) Optimized IMM ($Ut/c = 2.0$)

Figure 3.28: Impulsively translating plate ($\alpha = 90^o$) at $Ut/c = 0.2$, 1.0, and 2.0. The first column reports vorticity contours from the viscous vortex particle method (VVPM), while the second and third columns present streamlines from the original impulse matching model with a Kutta condition imposed (IMM) and the optimized impulse matching model (Optimized IMM), respectively. Stagnation streamlines are drawn in bold.

The convergence difficulty associated with later time behavior has a more physical explanation associated with it. One of the challenges with the later time behavior is the onset of vortex shedding. It is hypothesized that the vortex model would be able to better characterize the force response if a means of vortex shedding were included in the optimization model. A framework for introducing shedding into the vortex optimization framework will be discussed in Section 3.5.3. However, this framework will highly depend upon the ability to treat early-time behavior because the growth of a new vortex from the edge will be akin to the start-up of the vortex that was just released from the same edge. Before delving into a discussion of strategies for including vortex shedding, we present the results of a simple idea that has led to fruitful results.

3.5.2 Extending Time Windows via Stitching

As discussed in Section 3.5.1, the vortex shedding model will likely remain unsuccessful until the optimization procedure can better handle early-time behaviors. At least temporarily, a different approach can be considered. In the present section, we introduce a simple "stitching" method that has proven to work quite well for extending the time window to include the completion of the pitch-up maneuver.

The main premise of the proposed method is to decompose the full time window into several more manageable ones. For the present study, we consider decompose the full time-domain $[t_o, t_f]$ into two time windows $[t_1, t_2)$ and $[t_2, t_3]$, where $t_1, t_2, t_3 \in [t_o, t_f]$ (cf. Figure 3.29). The vortex optimization procedure can then be applied to each of these time windows independently, coupled only by means of a continuity constraint on the trajectory of the state vector (i.e. $\mathbf{x}(t_3) = \mathbf{x}(t_2)$). Such an approach is slightly less restrictive than the original procedure in that it allows from a finite number of discontinuities in the inputs at times corresponding to the intersection of the time windows (i.e. t_2 for the case presented here).

The results of the stitching procedure are reported in Figures 3.30–3.35. For both $K = 0.2$

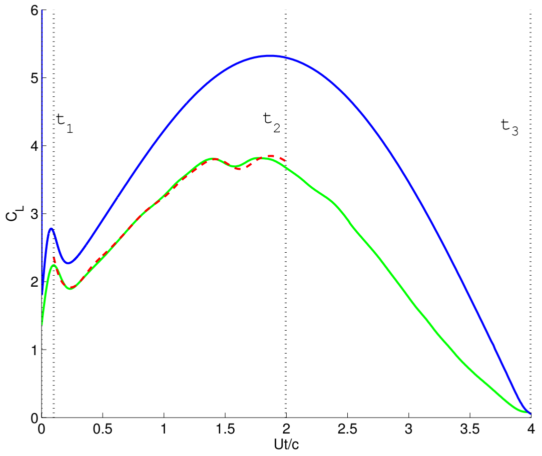

Figure 3.29: The decomposition of the full time-domain, $[t_o, t_f]$, into two smaller windows, $[t_1, t_2)$ and $[t_2, t_3]$. We currently assume that t_1 and t_2 are those corresponding to the time window for the original model optimization. Here we show the ($K = 0.2$) pitch-up maneuver lift history corresponding to the VVPM data —, the impulse matching model with Kutta conditions imposed at both the leading and trailing edge —, and the original optimized impulse matching model - -.

and $K = 0.7$, we have taken t_1 and t_2 from the original vortex model optimization time windows considered in Section 3.4. We see that the later time behavior is improved from the original impulse matching model, though the second time window tends to have a larger mean squared error than the first time window. Again, this is attributed to the need to model vortex shedding. The optimal input history is shown alongside the strength history to demonstrate that the discontinuity in the input at t_2 remains fairly small and does not affect the smoothness of the strength of either vortex.

3.5.3 A Framework for Subsequent Vortex Shedding

In the previous section, we demonstrated a method for overcoming some of the convergence challenges associated with large time windows. Despite this capability, it remains of interest

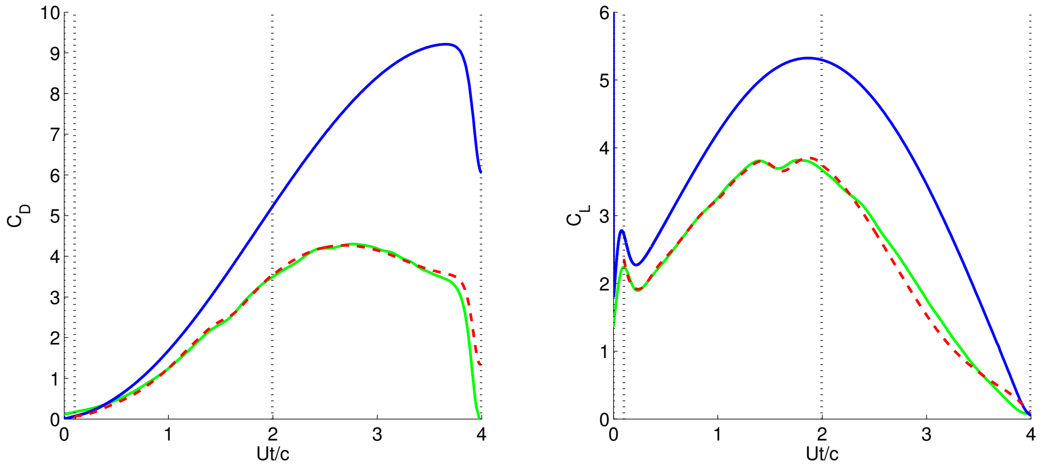

Figure 3.30: Pitching plate ($K = 0.2$) drag and lift coefficient histories associated with the VVPM data —, the impulse matching model with Kutta conditions imposed at both the leading and trailing edge —, and the stitch-optimized impulse matching model - -.

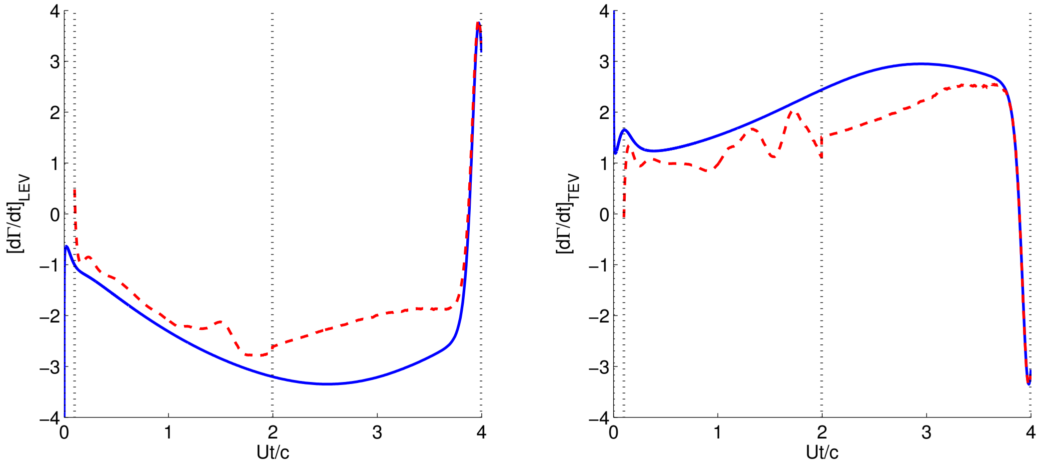

Figure 3.31: Pitching plate ($K = 0.2$) time rate of change of leading and trailing edge vortex strengths from the impulse matching model with Kutta conditions imposed at both the leading and trailing edge — and from the stitch-optimized impulse matching model - -.

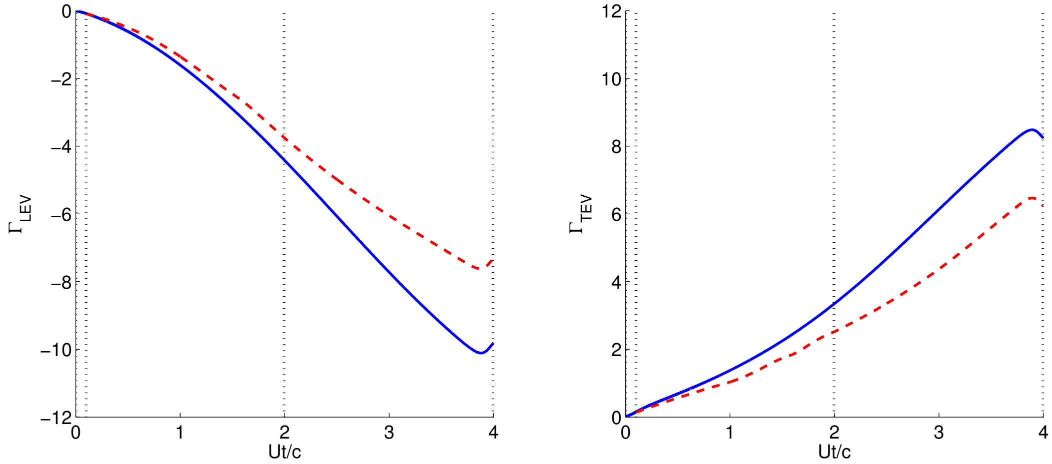

Figure 3.32: Pitching plate ($K = 0.2$) leading and trailing edge vortex strengths from the impulse matching model with Kutta conditions imposed at both the leading and trailing edge — and from the stitch-optimized impulse matching model - -.

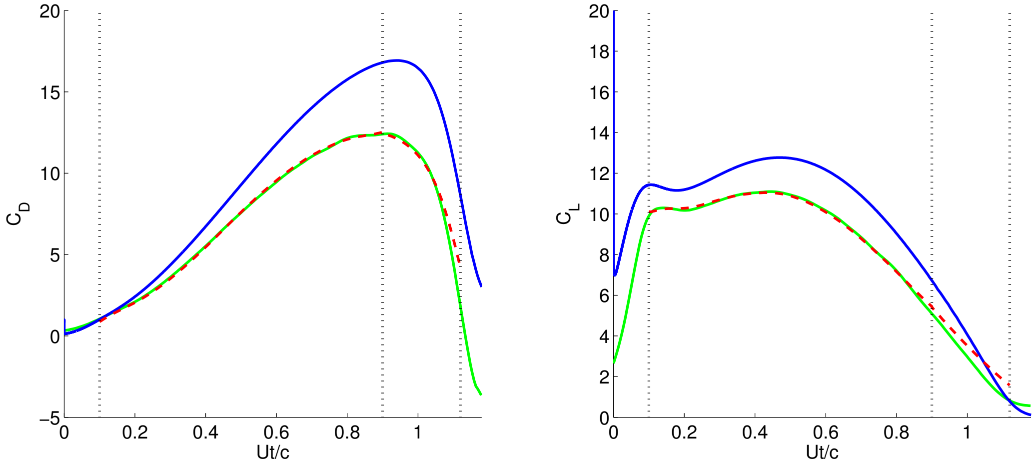

Figure 3.33: Pitching plate ($K = 0.7$) drag and lift coefficient histories associated with the VVPM data —, the impulse matching model with Kutta conditions imposed at both the leading and trailing edge —, and the stitch-optimized impulse matching model - -.

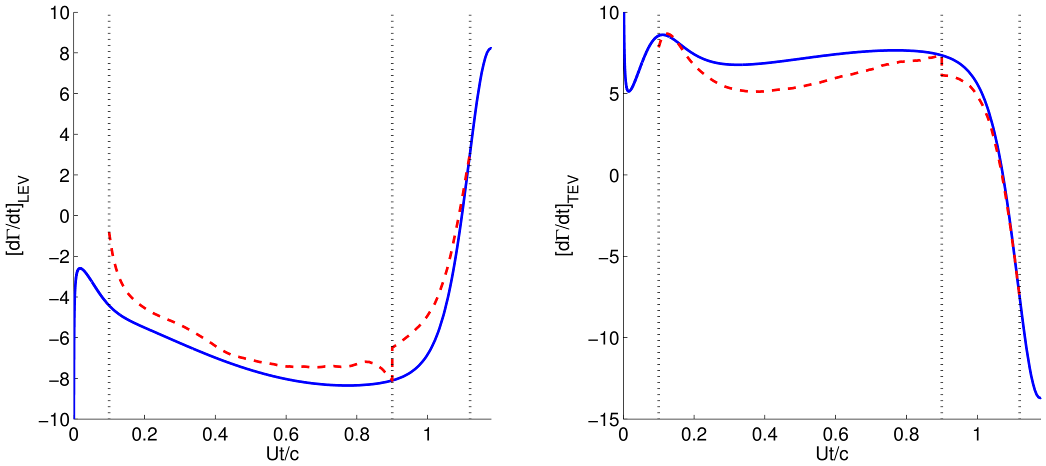

Figure 3.34: Pitching plate ($K = 0.7$) time rate of change of leading and trailing edge vortex strengths from the impulse matching model with Kutta conditions imposed at both the leading and trailing edge — and from the stitch-optimized impulse matching model - -.

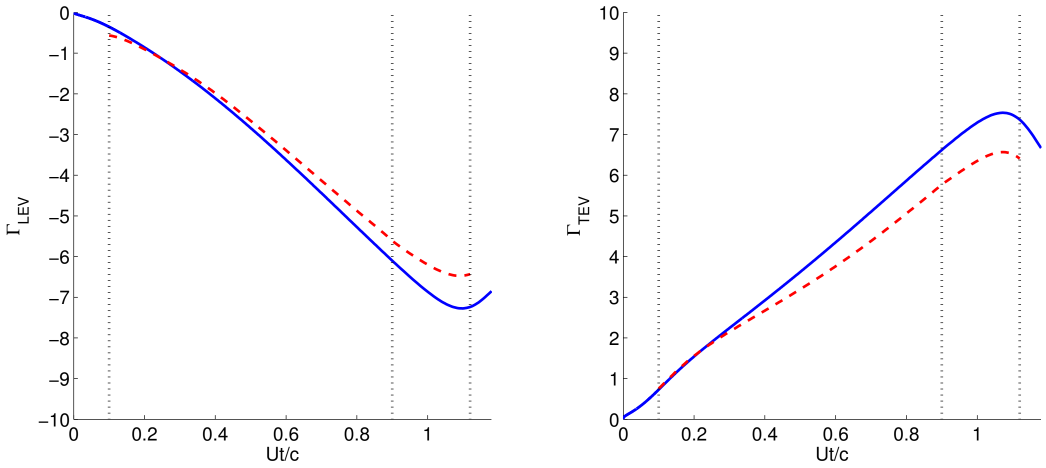

Figure 3.35: Pitching plate ($K = 0.7$) leading and trailing edge vortex strengths from the impulse matching model with Kutta conditions imposed at both the leading and trailing edge — and from the stitch-optimized impulse matching model - -.

to introduce a means of vortex shedding within the optimization framework. Not only will this provide potential for improving the predictions over the stitch-optimized results, but it also offers a means of gaining further physical insight into the nature of vortex shedding. We have already discussed the need to better handle early-time behavior before a successful vortex shedding optimization can be conducted. Nonetheless, we develop an approach for including vortex shedding such that it can be applied when the challenges associated with vortex start-up are resolved.

The problem of vortex shedding can be introduced into the current optimization framework by considering the shedding instant as an optimization parameter. This can be viewed in the same manner as the time-domain decomposition into multiple time-windows, as in the stitching case. However, now the second time window will follow the impulse matching evolution equations in the presence of an additional vortex, with a constant strength, while the first time window is treated as before. We will first consider the general framework of optimal model switching developed in [XA04] in Section 3.5.3.1, then in Section 3.5.3.2 we discuss how this framework can be used to introduce vortex shedding within the optimization problem.

3.5.3.1 The Optimal Switching Control Problem

Consider the switched system consisting of the following subsystems

$$\dot{x} = f_i(x, u),\ \ f_i : \mathbb{R}^n \times \mathbb{R}^m \to \mathbb{R}^m,\ \ i \in I := \{1, 2, \ldots, M\}\,. \tag{3.27}$$

The optimal switching control problem consists of determining the optimal control input u, in addition to an optimal switching sequence in $t \in [t_o, t_f]$ that specifies the sequence of active subsystems. This switching sequence is defined as

$$\sigma := ((t_o, i_o), (t_1, i_1), \ldots, (t_K, i_K)) \tag{3.28}$$

where $0 \leq K < \infty$, $t_o \leq t_1 \leq \cdots \leq t_K \leq t_f$, and $i_k \in I$ for $k = 0, 1, \ldots, K$. Here, (t_k, i_k) denotes that at time t_k the system switched from subsystem i_{k-1} to subsystem i_k for the time interval $[t_k, t_{k+1})$ (except when $k = K$, for which the interval is $[t_K, t_f]$).

The optimal switching control problem can now be stated in the following manner. Consider a switched system consisting of subsystems $\dot{x} = f_i(x, u)$, $i \in I$. Given a fixed time interval $[t_o, t_f]$ and a specified sequence of active subsystems $(i_o, i_1, \ldots, i_K)$, find a continuous input $u \in \mathcal{U}_{[t_o,t_f]}$ and switching instants $t_1, \ldots, t_K$ such that

$$J = \psi(x(t_f)) + \int_{t_o}^{t_f} g(x, u)\mathrm{d}t \tag{3.29}$$

is minimized.

3.5.3.2 A Framework to Accommodate Vortex Shedding

In the spirit of the optimal switching control problem, we formulate a similar optimization problem for improving our vortex model by accounting for the shedding of multiple vortices. To do so, consider the switched system consisting of the following two subsystems, defined with respect to differing state and input vectors, (x_1, u_1) and (x_2, u_2),

$$\dot{x}_1 = f_1(x_1, u_1), t \in [t_o, t_1) \tag{3.30}$$

$$\dot{x}_2 = f_2(x_2, u_2), t \in [t_1, t_f] \tag{3.31}$$

The switching sequence here is simply $\sigma = (t_o, i_o, t_1, i_1)$ since the subsystems will only switch once. We have intentionally made a distinction between (x_1, u_1) and (x_2, u_2) in an effort to emphasize, from a modeling standpoint, the release of one vortex “in exchange for” the introduction of another. The problem now is to determine the inputs u_1 and u_2, the initial conditions on the states $x_1(t_o)$ and $x_2(t_1)$, and the switching instant t_1, such that

$$J = \int_{t_o}^{t_1} g(x_1, u_1)\mathrm{d}t + \int_{t_1}^{t_f} g(x_2, u_2)\mathrm{d}t \tag{3.32}$$

is minimized.

We can rewrite this last statement as

$$\begin{aligned}
\min_{u_1,u_2,x_1(t_o),x_2(t_o),t_1} J &= \min_{u_1,u_2,x_1(t_o),x_2(t_o),t_1} \left[\int_{t_o}^{t_1} g(x_1,u_1)\mathrm{d}t + \int_{t_1}^{t_f} g(x_2,u_2)\mathrm{d}t\right] && (3.33)\\
&= \min_{t_1}\left\{\min_{u_1,u_2,x_1(t_o),x_2(t_o)} \left[\int_{t_o}^{t_1} g(x_1,u_1)\mathrm{d}t + \int_{t_1}^{t_f} g(x_2,u_2)\mathrm{d}t\right]\right\} && (3.34)\\
&= \min_{t_1}\left\{\min_{u_1,x_1(t_o)} \int_{t_o}^{t_1} g(x_1,u_1)\mathrm{d}t + \min_{u_2,x_2(t_o)} \int_{t_1}^{t_f} g(x_2,u_2)\mathrm{d}t\right\} && (3.35)
\end{aligned}$$

Though the original form should be used for practical implementation, writing the minimization in this form demonstrates the equivalent nature of the problem to the optimization we have already considered. That is, this “switching” problem nests two optimization problems with the same form we treated previously, with an additional parameter optimization for t_1.

It should be noted that this framework can be extended arbitrarily to accommodate any number of vortex shedding events. Of course the practicality of computing a solution for multiple shedding events may be a limiting factor. In addition to convergence properties having a greater potential for being poor, the computational expense grows greatly with the addition of each switching event. In considering a large number of shedding events, one may also consider framing the problem as a periodic optimal control problem. Such an approach will rely on the assumption of periodicity in the vortex shedding and force histories for all times, including start-up. Although this may seem like a rather crude assumption, the solution of the periodic optimal control problem will undoubtedly be much more tractable from a computational standpoint and, thus, more likely to yield a solution.

3.5.4 Distilling a Modified Kutta Condition

All of the optimized vortex models require *a priori* data for a given maneuver in order to be constructed. In this sense, the vortex optimization framework is not suitable for developing standalone models. Rather, the method is useful in guiding the design of a better model. For example, the results of the optimized vortex models give hope for discovering a more appropriate condition to apply at the leading and trailing edges for pitch-up and impulsive translation. A rudimentary study of such a model comes from our observation that the stagnation point towards the front of the wing is slightly aft of the leading edge. With this information in hand, we set out to study the effects of imposing various stagnation point locations for the fore-section of the wing. In this study we consider the pitch-up maneuver for $K = 0.2$ in Figure 3.36 and $K = 0.7$ in Figure 3.37. Additionally, we consider impulsive translation at a fixed angle of attack with $\alpha = 45^o$ in Figure 3.38 and $\alpha = 90^o$ in Figure 3.39. The $\alpha = 10^o$ is not considered here, since we have already determined that a two point vortex model alone is inadequate for modeling the skin friction forces associated with this low angle of attack maneuver.

Based on this simple model, we see that the force predictions can be improve in some instances, but only for a short portion of the maneuver. This is not terribly unforeseen, since based on observations of the optimization results, the leading edge stagnation point seems to meander along the fore-section of the wing. This makes a study of a fixed stagnation point location somewhat dubious, a crude approximation at the best. Future efforts will likely need to consider a functional approximation to the stagnation point location as a function of various kinematic and vortex parameters. Perhaps a monotonic or sinusoidal model of the stagnation point position would yield better results, while keeping the model relatively simple. Another approach may be to incorporate the notion of optimal switching control to determine the best model for various segments of a maneuver. The models to be switched could be monotonically increasing and decreasing functions for the stagnation point location.

3.6 Conclusions

In this chapter, we have formulated a systematic framework for vortex model improvement based on variational principles and optimal control theory. We have demonstrated the optimization method's merits by demonstrating improvements to the impulse matching model, developed by Eldredge and Wang, for predicting the forces resulting from the pitching and/or translation of a two-dimensional plate. The force computations resulting from the optimized model match those predicted by high-fidelity simulations remarkably well for most of the

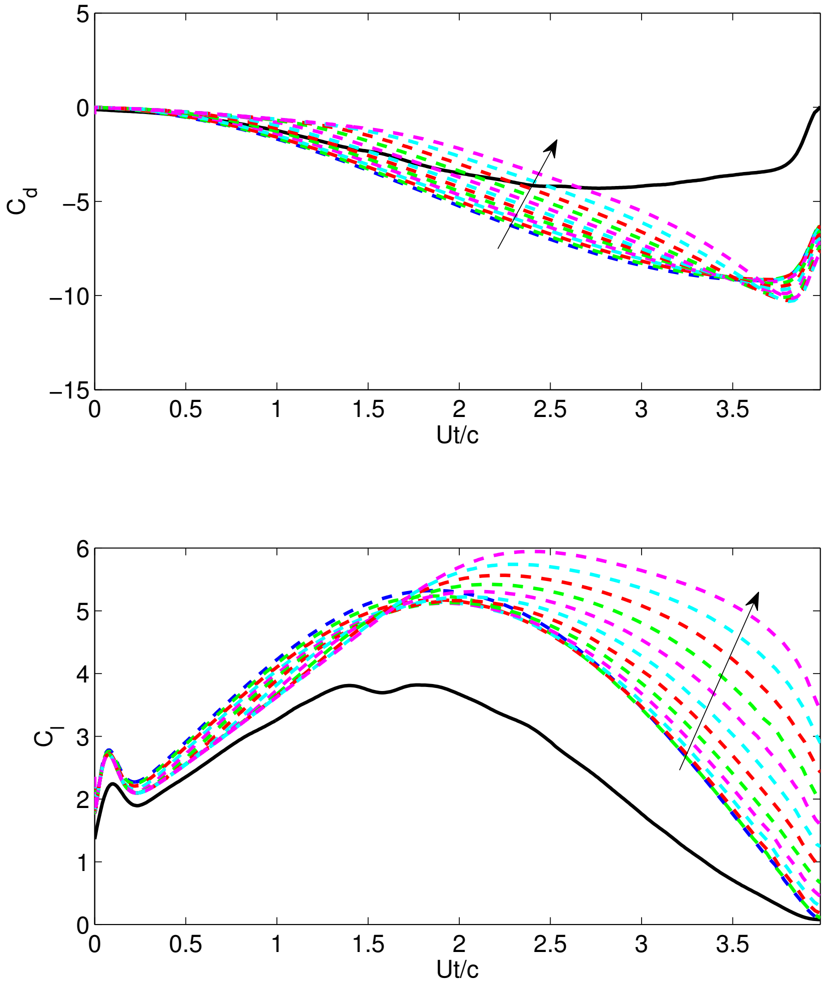

Figure 3.36: Lift and drag histories associated with a pitch-up maneuver ($K = 0.2$) predicted using an impulse matching model with modified stagnation point specifications. The solid line represents the “true” force response, while the dashed lines correspond to model-predicted results using different regularity conditions. The regularity point at the leading edge is varied from $\theta = 0^{\mathrm{o}}$ (i.e. the Kutta condition) in increments of 3^{o} in the circle plane, while the trailing edge has a Kutta condition condition imposed across all results. The arrow denotes the direction of increasing θ.

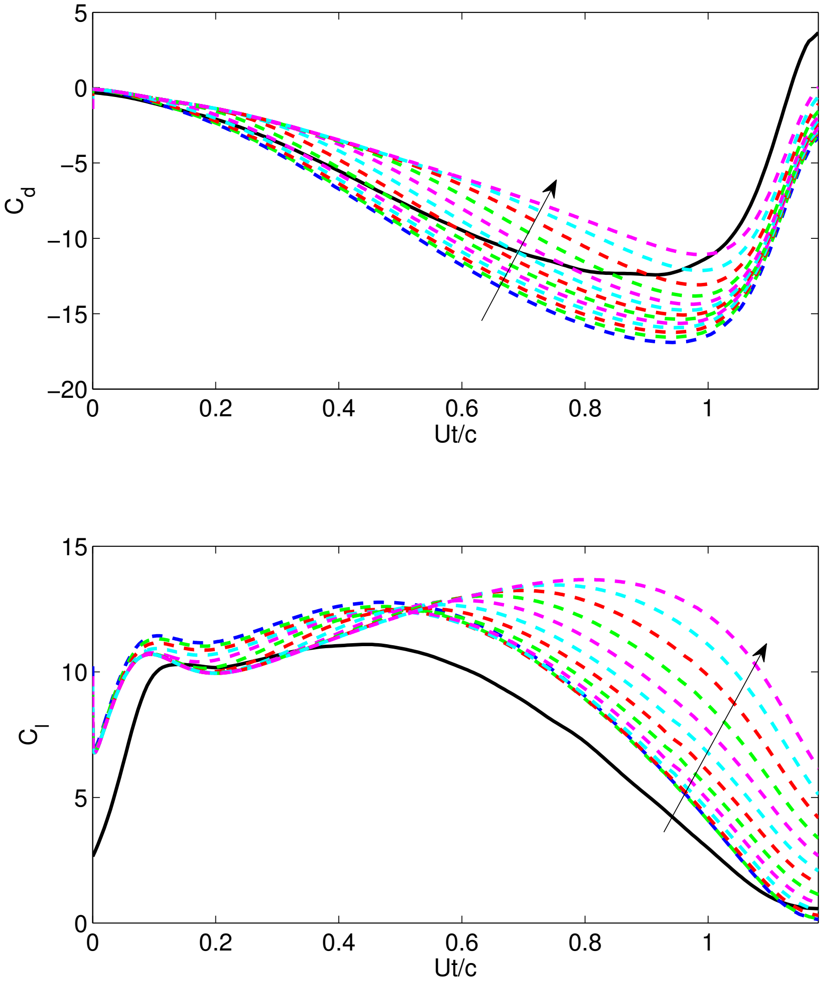

Figure 3.37: Lift and drag histories associated with a pitch-up maneuver ($K = 0.7$) predicted using an impulse matching model with modified stagnation point specifications. The solid line represents the “true” force response, while the dashed lines correspond to model-predicted results using different regularity conditions. The regularity point at the leading edge is varied from $\theta = 0^o$ (i.e. the Kutta condition) in increments of 3^o in the circle plane, while the trailing edge has a Kutta condition condition imposed across all results. The arrow denotes the direction of increasing θ.

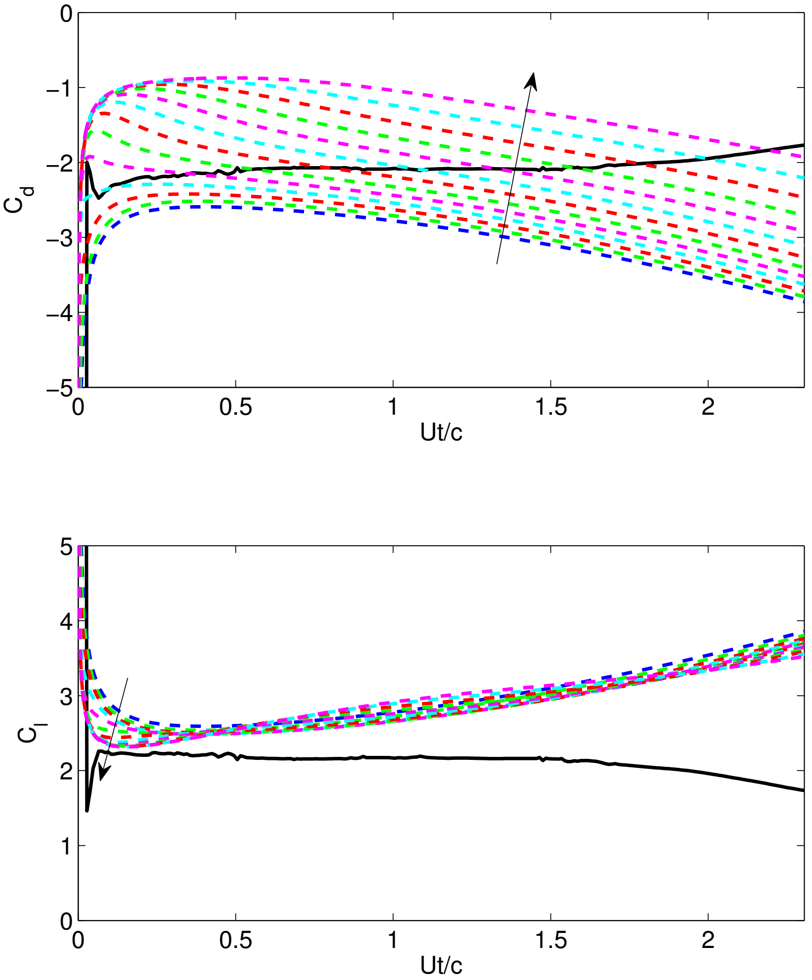

Figure 3.38: Lift and drag histories associated with impulsive translation at a fixed angle of attack ($\alpha = 45^o$) predicted using an impulse matching model with modified stagnation point specifications. The solid line represents the "true" force response, while the dashed lines correspond to model-predicted results using different regularity conditions. The regularity point at the leading edge is varied from $\theta = 0^o$ (i.e. the Kutta condition) in increments of 3^o in the circle plane, while the trailing edge has a Kutta condition condition imposed across all results. The arrow denotes the direction of increasing θ.

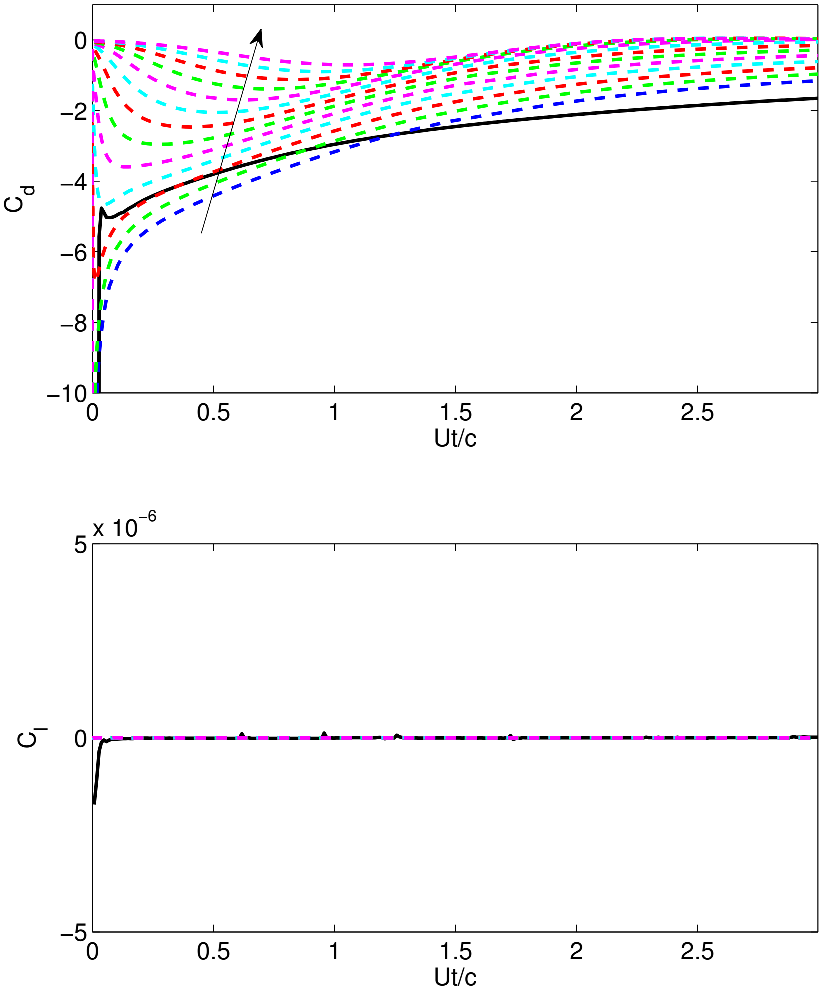

Figure 3.39: Lift and drag histories associated with impulsive translation at a fixed angle of attack ($\alpha = 90^o$) predicted using an impulse matching model with modified stagnation point specifications. The solid line represents the "true" force response, while the dashed lines correspond to model-predicted results using different regularity conditions. The regularity point at the leading edge is varied from $\theta = 0^o$ (i.e. the Kutta condition) in increments of 3^o in the circle plane, while the trailing edge is modified so as to preserve symmetry across the plate in the physical plane. The arrow denotes the direction of increasing θ.

flows considered. The only short-comings arose for low angle of attack translation (i.e. when the skin friction drag was a dominant factor) and for flows undergoing vortex shedding. Despite these "short-comings," the optimized model consistently predicted the forces better than the original impulse matching model for all the cases considered. Moreover, the quality of the results obtained using only six degrees of freedom is impressive, considering that the fully-resolved high-fidelity simulations used between 10^5–10^6 degrees of freedom at $Re = 1000$.

Difficulties associated with convergence for early-time behavior as well as for extended time windows proved challenging. In spite of the fact that the early-time issues have yet to be resolved, a "stitching" methodology was devised to allow the optimization to progress for extended time windows. The optimization framework developed here is only represents a small aspect of the capabilities of the model improvement paradigm. For example, the present method can be extended to incorporate vortex shedding, as discussed in Section 3.5.3. Although we suggested techniques for accommodating vortex shedding within the optimization framework, practical implementation will require a better handling of early-time optimizations. Resolving vortex growth at early-times remains the essential obstacle to be surmounted, at least for the present model.

Prior to this work, the Kutta condition was the gold standard for determining the strengths of developing point vortices. Here, we have provided a framework for relaxing the Kutta condition and determining the vortex strengths empirically from high-fidelity numerical computations, instead. As such, the model optimization methodology presented serves as a framework for model reduction, with a phenomenological basis. By optimizing the low-order point vortex model for unsteady wing maneuvers, we have highlighted the shortcomings of applying Kutta conditions at the leading and trailing edges of flows with LEV and TEV evolution. We considered a simple approach for a modified Kutta condition from the optimized models, but much progress still remains to be made in this area.

The model optimization framework can also be extended to other systems of interest, such as finite aspect ratio wings. To take such a step, however, will require the appropriate vortex models to represent such flows. Necessary models will likely follow an unsteady modified lifting line [Jon40, Dor66] or vortex panel approach, augmented with the development and influence of the LEV. The key assumption in accommodating finite aspect ratio wings within the optimization framework is imposing an *a priori* spanwise distribution on the strength distribution of wake vortex system. That is,

$$\boldsymbol{\gamma}(y,t) := \phi(y) \begin{bmatrix} \Gamma_{\mathrm{LEV}}(t) & \Gamma_{\mathrm{TEV}}(t) \end{bmatrix}^{\mathsf{T}} \tag{3.36}$$

where $\phi(y)$ is the assumed spanwise distribution, which can be scaled by the vortex strength $\Gamma_{\mathrm{LEV}}(t)$ or $\Gamma_{\mathrm{TEV}}(t)$ to yield the strength distribution in the wake $\boldsymbol{\gamma}(y,t)$ emanating from the corresponding edge. In doing so, the control input $\mathbf{u}(t)$ can be defined as before, consisting of the two scalar functions $\dot{\Gamma}_{\mathrm{LEV}}(t)$ and $\dot{\Gamma}_{\mathrm{LEV}}(t)$.

It is clear that the availability of this vortex model optimization technique holds great promise for vortex-based aero- and hydrodynamic estimation. The generality of the model improvement technique will undoubtedly provide guidance in the modeling of other vortex systems of practical interest. By having a systematic means of improving vortex models to better predict real-world physics, the vortex-based estimation paradigm stands to have the modeling capabilities necessary for making reliable real-time flow estimates.

CHAPTER 4

Simulation Testbed: A Vortex Panel-Particle Method

As the name suggests, the panel-particle method developed in this section merges the capabilities of vortex panel methods with those of vortex particle methods to establish a computational tool suitable for studying unsteady multi-body aero- and hydrodynamic problems. The vortex panel method, first developed by Hess and Smith in the 1960's [Smi90], will be used to model the bound vorticity associated with bodies, while the free-vorticity of the wake is represented by vortex particles. The vortex particle method, first considered by Rosenhead in 1931 [Ros31], is free from the topological constraints of a panel representation, thus making it a good candidate for wake representations in multi-body simulations. A vast breadth of literature exists on both vortex panel and vortex particle methods. The method developed in the ensuing sections most closely resembles the panel-particle method of Willis et al. [Wil06, WPW07]. The resulting tool will enable efficient simulation and testing of aero- and hydrodynamic estimation and control strategies.

4.1 Coordinate Systems

A point in space $\mathbf{r}_{PG}$ can be defined relative to a ground-fixed coordinate frame at any instant in time by the relation

$$\mathbf{r}_{PG} = \mathbf{r}_{BG} + \mathbf{r}_{PB} \tag{4.1}$$

where $\mathbf{r}_{BG}$ is the origin of the body-fixed frame relative to the ground-fixed frame and $\mathbf{r}_{PB}$ is the position of the point under consideration relative to the body-fixed frame. The velocity of the same point in the ground-fixed frame, $\mathbf{v}_{PG}$, is then

$$\mathbf{v}_{PG} = \mathbf{v}_{BG} + \mathbf{v}_{PB} + \boldsymbol{\Omega} \times \mathbf{r}_{PB} \tag{4.2}$$

where $\mathbf{v}_{BG}$ represents the translational velocity of the body-fixed frame with respect to the ground-fixed frame, $\boldsymbol{\Omega}$ denotes the angular velocity of the body origin, and $\mathbf{v}_{PB}$ signifies the velocity of the point of interest with respect to the body-fixed origin due to deformations (e.g. control surface deflections, flapping kinematics, or elastic deformations).

4.2 The Mathematical Problem

In a real fluid, the relative motion between the body and fluid leads to the generation of vorticity in the thin region near the body surface known as the boundary layer. This shed vorticity convects away from the body to form the wake. To model this process, we consider the case where all the vorticity is confined to an infinitesimally thin vortex sheet. All flow regions outside of the sheet regions are considered to be irrotational. In using this sheet representation for the regions of vorticity, we must distinguish between two classifications of vortex sheets: (1) bound vortex sheets, and (2) free vortex sheets. The distinction is made because a bound sheet allows for the existence of a finite pressure jump across it, making it suitable for modeling the body. On the other hand, since a free vortex sheet must remain force free and moves with the local flow velocity, it is useful in representing the vorticity shed into the wake. The transition of vorticity from the bound sheet to the free sheet of the wake is reconciled via the so-called "unsteady Kutta condition" discussed in Section 2.6. This condition requires the flow to be free of singularities (i.e. to be finite everywhere). We note that the assumptions of the problems we are interested in studying lend themselves to the vortex sheet models considered here. That is to say, for high Reynolds number flows, the boundary layer and regions of shed vorticity may be viewed as infinitesimally thin regions of confined vorticity. As such, the accuracy of the model is expected to improve for larger Reynolds numbers.

In the current development, we restrict our attention to high Reynolds number flows of incompressible fluids. Again, these assumptions are suitable for the aerodynamic applications we are interested in studying. Let $\mathbf{u}(\mathbf{r}, t)$ denote the absolute velocity of a fluid particle at some point $\mathbf{r}$ of the flowfield at time t, $p(\mathbf{r}, t)$ the fluid pressure at that point, and ρ the constant fluid density. Under the assumption of large Reynolds number, the Navier-Stokes equations reduce to the Euler equations outside the regions of vorticity (i.e. away from the boundary layer and wake regions):

$$\frac{\partial \mathbf{u}}{\partial t} + (\mathbf{u} \cdot \nabla)\mathbf{u} = \frac{-1}{\rho} \nabla p. \tag{4.3}$$

This is accompanied by the continuity equation for incompressible flow,

$$\nabla \cdot \mathbf{u} = 0. \tag{4.4}$$

In this formulation, we have assumed that all body forces are conservative and that their potentials have been absorbed into the pressure term.

We must now impose appropriate boundary conditions for these equations. For this task, we shall assume that the locations of the boundary surfaces are known, and the normal component of the fluid velocity is prescribed along the boundaries. We denote the entire set of boundary surfaces by S. We note that for exterior problems, such as the aircraft formation flight studies of Chapter 6, there will be two sets of boundary conditions to impose on the flow field, one of which must be satisfied along S and another to be imposed far from S. Since we are dealing with the Euler limit of fluid flow, only one condition can be imposed along S. The constraint most consistent with this limit is that of no flow penetration across the boundaries, thus requiring the normal component of relative velocity between fluid and body to be zero

$$(\mathbf{u} - \mathbf{u}_S) \cdot \hat{\mathbf{n}} = 0 \text{ on } S \tag{4.5}$$

where $\mathbf{u}_S$ is the velocity of the boundary surface S, and $\hat{\mathbf{n}}$ is the unit surface normal vector. For our purposes, we ignore any transpiration velocities related to inlet/exit flows, such as those of engines; however, such conditions can be handled by modifying the boundary conditions along these surfaces such that

$$(\mathbf{u} - \mathbf{u}_S) \cdot \hat{\mathbf{n}} = \mathbf{u}_T \cdot \hat{\mathbf{n}}. \tag{4.6}$$

We now make note of an important point, namely that the above equations *do not* define a potential flow, which would only be the case if the flow were completely irrotational. Here the flow is not irrotational everywhere, only everywhere outside the regions to which vorticity is confined. Instead of taking the usual approach, as in the case of potential flows, of expressing the irrotational velocity field $\mathbf{u}(\mathbf{r}, t)$ as a gradient of a potential function from the onset, we express it as the sum of two velocities instead

$$\mathbf{u} = \mathbf{U}_\infty + \mathbf{U}. \tag{4.7}$$

The vector field $\mathbf{U}_\infty$ is the velocity of the onset flow, which is defined as the velocity field that would exist if no boundaries were present. The vector field $\mathbf{U}$ is then the disturbance velocity field attributed to the presence of boundaries. In general, this disturbance field may be decomposed into its irrotational and rotational parts (i.e. through a Helmholtz decomposition, as discussed in Section 2.2.1)

$$\mathbf{U}(\mathbf{r}, t) = \mathbf{U}_\phi(\mathbf{r}, t) + \mathbf{U}_\psi(\mathbf{r}, t) = \nabla\phi + \nabla \times \boldsymbol{\psi} \tag{4.8}$$

where the scalar potential represents the irrotational components of the disturbance field and the vector potential represents the rotational component due to the presence of vorticity. Upon applying the continuity equation for incompressible flow, we have

$$\begin{aligned}
\nabla \cdot \mathbf{U} = 0 &= \nabla \cdot (\mathbf{U}_\infty + \mathbf{U}_\phi + \mathbf{U}_\psi) \\
&= \nabla \cdot \mathbf{U}_\infty + \nabla \cdot \mathbf{U}_\phi + \nabla \cdot \mathbf{U}_\psi \\
&= \nabla \cdot \nabla\psi + \nabla \cdot (\nabla \times \boldsymbol{\psi}) \\
&= \nabla^2\phi.
\end{aligned}$$

Thus, the velocity potential $\phi(\mathbf{r}, t)$ satisfies Laplace's equation

$$\nabla^2\phi = 0. \tag{4.9}$$

At the body surface, the no flow penetration boundary condition (4.5) must be satisfied, or in the case of an inlet or outlet the transpiration boundary condition (4.6) must be enforced.

The regularity condition at infinity, that the disturbance field associated with the body vanish at infinity, is identically satisfied by invoking the Biot-Savart law to compute the associated velocity field (c.f. Section 2.2.2).

We make note of the fact that in determining the velocity field, we have only made use of the continuity equation. The Euler equations have not yet been invoked, demonstrating that the velocity can be determined independent of the pressure, as is the case in any incompressible flow. As such, once the velocity field has been determined, pressures can be computed by integrating the Euler equations. Another characteristic of incompressible flow that is consistent with the mathematical description above is that the influence of the boundaries is immediately felt across the entire domain; thus, the instantaneous velocity field is obtained from the instantaneous boundary conditions.

In addition to the boundary conditions considered above, the Kelvin-Helmholtz theorems (Section 2.4) and the unsteady Kutta condition (Section 2.6) are used to determine the strength and position of the free vortex sheets (i.e. the wakes), thus closing the solution strategy.

4.3 Discretization of Vortex Sheets

Traditional unsteady vortex panel methods represent both the bound vortex sheet of the body and the free vortex sheet of the wake by means of vortex panels. The present panel-particle method follows the approach taken in [Wil06, WPW07] by making use of vortex panels only in representing bound vortex sheets. Vortex particles are used to represent the free sheet of the wake instead. The present method differs from [Wil06, WPW07] in that the bound vortex panels are further discretized into equivalent vortex particle representations (c.f. Section 4.3.1) for improved computational efficiency during velocity computations by means of the fast multipole method (FMM). Describing all vortex elements by means of a single class of vortex entity prevents the need to call the FMM procedure multiple times due the existence of multiple integration kernels, thus saving time in FMM setup and associated overhead costs.

The bound vortex sheet is discretized into quadrilateral vortex panels consisting of four straight vortex line segments of uniform strength, $\Gamma_{i,j}(t)$. The use of quadrilateral panels automatically adheres to Kelvin's Circulation Theorem (Section 2.4) because the circulation of a closed-circuit pierced by the loop is zero. The placement of the vortex panels is dictated by Pistolesi's Theorem, originally formulated in 1933, which states that the correct circulation for a flat plate in two-dimensions results when a discrete vortex is concentrated at the quarter-chord point and the no-flow-penetration condition is satisfied at the three-quarter-chord point [Pis37]. Thus, the leading edge of each vortex panel is placed along the quarter-chord line of the geometric panel, while its trailing edge is placed along the quarter-chord line of the geometric panel behind it (c.f. Figure 4.1). The trailing edges of the row of trailing edge panels must be identified and given special treatment (Section 4.4) because they are responsible for transferring vorticity from the bound vortex sheet to the wake. The discretization of the body into a collection of vortex panels yields unknowns in the panel strengths, $\Gamma_{i,j}$. Since the conservation of circulation is already satisfied by the choice of

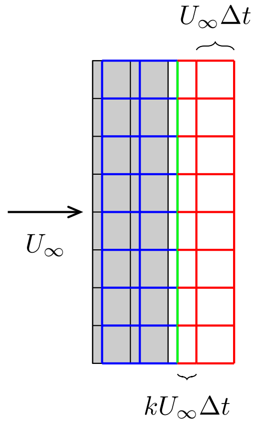

Figure 4.1: The bound vortex sheet — and the free vortex sheet — are represented by sets of quadrilateral vortex panels in traditional unsteady vortex panel methods. The trailing edge — represents the line about which vorticity is transferred from the bound vortex sheet into the free wake.

quadrilateral vortex panels, the no-flow-penetration boundary condition is all that remains for determining the panel strengths at each time step. Due to the discretization procedure, this boundary condition can only be satisfied at a finite number of control points, known as “collocation points.” The collocation points are chosen to coincide with the centroids of the four nodes of each panel, thus providing the most realistic downwash computation according to Pistolesi’s Theorem. The unit normal for each panel is then computed as the cross-product of the two diagonals of each panel. These two quantities, along with knowledge of the flow induced at the collocation point, leads to a linear system of equations for the panel strengths. Upon solving the panel strengths, the computational procedure for the given time-step is essentially complete.

4.3.1 Vortex Particle Representation of Line Vortex Segments

The main novelty of the specific panel-particle method developed here concerns the representation of vortex panels by means of vortex particles. This is a useful consideration because it reduces all of the vortex entities in the domain into vortex particles, thus making fast multipole method (FMM) invocations as seamless and computationally efficient as possible. By achieving a pure vortex particle representation of all of the vorticity in the domain, the overhead costs associated with establishing the FMM tree structures for multiple classes of vortex entities can be avoided. This streamlines the FMM implementation and leads to improved computational efficiency. In this section, we derive the equivalent vortex particle representation of a vortex segment. Since each panel consists of four segments, this is the only discretization that must be examined.

Consider a finite length line vortex which extends from point $\mathbf{a}$ to point $\mathbf{b}$ with constant strength Γ. The strength of this vortex segment can be written as an integral in the form

$$\Gamma = \int_a^b \gamma(\mathbf{s}) \mathrm{d}\mathbf{s}. \tag{4.10}$$

This integral representation lends itself to a simple “discretization” based on a quadrature method. Any quadrature method will suffice, but we will look to the Gauss-Lobatto quadrature method. We first consider the one-dimensional case, then extend our result to three-dimensions later. Thus, we begin with

$$\Gamma = \int_a^b \gamma(x)\mathrm{d}x \approx \frac{b-a}{2}\sum_{i=1}^{N} \tilde{w}_i \gamma\left(\frac{b-a}{2}\tilde{x}_i + \frac{a+b}{2}\right) \tag{4.11}$$

where $\tilde{x}_i$ and $\tilde{w}_i$ are the quadrature evaluation points and weightings, respectively. Since we are considering a line vortex with constant strength Γ, we apply the following uniform strength distribution inside the integral

$$\gamma(x) = \gamma = \frac{\Gamma}{b-a}. \tag{4.12}$$

Upon substitution, we obtain

$$\Gamma \approx \frac{b-a}{2}\sum_{i=1}^{N} \tilde{w}_i \frac{\Gamma}{b-a} = \frac{\Gamma}{2}\sum_{i-1}^{N} \tilde{w}_i. \tag{4.13}$$

Extending this one-dimensional quadrature in all three directions, yields,

$$\begin{aligned} \mathbf{x}_p &= \frac{\mathbf{b}-\mathbf{a}}{2}\tilde{x}_p + \frac{\mathbf{a}+\mathbf{b}}{2} && (4.14)\\ \boldsymbol{\alpha}_p &= \frac{\Gamma\tilde{w}_p}{2}\frac{\mathbf{b}-\mathbf{a}}{|\mathbf{b}-\mathbf{a}|} && (4.15) \end{aligned}$$

where $\mathbf{x}_p$ and $\boldsymbol{\alpha}_p$ denote the position and strength of vortex particle p, respectively.

4.4 Unsteady Trailing Edge Kutta Condition

In the case of bodies with sharp edges, the Kutta condition can be imposed to remove the non-uniqueness associated with the Euler equations [Saf92]. This condition, as discussed in Section 2.6, requires the velocity to be bounded, but not necessarily continuous. If we relax the condition of self-induced motion of the sheet in the immediate vicinity of the wing such that it is negligible, the sheet strength in the immediate vicinity of the wing must satisfy the equation

$$\frac{\partial \Gamma}{\partial t} + \mathbf{u}\frac{\partial \Gamma}{\partial s} = 0 \tag{4.16}$$

where $\Gamma(s,t)$ is the vortex sheet strength and s is the distance from the trailing edge. Such a consideration allows an approximation to the unsteady Kutta condition by means of a wake buffer region [Saf92]. To see this more clearly, consider (4.30) while setting the pressure jump to zero to enforce the condition that the wake must be a free vortex sheet (i.e. it must be force-free). Rewriting this condition in terms of a total derivative along the trailing edge yields

$$\left(\frac{\mathrm{d}\Gamma_{Wing}}{\mathrm{d}t}\right)_{\text{T.E.}} = -\left(\frac{\mathrm{d}\Gamma_{Wake}}{\mathrm{d}t}\right)_{\text{T.E.}} \tag{4.17}$$

This is the same approach taken in traditional unsteady panel methods (i.e. with panel representations of the wake). As noted by Katz and Plotkin in [KP01], experience dictates that the buffer wake panel should be aligned with the local flow field and its length should be prescribed to be between $k \approx 0.3 - 0.5$ for the most accurate force computations, where $0 \leq s \leq k$.

At each time-step, after the strength of the body-panels are computed, the strengths of the wake buffer panels are set equal to the strength of their wing-fixed counterparts. The trailing edge segments of the buffer wake region in the implementation of the panel-particle method hold their positions in space and are not convected with the flow until the very end of the time step. This approach is taken to ensure compliance with the unsteady Kutta condition throughout an entire time-step. Willis et al. arrive at the same Kutta condition in their work, though they claim this condition is a “linearized” condition on the zero pressure jump condition used to guarantee a force-free wake. [Wil06, WPW07]. This is clear when considering the first order approximation to the unsteady Kutta condition as presented in equation (4.35). Willis et al. caution that this first-order condition is only valid for moderately unsteady flows and that a non-linear pressure jump condition must be satisfied simultaneously with the no flow penetration condition if one considers highly unsteady flows. Such unsteadiness is beyond the scope of problems to be considered in the present work and will not be developed. The interested reader should consult Willis [Wil06] and Willis et al. [WPW07] for further discussion on this topic.

4.5 Wake Modeling

The wake vorticity is represented by means of vortex particles. As shown in [WCD05], the vorticity in the domain can be described as a linear superposition of all the vortex particles in the domain,

$$\begin{aligned} \boldsymbol{\omega}(\mathbf{x}, t) &= \sum_p \boldsymbol{\omega}_p(t) V_p \delta(\mathbf{x} - \mathbf{x}_p(t)) && (4.18) \\ &= \sum_p \boldsymbol{\alpha}_p(t) \delta(\mathbf{x} - \mathbf{x}_p(t)) && (4.19) \end{aligned}$$

where $\boldsymbol{\alpha} := \int_{V_p} \boldsymbol{\omega}(t) \mathrm{d}V = \boldsymbol{\omega}_p(t) V_p$ and V_p denotes the fluid volume described by the vortex particle situated at $\mathbf{x}_p$. The particle positions $\mathbf{x}_p(t)$ and strengths $\boldsymbol{\alpha}_p(t)$ are evolved according to

$$\begin{aligned} \frac{\mathrm{d}\mathbf{x}_p}{\mathrm{d}t} &= \mathbf{u}_p && (4.20) \\ \frac{\mathrm{d}\boldsymbol{\alpha}_p}{\mathrm{d}t} &= \nabla \mathbf{u}_p \cdot \boldsymbol{\alpha}_p && (4.21) \end{aligned}$$

Computation of $\mathbf{u}_p$ and $\nabla \mathbf{u}_p$ can be facilitated by direct invocation of the Biot-Savart law (recall equation 2.10). The present implementation, makes use of a fast multipole method (FMM) to expedite the computational process. Using the FMM solver reduces the cost of computation to $O(N \log N)$ from $O(N^2)$ associated with direct computations [GR88]. The vortex particles used in the wake description make use of regularization kernels to smooth out the singularity associated with these computations. Further details of regularized vortex particle methods can be found in [WCD05].

Results presented in the following sections make use of a forward Euler time-integration scheme,

$$\begin{aligned} \mathbf{x}_p^{k+1} &= \mathbf{x}_p^k + \mathbf{u}_p^k \Delta t && (4.22) \\ \boldsymbol{\alpha}_p^{k+1} &= \boldsymbol{\alpha}_p^k + \nabla \mathbf{u}_p^k \cdot \boldsymbol{\alpha}_p^k \Delta t. && (4.23) \end{aligned}$$

Higher order Runge-Kutta schemes can be incorporated to provide higher time resolution in the wake dynamics and may also be beneficial in instances leading to numerical instability for lower-order time-marching.

4.6 Aerodynamic Loads

The previous sections have described the procedure for determining the strength of the bound vorticity, the transfer for bound vorticity into free vorticity, and the evolution of the free vorticity in the wake. What remains is to determine the aerodynamic loads associated with the given distribution of vorticity in the domain. Here, attention is given to deriving an expression for computing the loads in a vortex panel method. Since the derivation is typically excluded from most texts and papers on vortex panel methods, it is included here for convenience to the curious reader.

We begin from the expression for the pressure jump across a bound vortex sheet, namely (2.35),

$$-[p] = \rho\left(\frac{\partial\Gamma}{\partial t} - \hat{\mathbf{n}}\cdot(\boldsymbol{\gamma}\times\overline{\mathbf{u}})\right). \tag{4.24}$$

We invoke the identity for scalar triple products,

$$\mathbf{a}\cdot(\mathbf{b}\times\mathbf{c}) = \mathbf{b}\cdot(\mathbf{c}\times\mathbf{a}) = \mathbf{c}\cdot(\mathbf{a}\times\mathbf{b}) \tag{4.25}$$

to obtain

$$-[p] = \rho\left(\frac{\partial\Gamma}{\partial t} - \overline{\mathbf{u}}\cdot(\hat{\mathbf{n}}\times\boldsymbol{\gamma})\right). \tag{4.26}$$

Upon substituting (2.31), $\boldsymbol{\gamma} = \hat{\mathbf{n}}\times\nabla\Gamma$, we have,

$$-[p] = \rho\left(\frac{\partial\Gamma}{\partial t} - \overline{\mathbf{u}}\cdot(\hat{\mathbf{n}}\times\hat{\mathbf{n}}\times\nabla\Gamma)\right). \tag{4.27}$$

Now we apply the vector triple product identity,

$$\mathbf{a}\times\mathbf{b}\times\mathbf{c} = \mathbf{b}(\mathbf{a}\cdot\mathbf{c}) - \mathbf{c}(\mathbf{a}\cdot\mathbf{b}) \tag{4.28}$$

to obtain

$$-[p] = \rho\left(\frac{\partial\Gamma}{\partial t} - \overline{\mathbf{u}}\cdot[\hat{\mathbf{n}}(\hat{\mathbf{n}}\cdot\nabla\Gamma) - \nabla\Gamma(\hat{\mathbf{n}}\cdot\hat{\mathbf{n}})]\right). \tag{4.29}$$

Noting that $\overline{\mathbf{u}}\cdot\hat{\mathbf{n}} = 0$ and $\hat{\mathbf{n}}\cdot\hat{\mathbf{n}} = 1$ yields,

$$-[p] = \rho\left(\frac{\partial\Gamma}{\partial t} + \overline{\mathbf{u}}\cdot\nabla\Gamma\right) \tag{4.30}$$

which is the analytical expression for the pressure jump across the bound vortex sheet in terms of Γ and $\overline{\mathbf{u}}$.

To apply this formula to our panel method, we expand further,

$$-[p] = \rho\left(\frac{\partial \Gamma}{\partial t} + \overline{u}_1\frac{\partial \Gamma}{\partial x_1} + \overline{u}_2\frac{\partial \Gamma}{\partial x_2} + \overline{u}_3\frac{\partial \Gamma}{\partial x_3}\right). \tag{4.31}$$

Taking $\hat{\mathbf{e}}_1 = \hat{\boldsymbol{\tau}}_1$, $\hat{\mathbf{e}}_2 = \hat{\boldsymbol{\tau}}_2$, and $\hat{\mathbf{e}}_3 = \hat{\mathbf{n}}$, then we have $\partial\Gamma/\partial x_1 = \partial\Gamma/\partial x$, $\partial\Gamma/\partial x_2 = \partial\Gamma/\partial y$, and $\partial\Gamma/\partial x_3 = 0$. Finally, we approximate the spatial derivatives as

$$\frac{\partial \Gamma_{i,j}}{\partial x} \approx \frac{\Gamma_{i,j} - \Gamma_{i-1,j}}{\Delta c_{i,j}} \tag{4.32}$$

$$\frac{\partial \Gamma_{i,j}}{\partial y} \approx \frac{\Gamma_{i,j} - \Gamma_{j-1,j}}{\Delta b_{i,j}} \tag{4.33}$$

and the time derivative as

$$\frac{\partial \Gamma^{(k)}}{\partial t} \approx \frac{\Gamma^{(k)} - \Gamma^{(k-1)}}{\Delta t^{(k)}}. \tag{4.34}$$

This yields the numerical discretization for 4.30 which can be applied in a panel method,

$$-\Delta p_{i,j} = p^- - p^+ = \frac{\Gamma^{(k)}_{i,j} - \Gamma^{(k-1)}_{i,j}}{\Delta t^{(k)}} + (\overline{\mathbf{u}}\cdot\hat{\tau}_1)^{(k)}_{i,j}\left(\frac{\Gamma_{i,j} - \Gamma_{i-1,j}}{\Delta c_{i,j}}\right)^{(k)} + (\overline{\mathbf{u}}\cdot\hat{\tau}_2)^{(k)}_{i.j}\left(\frac{\Gamma_{i,j} - \Gamma_{i,j-1}}{\Delta b_{i,j}}\right)^{(k)}. \tag{4.35}$$

This final expression is equivalent to the one reported in [KP01], though their discussion spares the details of the derivation.

Integrating the surface pressures associated with each panel into a force vector normal to that panel enables computation of the resultant force vector on the body. In turn, this can be decomposed into components of lift and drag in the standard manner.

4.7 Code Validation

Two preliminary validation simulations are presented. The first is of an impulsively started flat plate, used to demonstrate the correctness of the force computations. The second study is identical to the first, except that a two flat plate formation is considered. It demonstrates the ability of the numerical scheme to handle multiple bodies and wakes, while exhibiting the method's ability to capture unsteady aerodynamic effects such as wake encounters.

4.7.1 Simulation Specifications

The unsteady lift and drag forces on a flat plate, impulsively started from rest, are computed by means of the panel-particle method described above. Various aspect ratios were simulated and the results are compared against those from a purely panel-based solver presented in [KP01]. The panel-particle simulation makes use of 56-panels (4-chordwise and 14-spanwise) for each wing with each panel segment represented by its equivalent 8-vortex-particle description. Each flat plate's angle of attack is prescribed as $\alpha = 5^o$. The time-stepping increment Δt and velocity magnitude $|\mathbf{U}_\infty|$ were chosen such that $\frac{U_\infty \Delta t}{c} = \frac{1}{16}$.

4.7.2 Impulsive Start of a Flat Plate

The rolled-up wake of an $AR = 4$ flat plate is visualized by means of instantaneous vortex particle positions in Figure 4.2. Both the starting vortex and the rolled-up tip vortices are clear from this visualization. The resulting lift and drag time-histories compare to those predicted by Katz and Plotkin [KP01] quite well (Figures 4.3–4.5). Although the induced drag has a faster time-response in the current method, the steady state-values are very close to those presented in [KP01].

4.7.3 Impulsive Start of a Two Flat Plate Formation

To demonstrate the panel-particle method's capability in handling multiple bodies and unsteady wake encounters, a two plate formation of $AR = 4$ flat plates is simulated from start-up. The simulation is equivalent to the one of the single flat plate, except for the presence of a second flat plate. This second plate is situated two wingspans aft and one quarter of a wingpsan below the leader.

The lift and drag histories clearly capture the transient effect of the lead plate's wake on the trailing plate (c.f. Figure 4.7). As the starting vortex of the leader passes over the trailing plate, the lift and drag curves both drop. Then as the starting vortex moves away, the drag curve recovers to its initial steady-state value while the lift curve continues to converge to a

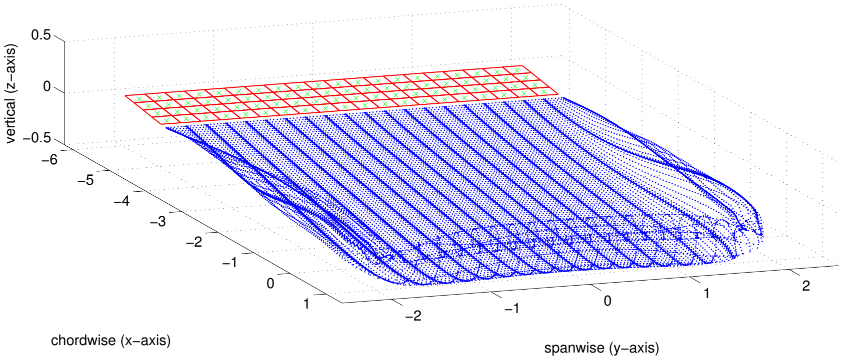

Figure 4.2: Snapshot of impulsively translating $AR = 4$ flat plate at $\alpha = 5^o$ with its associated vortex particle wake. The figure depicts geometric panels —, collocation points ×, vortex particles in the wake •.

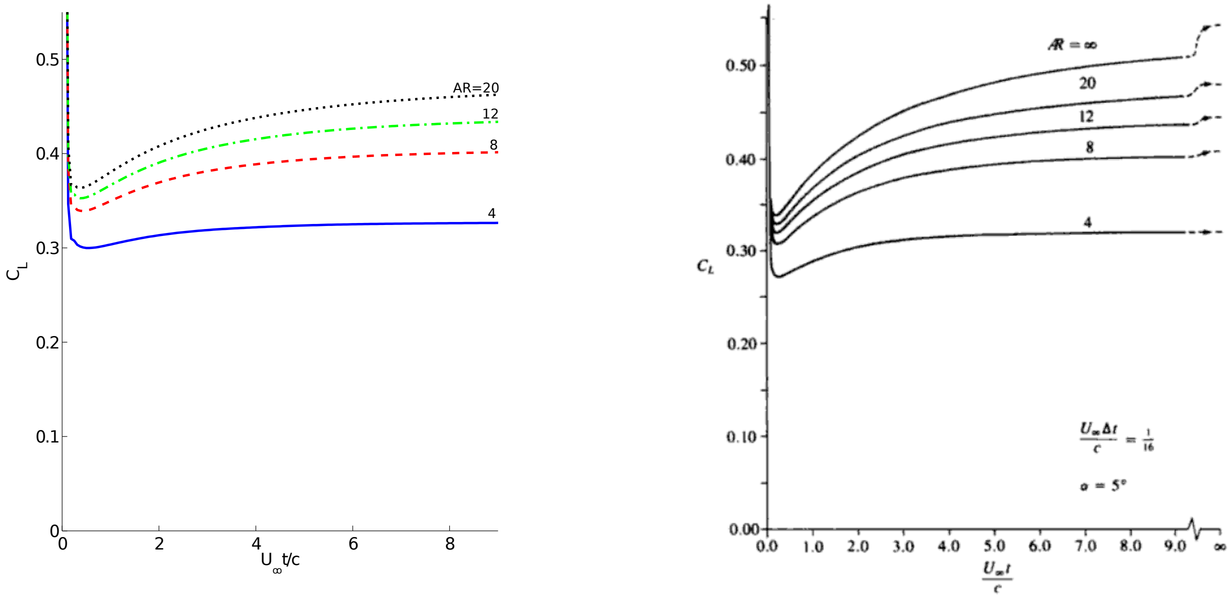

(a) Panel-Particle Transient Lift Curve

(b) Transient Lift Curve from [KP01]

Figure 4.3: Transient lift curves for wings of various aspect ratio generated by the present panel-particle method compared with the results report in [KP01].

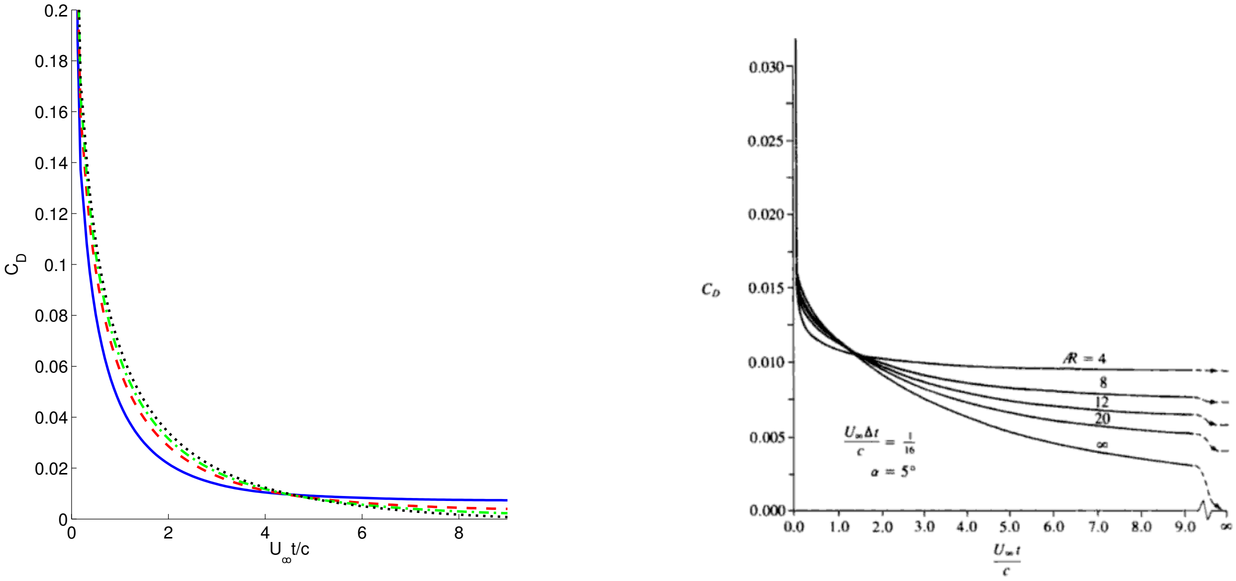

(a) Panel-Particle Transient Induced Drag Curve

(b) Transient Induced Drag Curve from [KP01]

Figure 4.4: Transient induced drag curves for wings of various aspect ratio generated by the present panel-particle method compared with the results report in [KP01]. The drag curves in (a) correspond to $AR = 4$ (—), 8 (– –), 12 (– · –), and 20 (· · ·).

reduced steady-state value. The lead plate's lift and drag curves are identical to those of the isolated case. This is expected since the trailing plate's wake has little influence from two wingspans back, as does the leader's own wake deformations resulting from interactions with the follower's wake. The wake visualization in Figure 4.6 is taken from a snapshot of vortex particle positions approximately half-way through the simulation so as to provide a clear image of the two rolled-up wakes. Until the point at which the lead plate's wake passes over the trailing plate, both wakes are essentially identical to one another. At this instant, the wake encounter causes a dip in drag and an initial rise in lift. Ultimately, the drag recovers to approximately its initial value, though the lift is greatly compromised. The results of this analysis demonstrate a need for reliable estimates of the wake location for formation flight missions. Being in the wake does not guarantee a drag benefit, and can potentially yield undesirable effects such as drag increase or, as seen here, lift degradation.

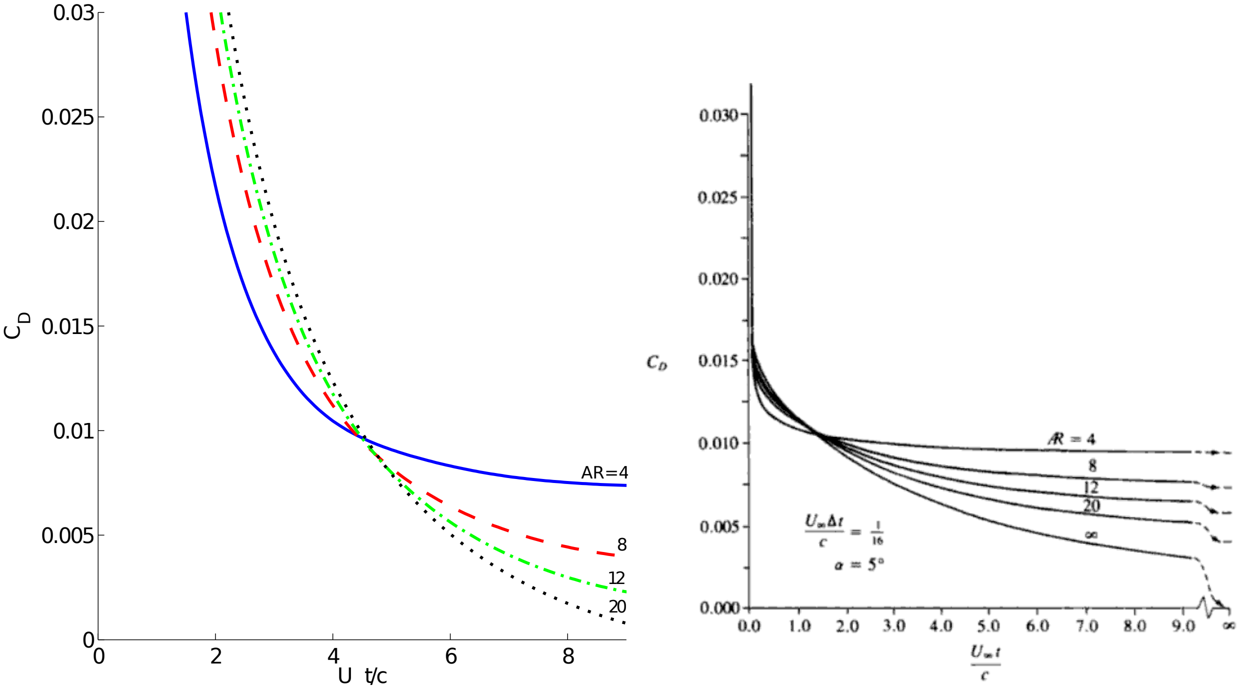

(a) Panel-Particle Induced Drag Curve (Zoomed-In)

(b) Induced Drag Curve from [KP01]

Figure 4.5: A closeup of the transient induced drag curves for wings of various aspect ratio generated by the present panel-particle method compared with the results report in [KP01].

4.8 Conclusions

The vortex panel-particle implementation in this chapter relied upon a pure vortex particle representation for both the free and bound vorticity, thus yielding a more efficient computational scheme. By relying solely on vortex particles, the overhead time associated with setting up the FMM algorithm for multiple vortex entities is greatly reduced. The particle representation of the wake, though not a new concept, is a useful means of capturing the wake evolution in unsteady multi-body aerodynamics problems. The capabilities of the method for the impulsive startup of a single wing and a two-wing formation were demonstrated in Section 4.7. The force histories associated with the single wing case matched other results in the literature quite closely. Resulting force histories for the two-wing formation clearly indicate the method's ability to capture transients in the forces due to wake encounters from multiple bodies. Ultimately, the availability of an efficient unsteady multi-body aerodynamic

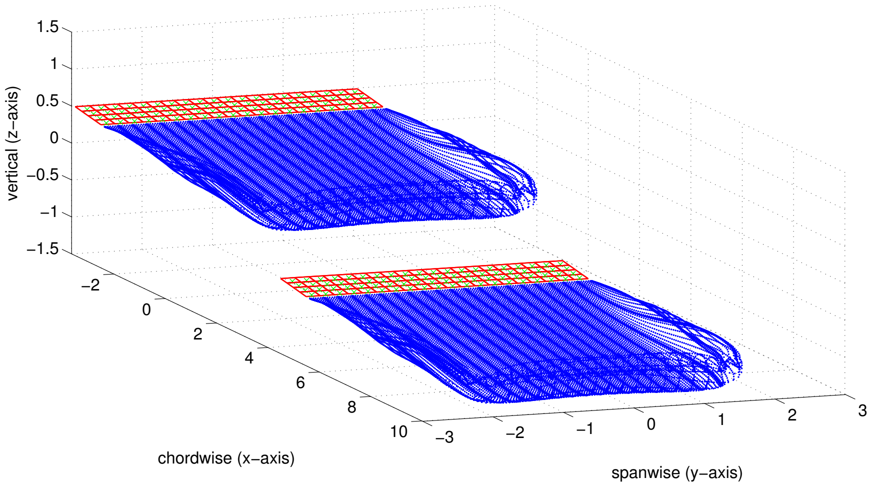

Figure 4.6: Snapshot of two impulsively translating $AR = 4$ flat plates at $\alpha = 5^{o}$ with their associated vortex particle wakes. The figure depicts geometric panels —, collocation points ×, vortex particles in the wake •.

tool will prove useful in the simulation, testing, and validation of flow estimation and control algorithms. Testing controllers and estimators in an unsteady environment enables the designer to validate algorithms for robustness qualities that will be essential to real-world functionality.

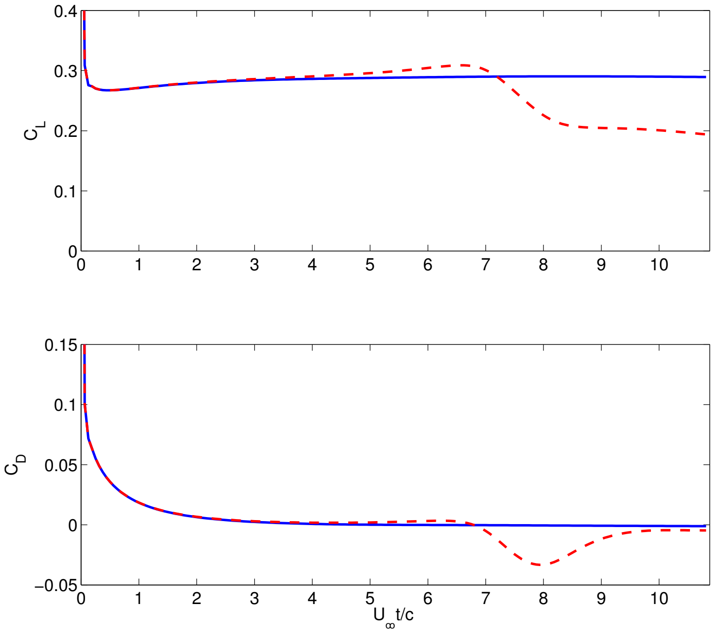

Figure 4.7: Transient lift and induced drag curves generated by the present panel-particle method for two $AR = 4$ wings flying in the specified leader-follower formation. Forces associated with the leader are drawn as solid lines —, while those corresponding to the follower are drawn as dashed lines – –.

CHAPTER 5

Nonlinear Estimation and Filtering

By definition, feedback control systems require the use of state feedback; however, in many instances the desired states are unmeasurable and not directly available for feedback. Such states are deemed inaccessible and motivate the use of a state estimator for reconstructing the desired states from available measurements. Optimal estimation, according to Gelb, consists of a computational algorithm for processing measurements to "deduce a minimum error estimate of the state of a system by utilizing: knowledge of the system and measurement dynamics, assumed statistics of system noises and measurement errors, and initial condition information," [Gel74]. Since the states of interest, from a control standpoint, are typically inaccessible for most fluid mechanical systems, a state estimator is almost assuredly required for any closed-loop flow control application. In the present treatise, focus is given to vortex-based methods for estimating the states of aero- and hydrodynamic systems. This is done by augmenting nonlinear stochastic estimation and filtering algorithms with vortex models to synthesize sensor measurements and deduce information about the state of the flow.

The general notion of filtering and estimation theory was first considered by Gauss in 1809 in *Theoria Motus*. The following passage, analyzed thoroughly by Sorenson [Sor70], demonstrates the parallels between Gauss' original notion of least-squares estimation with modern day filtering and estimation theory.

> If the astronomical observations and other quantities, on which the computation of orbits is based, were absolutely correct, the elements also, whether deduced from three or four observations, would be strictly accurate (so far indeed as the motion is supposed to take place exactly according to the laws of KEPLER [*sic*])

> and, therefore, if other observations were used, they might be confirmed, but not corrected. But since all our measurements and observations are nothing more than approximations to the truth, the same must be true of all calculations resting upon them, and the highest aim of all computations made concerning concrete phenomena must be to approximate, as nearly as practicable, to the truth. But this can be accomplished in no other way than by suitable combination of more observations than the number absolutely requisite for the determination of the unknown quantities. This problem can only be properly undertaken when an approximate knowledge of the orbit has already been attained, which is afterwards to be corrected so as to satisfy all the observations in the most accurate manner possible.
>
> —C.F. Gauss in *Theoria Motus* translation taken from pp. 249 in [Dav57]

The statement by Gauss is incredibly insightful, especially given the time in which it was made. "In fact, it can be argued that the Kalman filter is, in essence, a recursive solution to Gauss' original least-squares problem," [Gel74]. Sorenson's paper [Sor70] should be consulted for a full treatment of historical developments leading up to Kalman's seminal paper which introduced the linear Gaussian-noise optimal filter (i.e. the Kalman filter) in 1960.

We now establish the general framework of nonlinear estimation problems. Consider the system Σ, comprised of an N-dimensional nonlinear discrete-time state equation and an M-dimensional nonlinear discrete-time measurement equation, given by

$$\Sigma \begin{cases} \mathbf{x}_{k+1} = \mathbf{f}_k(\mathbf{x}_k) + G_k(\mathbf{x}_k)\mathbf{w}_k \\ \mathbf{z}_k = \mathbf{h}_k(\mathbf{x}_k) + \mathbf{v}_k \end{cases} \tag{5.1}$$

where $\mathbf{w}_k$ and $\mathbf{v}_k$ are independent noise processes representing process noise and measurement noise, respectively. We also allow for a weighting of the process noise as a function of the state through the scaling matrix $G_k(\mathbf{x}_k)$ The goal of any estimation algorithm is to determine the system state $\mathbf{x}_k$ at time-step k from the set of all available measurements $\mathbf{z}_{1:k} = \{\mathbf{z}_i, i = 1, \ldots, k\}$.

There are numerous techniques for treating this general problem. Variations exist due to the assumptions and derivation methodologies invoked by researchers. As alluded to by Gauss, all of these methods attempt to accomplish their goals by synthesizing all available measurements and assimilating them in some manner with a model in an effort to improve the estimate of a given state. The present discussion will focus on the specific estimation algorithms considered during the current studies on vortex-based estimation and is in no way a complete survey of this mature field. Presentation of the Kalman filtering paradigm and variations of it will be introduced first. The final section discusses the perspectives of Bayesian estimation and particle filtering, which have gained much attention in recent years due to advances in computational speed and parallel architectures for real-time systems. The focus will tend toward the practical, while derivations and proofs of the algorithms can be found in the literature referenced in each of the ensuing sections.

5.1 Kalman Filtering

The problem of nonlinear filtering involves the estimation of the state of a dynamical system from a sequence of noisy measurements. Work in this field began to attract great attention ever since Kalman's publication [Kal60] of the linear optimal filter in 1960 and has been the focus of many studies by the statistical and engineering communities ever since. In the following sections, a brief introduction to the Kalman filter and its many variations is presented. The block diagram in Figure 5.1 describes the general framework of the Kalman filter and should be kept in mind while reading the following sections.

5.1.1 Linear Kalman Filtering

The Kalman filter, introduced by Rudolph E. Kalman in 1960, provides an optimal solution to the Gaussian-noise linear filtering problem. That is, if the noise sequences $\mathbf{w}_k \sim \mathcal{N}(0, W_k)$ and $\mathbf{v}_k \sim \mathcal{N}(0, V_k)$ in Σ are assumed independent processes, and if both $\mathbf{f}(\cdot)$ and $\mathbf{h}(\cdot)$ are linear, the Kalman filter represents the minimum mean-square error and minimum variance

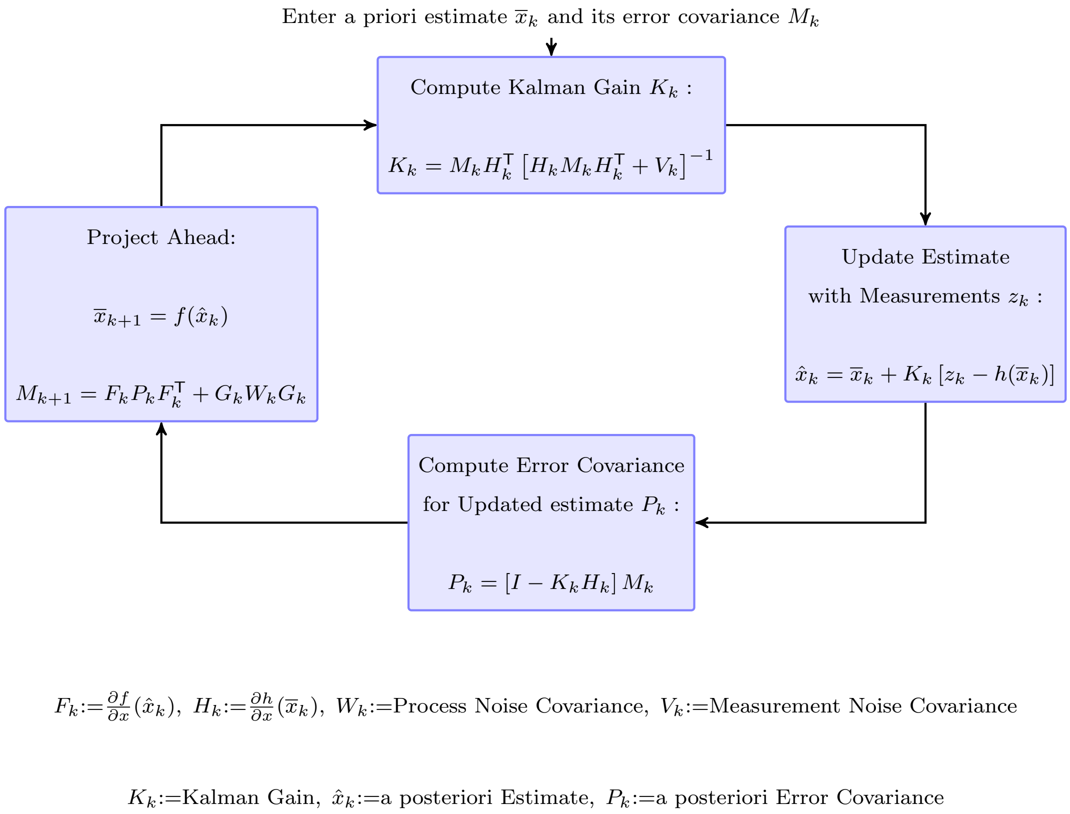

Figure 5.1: The Kalman filter block diagram graphically represents the framework by which recursions of the Kalman filter and its variations operate.

estimator. Moreover, the algorithm can be expressed as a recursion, so only knowledge of the current measurement and the last estimate is required. As such, the Kalman filter has become the algorithm of choice in dealing with general estimation problems.

For convenience we rewrite $\mathbf{f}_k(\mathbf{x}_k) = F_k \mathbf{x}_k$ and $\mathbf{h}_k(\mathbf{x}_k) = H_k \mathbf{x}_k$, since they are assumed linear. This takes us from Σ in (5.1) to Σ_1 defined as

$$\Sigma_1 \left\{ \begin{aligned} \mathbf{x}_{k+1} &= F_k \mathbf{x}_k + G_k \mathbf{w}_k \\ \mathbf{z}_k &= H_k \mathbf{x}_k + \mathbf{v}_k \end{aligned} \right. . \tag{5.2}$$

As will be seen in the following sections, by manipulating the system Σ to conform to the assumptions required by the Kalman filter, a vast array of problems can be handled by the algorithm. The algorithm below applies to the linear system Σ_1.

$$
\begin{aligned}
\bar{\mathbf{x}}_{k+1} &= F_k \hat{\mathbf{x}}_k, && (5.3)\\
M_{k+1} &= F_k P_k F_k^{\mathsf{T}} + G_k W_k G_k^{\mathsf{T}}, && (5.4)\\
K_k &= P_k H_k^{\mathsf{T}} V_k^{-1}, && (5.5)\\
\hat{\mathbf{x}}_k &= \bar{\mathbf{x}}_k + K_k[\mathbf{z}_k - \mathbf{h}(\bar{\mathbf{x}}_k)], && (5.6)\\
P_k &= [M_k^{-1} + H_k^{\mathsf{T}} V_k^{-1} H_k]^{-1} && (5.7)
\end{aligned}
$$

where

- $\bar{\mathbf{x}}_{k+1} \in \mathbb{R}^n$ is the updated *a priori* state estimate,
- $M_{k+1} \in \mathbb{R}^{n\times n}$ is the updated a *priori estimation* covariance,
- $K_k \in \mathbb{R}^{n\times m}$ is the Kalman Gain,
- $\hat{\mathbf{x}}_k \in \mathbb{R}^n$ is the current *a posteriori* state estimate, and
- $P_k \in \mathbb{R}^{n\times n}$ is the current *a posteriori* estimation covariance.

It is important to note that equivalent forms exist that are more tractable for specific classes of problems. Here, the algorithm specified proves to be the best suited for vortex-based estimation.

5.1.2 Extended Kalman Filtering

The notion of the extended Kalman filter (EKF) considered here was first considered by Stanley Schmidt in an effort to apply the Kalman filtering algorithm to nonlinear spacecraft navigation problems [BD67]. Consider the system Σ, again with independent Gaussian noise sequences $\mathbf{w}_k$ and $\mathbf{v}_k$, but now with nonlinear functions $\mathbf{f}_k(\cdot)$ and $\mathbf{h}_k(\cdot)$. If these functions are "sufficiently" smooth, they can be expanded via Taylor series about the conditional mean (i.e. the most current estimate). Retaining only up to the first-order terms yields the linear system

$$\Sigma_2 \begin{cases} \mathbf{x}_{k+1} = F_k \mathbf{x}_k + G_k \mathbf{w}_k \\ \mathbf{z}_k = H_k \mathbf{x}_k + \mathbf{v}_k \end{cases} \tag{5.8}$$

where

$$F_k := \left(\frac{\partial \mathbf{f}}{\partial \mathbf{x}}\right)_{\mathbf{x}=\hat{\mathbf{x}}_k} \quad \text{and} \quad H_k := \left(\frac{\partial \mathbf{h}}{\partial \mathbf{x}}\right)_{\mathbf{x}=\overline{\mathbf{x}}_k} \tag{5.9}$$

The Kalman filter recursion for this approximate model is identical to the linear Kalman filter recursion, though it is referred to as the "extended Kalman filtering recursion" to denote the linearization process applied to handle the model nonlinearities. The act of linearization results in a filter which is no longer linear nor optimal. Additionally, the conditional means and covariances are now mere approximations, as the filter does not propagate statistics through the model nonlinearities directly. The EKF recursion is simply

$$\bar{\mathbf{x}}_{k+1} = F_k \hat{\mathbf{x}}_k, \tag{5.10}$$

$$M_{k+1} = F_k P_k F_k^{\mathsf{T}} + G_k W_k G_k^{\mathsf{T}}, \tag{5.11}$$

$$K_k = P_k H_k^{\mathsf{T}} V_k^{-1}, \tag{5.12}$$

$$\hat{\mathbf{x}}_k = \bar{\mathbf{x}}_k + K_k[\mathbf{z}_k - \mathbf{h}(\bar{\mathbf{x}}_k)], \tag{5.13}$$

$$P_k = [M_k^{-1} + H_k^{\mathsf{T}} V_k^{-1} H_k]^{-1} \tag{5.14}$$

where

- $\bar{\mathbf{x}}_{k+1} \in \mathbb{R}^n$ is the updated *a priori* state estimate,
- $M_{k+1} \in \mathbb{R}^{n\times n}$ is the updated *a priori* estimation covariance,
- $K_k \in \mathbb{R}^{n\times m}$ is the Kalman Gain,
- $\hat{\mathbf{x}}_k \in \mathbb{R}^n$ is the current *a posteriori* state estimate, and
- $P_k \in \mathbb{R}^{n\times n}$ is the current *a posteriori* estimation covariance.

It is emphasized that the original nonlinear $\mathbf{h}(\overline{\mathbf{x}}_k)$ is used in equation (5.13) within the EKF recursion.

5.1.3 Variations of Extended Kalman Filtering

When the functions $\mathbf{f}_k(\cdot)$ and $\mathbf{h}_k(\cdot)$ are not sufficiently smooth, local iterations can be applied or higher-order approximations can be made. The remaining two sections discuss these approaches for dealing with insufficiently smooth nonlinear systems.

5.1.3.1 Iterated Extended Kalman Filtering

The iterated extended Kalman filter (IEKF) is presented in [Jaz07], [Gel74], and many other texts. The algorithm follows the EKF algorithm with the *a posteriori* update equation (i.e. equation 5.13) replaced by the iterator:

$$\begin{aligned}
\boldsymbol{\eta}_{i+1} &= \overline{\mathbf{x}}_k + K(\boldsymbol{\eta}_i)\left[\mathbf{z}_k - \mathbf{h}(\boldsymbol{\eta}_i) - M(\boldsymbol{\eta}_i)\{\overline{\mathbf{x}}_k - \boldsymbol{\eta}_i\}\right] \quad \text{for} \quad i = 1, \ldots, p && (5.15)\\
\hat{\mathbf{x}}_k &= \boldsymbol{\eta}_p && (5.16)
\end{aligned}$$

The iteration begins with $\boldsymbol{\eta}_1 = \overline{\mathbf{x}}_k$ and terminates when $||\boldsymbol{\eta}_{i+1} - \boldsymbol{\eta}_i|| \leq \epsilon$, for small ϵ, or when the maximum number of iterations is reached. The covariance matrix is then computed based on the linearization about $\boldsymbol{\eta}_p$.

The iterated EKF presented above is suitable for handling nonlinearities associated with the measurements, but does not improve issues related to nonlinear system dynamics. An iterated EKF can be designed to deal with nonlinear state equations as well, though the topic will not be developed here. Discussion of such an approach can be found in [Jaz07].

5.1.3.2 Higher Order Extended Kalman Filtering

As previously noted, there are many variations to the extended Kalman filter, distinguished from each other by varying assumptions and derivation techniques. Here, we present the case where more terms from the Taylor expansions of $\mathbf{f}_k(\cdot)$ and $\mathbf{h}_k(\cdot)$ are retained. Specifically, we consider the second-order extended Kalman filter (SOEKF). We note that many derivations of this algorithm exist, but that many of the derivations, including the one by Jazwinski in [Jaz07], are erroneous as shown by Henriksen in [Hen82]. As such, we present Henriksen's algorithm and direct the reader to [Hen82] for further details and explanations.

Given the dynamical system Σ in (5.1), the SOEKF recursion proceeds as follows

$$
\begin{aligned}
\bar{\mathbf{x}}_{k+1} &= \mathbf{f} + \frac{1}{2}\mathbf{f}_{xx}\mathrm{cs}(P_k) && (5.17)\\
M_{k+1} &= \mathbf{f}_x P_k \mathbf{f}_x^\mathsf{T} + G_x\left[P_k \otimes W_k\right]G_x^\mathsf{T} + \frac{1}{2}G_{xx}\left[\mathrm{cs}(P_k)\otimes W_k\right]G^\mathsf{T} \\
&\quad + \frac{1}{2}G\left[\mathrm{cs}(P_k)\otimes W_k\right]^\mathsf{T} G_{xx}^\mathsf{T}, && (5.18)\\
K_k &= M_k \mathbf{h}_x^\mathsf{T}\left[\mathbf{h}_x M_k \mathbf{h}_x^\mathsf{T} + V_k\right]^{-1}, && (5.19)\\
\hat{\mathbf{x}}_k &= \bar{\mathbf{x}}_k + K_k[\mathbf{z}_k - \hat{\mathbf{z}}_k], && (5.20)\\
P_k &= (I - K_k\mathbf{h}_x)M_k && (5.21)
\end{aligned}
$$

where $\mathbf{f} := \mathbf{f}_k(\hat{\mathbf{x}}_k)$, $\mathbf{h} := \mathbf{h}_k(\hat{\mathbf{x}}_k)$, $\hat{\mathbf{z}}_k := \mathbf{h}_k(\hat{\mathbf{x}}_k) + \frac{1}{2}\mathbf{h}_{xx}\mathrm{cs}(M_k)$, $A \otimes B$ denotes the Kronecker product of matrices A and B, $\mathrm{cs}(A)$ denotes the column string of the matrix A, $\mathbf{y}_x$ denotes the Jacobian of $\mathbf{y}$ with respect to $\mathbf{x}$, and $\mathbf{y}_{xx}$ denotes the Hessian matrix of $\mathbf{y}$ with respect to $\mathbf{x}$.

5.2 Bayesian Estimation

The goal of a Bayesian estimator is to approximate the conditional probability distribution function (pdf) of $\mathbf{x}_k$ based on measurements $\mathbf{z}_{1:k} = \{\mathbf{z}_1, \mathbf{z}_2, \ldots, \mathbf{z}_k\}$, denoted as $p(\mathbf{x}_k|\mathbf{z}_{1:k})$. The first measurement is obtained at $k = 1$, so the initial condition of the estimator is the pdf of $\mathbf{x}_o$, which simplifies to $p(\mathbf{x}_o|\mathbf{z}_o) = p(\mathbf{x}_o)$, since $\mathbf{z}_o$ is defined as the set of no measurements. Once we compute $p(\mathbf{x}_k|\mathbf{z}_{1:k})$, we can estimate the current state $\mathbf{x}_k$ from the conditional pdf in any manner we deem most appropriate based on the given problem. The present discussion closely follows the development in [Gri03].

Our goal is to find a recursion for computing $p(\mathbf{x}_k|\mathbf{z}_{1:k})$ given:

1. The *a priori* distribution, $p(\mathbf{x}_o)$,

2. The dynamical system equations (5.1), and

3. The measurement sequence $\mathbf{z}_{1:k} = \{\mathbf{z}_1, \ldots, \mathbf{z}_k\}$.

To do so, we assume a Markovian dynamical system model $p(\mathbf{x}_{k+1}|\mathbf{x}_k)$, that is:

1. Given the present, the future is independent of the past:

$$p(\mathbf{x}_{k+1}|\mathbf{x}_{1:k}, \mathbf{z}_{1:k}) = p(\mathbf{x}_{k+1}|\mathbf{x}_k) \tag{5.22}$$

2. Given the present, the past is independent of the future:

$$p(\mathbf{x}_{k-1}|\mathbf{x}_{k:T}, \mathbf{z}_{k:T}) = p(\mathbf{x}_{k-1}|\mathbf{x}_k). \tag{5.23}$$

Additionally, we assume the measurements $\mathbf{z}_k$ are conditionally independent given $\mathbf{x}_k$, such that

$$p(\mathbf{z}_k|\mathbf{x}_{1:k}, \mathbf{z}_{1:k}) = p(\mathbf{z}_k|\mathbf{x}_k). \tag{5.24}$$

Provided the above assumptions are satisfied, knowledge of the *a posteriori* distribution from the previous time-step, $p(\mathbf{x}_{k-1}|\mathbf{z}_{1:k-1})$, allows us to compute the joint distribution of $\mathbf{x}_k, \mathbf{x}_{k-1}$ given $\mathbf{z}_{1:k-1}$ as

$$\begin{aligned} p(\mathbf{x}_k, \mathbf{x}_{k-1}|\mathbf{z}_{1:k}) &= p(\mathbf{x}_k|\mathbf{x}_{k-1}, \mathbf{z}_{1:k-1})p(\mathbf{x}_{k-1}|\mathbf{z}_{k-1}) && (5.25)\\ &= p(\mathbf{x}_k|\mathbf{x}_{k-1})p(\mathbf{x}_{k-1}|\mathbf{z}_{k-1}). && (5.26) \end{aligned}$$

Integrating over $\mathbf{x}_{k-1}$ yields the Chapman-Kolmogorov equation

$$p(\mathbf{x}_k|\mathbf{z}_{1:k-1}) = \int p(\mathbf{x}_k|\mathbf{x}_{k-1})p(\mathbf{x}_{k-1}|\mathbf{z}_{1:k-1})\mathrm{d}\mathbf{x}_{k-1}. \tag{5.27}$$

This represents Bayes' prediction step for our optimal filter and provides us with an expression for the *a priori* distribution.

To compute the *a posteriori* distribution, we invoke Bayes' rule

$$\begin{aligned} p(\mathbf{x}_k|\mathbf{z}_{1:k}) &= \frac{1}{\zeta_k}p(\mathbf{z}_k|\mathbf{x}_k, \mathbf{z}_{1:k-1})p(\mathbf{x}_k|\mathbf{z}_{1:k-1}) && (5.28)\\ &= \frac{1}{\zeta_k}p(\mathbf{z}_k|\mathbf{x}_k)p(\mathbf{x}_k|\mathbf{z}_{1:k-1}) && (5.29) \end{aligned}$$

where $\zeta_k := p(\mathbf{z}_k|\mathbf{z}_{1:k-1}) = \int p(\mathbf{z}_k|\mathbf{x}_k)p(\mathbf{x}_k|\mathbf{z}_{1:k-1})\mathrm{d}\mathbf{x}_k$ is a normalization constant ensuring (5.29) remains a probability distribution. This final equation represents Bayes' update step, and together with the prediction step (5.27), completes the Bayesian optimal filter.

In this form, Bayes' filter is an exact solution to the estimation problem and can be used on *any* Markov system. In most practical instances, the above integrations must be carried out over a high-dimensional state-space, making exact solutions impractical. As a result, many approximation strategies have arisen. In the next section, we consider the *particle filtering* approximation technique for Bayesian estimation.

5.2.1 Particle Filtering

Particle filters approximate the Bayesian optimal filtering equations by means of Monte Carlo methods. The *a posteriori* density is represented by a set of random samples, or "particles," with associated weights. As the number of particles increases, the representation approaches the exact functional description of the probability distribution.

Let $\{\mathbf{x}_k^i, w_k^i\}_{i=1}^{N_p}$ denote a set of support points $\{\mathbf{x}_k^i, i = 1, \dots, N_p\}$ and their associated weights $\{w_k^i, i = 1, \dots, N_p\}$ characterizing the *a posteriori* density $p(\mathbf{x}_k|\mathbf{z}_{1:k})$. Then, the *a posteriori* density at time k can be approximated as

$$p(\mathbf{x}_k|\mathbf{z}_k) \approx \sum_{i=1}^{N_p} w_k^i \delta(\mathbf{x}_k - \mathbf{x}_k^i). \tag{5.30}$$

The individual particle weights are determined by means of "importance sampling," as described in [AMG02, Gri03, RAG04]. That is, we assume that $p(\mathbf{x}) \propto \pi(\mathbf{x})$ is difficult to draw samples from, but that $\pi(\mathbf{x})$ can be evaluated with ease. Thus, $p(\mathbf{x})$ can also be computed to within a proportionality with relative ease. We also consider $\mathbf{x}^p \sim q(\mathbf{x})$ to be particles drawn from the proposal density $q(\cdot)$, known as the "importance density." Thus, we may write the weighted approximation of $p(\mathbf{x})$ as

$$p(\mathbf{x}) \approx \sum_{i=1}^{N_p} w^i \delta(\mathbf{x} - \mathbf{x}^i) \tag{5.31}$$

where

$$w^i \propto \frac{\pi(\mathbf{x}^i)}{q(\mathbf{x}^i)} \tag{5.32}$$

is the normalization weight of the i^{th} particle. Thus, the weights in (5.30) can be defined in a similar manner if the samples $\{\mathbf{x}_k^i\}$ are drawn from a proposal density $q(\mathbf{x}_k|\mathbf{z}_k)$, as

$$w_k^i \propto \frac{p(\mathbf{x}_k^i|\mathbf{z}_k)}{q(\mathbf{x}_k^i|\mathbf{z}_k)}. \tag{5.33}$$

At each iteration, we have knowledge of the set of particles approximating $p(\mathbf{x}_{k-1}^i|\mathbf{z}_{k-1})$ and wish to approximate the current *a posteriori* distribution $p(\mathbf{x}_k^i|\mathbf{z}_k)$ by a set of new samples. By selecting the importance density such that it can be factorized as

$$q(\mathbf{x}_k|\mathbf{z}_k) = q(\mathbf{x}|\mathbf{x}_{k-1}, \mathbf{z})q(\mathbf{x}_{k-1}|\mathbf{z}_{k-1}), \tag{5.34}$$

we can draw samples from $q(\mathbf{x}_k^i|\mathbf{z}_k)$ to determine the new set of samples $\{\mathbf{x}_k^i\}$. Additionally, we note the following factorizations

$$\begin{aligned} p(\mathbf{x}_k|\mathbf{z}_k) &= \frac{p(\mathbf{z}_k|\mathbf{x}_k, \mathbf{z}_{k-1})p(\mathbf{x}_k|\mathbf{z}_{k-1})}{p(\mathbf{z}_k|\mathbf{z}_{k-1})} && (5.35)\\ &= \frac{p(\mathbf{z}_k|\mathbf{x}_k, \mathbf{z}_{k-1})p(\mathbf{x}_k|\mathbf{x}_{k-1}, \mathbf{z}_{k-1})}{p(\mathbf{z}_k|\mathbf{z}_{k-1})}p(\mathbf{x}_{k-1}|\mathbf{z}_{k-1}) && (5.36)\\ &= \frac{p(\mathbf{z}_k|\mathbf{x}_k)p(\mathbf{x}_k|\mathbf{x}_{k-1})}{p(\mathbf{z}_k|\mathbf{z}_{k-1})}p(\mathbf{x}_{k-1}|\mathbf{z}_{k-1}) && (5.37)\\ &\propto p(\mathbf{z}_k|\mathbf{x}_k)p(\mathbf{x}_k|\mathbf{x}_{k-1})p(\mathbf{x}_{k-1}|\mathbf{z}_{k-1}). && (5.38) \end{aligned}$$

Then, upon substituting (5.34) and (5.38) into (5.33) we obtain the weight update equation

$$w_k^i \propto \frac{p(\mathbf{z}_k|\mathbf{x}_k^i)p(\mathbf{x}_k^i|\mathbf{x}_{k-1}^i)}{q(\mathbf{x}_k^i|\mathbf{x}_{k-1}^i, \mathbf{z}_k)}w_{k-1}^i, \tag{5.39}$$

which can be used to compute the approximate *a posteriori* density $p(\mathbf{x}_k|\mathbf{z}_k)$ at each time-step via (5.30). A wide variety of numerical algorithms have been developed based on the presentation above. No one algorithm is better than the rest, as the various implementations tend to have varying performance under different circumstances. The following section gives a presentation of the specific algorithm used for the present studies of vortex-based state estimation. Details and developments concerning other varieties of particle filters can be found in [AMG02, BTG02, Gri03, RAG04].

5.2.1.1 Particle Filtering Algorithm

The block diagram of Figure 5.2 depicts the general particle filtering algorithm steps in graphical form. The specific PF implementation used in this study assumes the probability distribution functions are all Gaussian. This leads to the specific analytical forms presented in the equations below. The PF recursion is given as

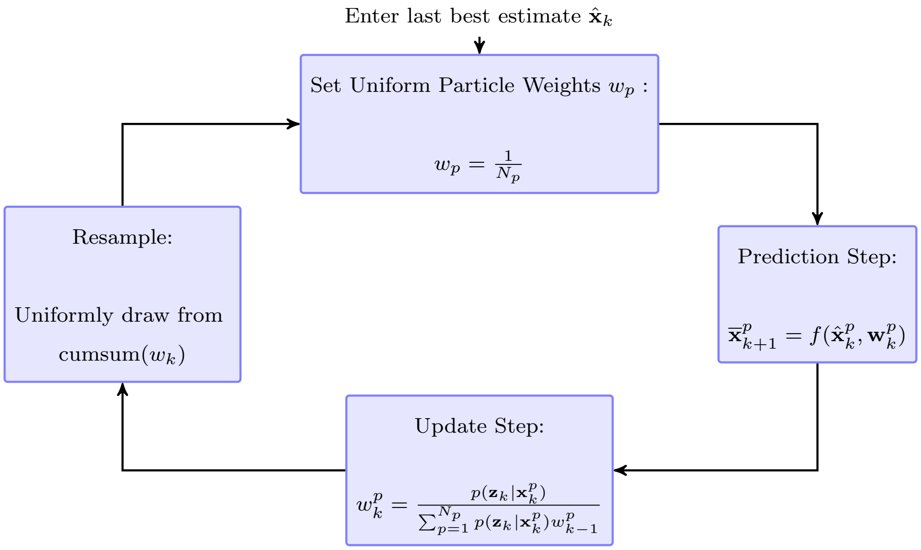

p:=Particle Index=1,...,N_p, w_k:=Vector of Particle Weights w_k^p, cumsum:=Cumulative Sum of Vector Elements.

Figure 5.2: The particle filter block diagram graphically represents the general steps involved in the PF algorithm.

$$\bar{\mathbf{x}}_{k+1}^p = \mathbf{f}_k(\mathbf{x}_k^p, \mathbf{w}_k^p) \tag{5.40}$$

$$\Psi_k^p = -\frac{1}{2}\left[\mathbf{z}_k - \mathbf{h}_k(\mathbf{x}_k^p)\right] V_k^{-1} \left[\mathbf{z}_k - \mathbf{h}_k(\mathbf{x}_k^p)\right] \tag{5.41}$$

$$w_k^p = \frac{\exp(\Psi_k^p)}{\sum_{p=1}^{N_p} \exp(\Psi_k^p)} \tag{5.42}$$

$$\hat{\mathbf{x}_k} = \sum_{p=1}^{N_p} w_k^p \mathbf{x}_k^p \tag{5.43}$$

$$P_k = \frac{1}{N-1} \sum_{p=1}^{N_p} w_k^p (\hat{\mathbf{x}}_k - \mathbf{x}_k^p)^2 \tag{5.44}$$

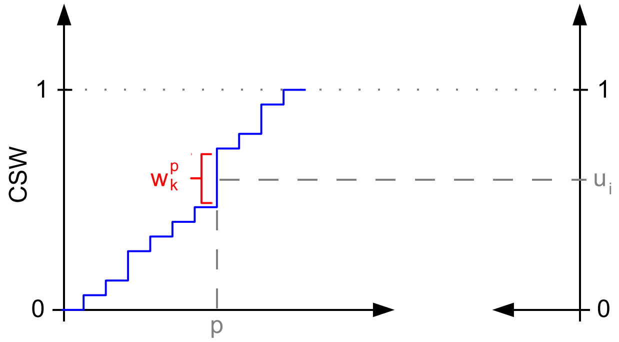

Figure 5.3: Resampling by the cumulative sum of particle weights (CSW) depends upon a mapping from CSW to the particle index p. By drawing from $\mathcal{U}[0, 1]$, the particles with the highest weights have the highest likelihood of being sampled for the next step.

As time progresses, the PF algorithm can lead to degeneracy due to the overweighting of a few particles, making the remaining particles useless. A common method of circumventing this issue comes in the form of a "resampling" step. Further discussion regarding various approaches to resampling can be found in [AMG02, RAG04]. Here, the resampling step is implemented via a simple cumulative sum algorithm. By taking the cumulative sum of the particle weights (CSW) we can map random draws from the uniform distribution $\mathcal{U}[0, 1]$ to the particle index p as shown in Figure 5.3. This mapping results in the particles $\mathbf{x}_k^p$ with the greatest weights w_k^p having the greatest likelihood of being selected. Particles with low weights will be dropped from the PF, being replaced by additional particles generated in the region of particles with the highest weights.

5.3 Bias and Divergence Issues

Regardless of the estimation algorithm employed, bias and divergence issues may result due to modeling errors and the system's observability characteristics.

5.3.1 Modeling Errors

Both bias and divergence may result due to mismatches between the estimator model and the true physics associated with the system [Jaz07, Lew86]. Such effects are a byproduct of the filter operating based on inaccurate knowledge. In other words, the filter is told that the process behaves one way, whereas in reality it behaves in a different way. As a result of an inaccurate measurement model, the filter will continue fitting the wrong model to the measurement data. Even if the residuals go to zero, the estimates will be biased due to the modeling errors.

5.3.2 Observability Problems

Unobservable states can lead to the problem of filter divergence [Jaz07, Lew86]. If the unobservable states are unstable, the corresponding estimation errors will also be unstable, thus leading to divergence. Unless additional measurements are unattainable due to physical or design restrictions, the best solution to such divergence issues lies in augmenting the filter with additional measurements which introduce observability to the otherwise hidden states.

CHAPTER 6

Wake Estimation for Formation Flight

Flying aircraft in formation can lead to significant fuel savings due to the reduction in induced drag realized by the trailing aircraft. This method of drag reduction is contingent upon having the trailing aircraft positioned properly within the upwash-field of the lead aircraft's wake. Proper positioning within this upwash-field yields a rotation of the resultant force vector (c.f. Figure 6.1), which is to first order responsible for the reduction in induced drag [BM98, RCV02]. The rotation of the resultant force vector is depicted in Figure 6.1. It is clear from the figure that the induced angle of attack due to the lead aircraft's upwash-field leads to a decrease in induced drag (i.e. ΔD points in the direction of motion) and a small increase in lift.

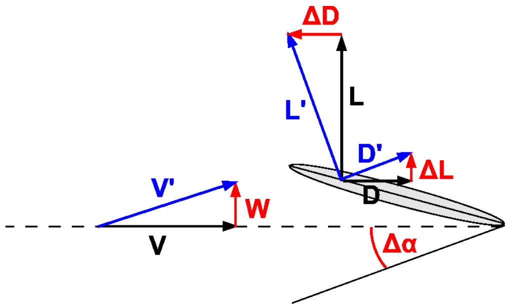

Figure 6.1: The upwash of the lead aircraft's wake leads to a rotation of the resultant force on the trailing aircraft. To first order, this rotation is responsible for the decrease in induced drag realized by flying in formation. The figure presents the baseline forces, induced effects, and formation forces.

It is important to note that 50% of the benefit is lost if the wake cannot be tracked to within 10% span [BM98]. Based on this sensitivity to position within the wake, it is clear that accurate estimates of the wake location are essential for successful drag reduction in formation flight missions. This problem of reliable wake sensing lends itself to a vortex-based aerodynamic estimation approach. By representing the wake as a pair of counter-rotating infinite line vortices, the vortex-based aerodynamic estimation paradigm can be applied directly. In the present chapter, we develop a vortex-based wake estimator to address the issue of wake sensing by means of distributed on-board aerodynamic sensors.

We begin by reviewing background on formation flight research in Section 6.1. Details regarding the aerodynamic modeling are presented in Section 6.2, followed by analysis pertaining to wake observability based on various classes of aerodynamic measurements. In Section 6.4 we discuss specific details of the vortex-based wake estimation algorithms and outline the approach to integrating the aerodynamic models within the estimation framework. Performance results for various configurations and estimator implementations are presented in Section 6.5, while conclusions and discussion are presented in Section 6.6.

6.1 Introduction

Aircraft wake vortices and their contribution to induced drag comprise a broad body of technical literature and research. The review article by Spalart, and citations therein, summarize a tremendous amount of knowledge on aircraft trailing vortices, especially with regards to characterizing their formation, dynamics, and decay [Spa98]. Another review article, by Kroo, summarizes fundamental aspects of induced drag and various drag reduction concepts that take advantage of induced drag physics [Kro01]. Additionally, an excellent overview of wake vortex research involving transport aircraft can be found in the article by Rossow [Ros99].

The specific topic of formation flying aerodynamics has been examined from a variety of standpoints. For example, some investigators have considered the optimal downwash and lift distribution of formation flying wings [FG03], while others have focused on approaches for the modeling and simulation of aircraft formations [Mar03, WM03]. Many groups have attempted to better characterize, by way of wind-tunnel measurements, the effect of tip vortices and wake roll-up on the trailing aircraft [BSA06, BM08, Gin99, OG92, SJD03]. Numerous flight tests have also been conducted to determine real-world feasibility and proof-of-concept for formation flying missions. Among these are the tests conducted at NASA Dryden, in 2001, on F/A-18 aircraft [Ian02, RCV02, VRW02] as well as recent tests at Edwards Air Force Base, in 2010 and 2012, on a fleet of C-17 transport aircraft [Dri12, Thu10].

The issue of formation flight control has also been the focus of several investigations. Giulietti et al. have studied various aspects of formation flight dynamics and control [GIN05], while Campa et al. have considered the design and flight testing of non-linear formation control laws [CGS07]. There has also been much focus on real-time formation optimization by means of extremum-seeking control [BAK03, CSF05, CWS02, RS10]. All of these studies consider formation aerodynamic effects as a function of the relative position between aircraft. This is a reasonable assumption for longitudinal separations on the order of a few wingspans, but deteriorates as this separation increases. Due to safety restrictions imposed by regulating bodies, practical formation flight missions will require significant longitudinal separations. This poses a problem to strategies considered in these past studies because approaches based on relative aircraft positioning are not robust to atmospheric turbulence and wind gusts. This will most necessarily shift and modify wake characteristics in such a manner as to invalidate any such approach. Surely, constructing the aerodynamic benefit maps is more useful if they are referenced relative to the *wake* position directly. It is useful to note that these larger separation distances may be advantageous from a vortex-based wake estimation standpoint; the wake vortices will have more time to coalesce into coherent structures, thus giving them a closer semblance to the simple horseshoe models typically used to represent such flows.

The sensing and detection of wake vortices is not a new concept. Much research and technology development has focused on detecting wake hazards in the airspace and on airport runways. However, many such wake detection tools require access to heavy, expensive, and complex instrumentation, such as radar, lidar, massive microphone and sodar arrays, and specialized acoustic transducer configurations [BMH07, HYK02, RDJ07, Rub00, RLH03, SR10]. Despite significant advances made for wake hazard detection, these systems are primarily designed for ground use. The systems available for in-flight use, such as airborne lidar, remain impractical for operational use from both a cost and weight standpoint.

Other approaches for vortex detection have also been considered in non-aircraft scenarios. For example, much work has been conducted on Lagrangian data assimilation for vortex detection in the atmospheric and oceanic sciences community [IG97a, IG97b, KIJ03]. This work provides useful insight into general vortex detection, but remains outside the scope of on-board wake sensing due to the need for Lagrangian measurements, which are unavailable for operational formation flight missions. In 2003, Suzuki and Colonius developed a method for detecting a vortex in a channel [SC03]. This work is especially noteworthy due to its semblance to the approach taken in the present study, in that an array of pressure sensors is used to determine the vortex parameters of interest.

Despite all of the progress made in formation flight research, it is clear that, to date, reliable and practical methods for on-board wake estimation and sensing remain nonexistent. Knowledge of the wake location is essential to the success of formation flight missions for drag reduction. As Blake and Multhopp have shown, small deviations from the true wake location can lead to large losses in the drag benefit [BM98], thus indicating the absolute need for accurate and precise wake position estimates. The goal of wake sensing is to obtain reliable estimates of the wake location based on measurements taken from a suite of on-board sensors. The ultimate goal is to rely solely upon pre-existing instrumentation; however, such a solution may not be physically possible.

The present work makes significant contributions towards realizing a practical system for real-time on-board wake estimation. The current development makes use of wing-distributed pressure sensors to extract the lead aircraft's wake parameters. Since the wake's upwash-field is inherently distributed, the lead aircraft's wake leaves an aerodynamic signature across the trailing aircraft's lifting surfaces. By assimilating measurements from wing-distributed sensors, the wake signature can be used to back-out the wake location and other parameters of interest. The added advantage of such an approach is its ability to provide basic insights into the role of the fundamental wake nonlinearity associated with the upwash-field. The wake estimation algorithm developed here makes use of simple, but rich, aerodynamic models to reveal the fundamental aspects of the wake sensing problem. In doing so, it is found that nonlinearities inherent to the wake's influence on the trailing aircraft can lead to undesirable behaviors, under certain circumstances. It is shown, in the present study, that adopting more sophisticated nonlinear filtering paradigms and introducing relative motions between aircraft can help mitigate some of these issues. The present work marks the first time, to the authors' knowledge, that distributed aerodynamic measurements have been synthesized to successfully determine the wake parameters of a lead aircraft during formation flight.

6.2 Aerodynamic Modeling

In designing a reliable wake estimation strategy, a representation of the wake's influence on the trailing aircraft must be considered. This representation will rely upon a model for the lead aircraft and its wake as well as a model for the trailing aircraft's aerodynamic response due to the presence of this wake. It is essential that the ensuing model be of sufficiently low-order for use in real-time wake estimation. The following sections present the development of the low-dimensional vortex-based model to be integrated with the nonlinear filtering methods of Chapter 5.

6.2.1 Lead Aircraft and Wake Representation

The influence of the lead aircraft, both on its own wake and on the trailing aircraft, can be neglected due to the large longitudinal separations experienced between aircraft during formation flight missions. Indirectly, the geometry and weight of the lead aircraft will play a role on the aerodynamics because they dictate the characteristics of the resulting wake model. The simple horseshoe representation of an aircraft can be further simplified based on these assumptions, since the bound vortex no longer introduces a notable influence at large distances. As a result, only the semi-infinite legs of the horseshoe remain, representing the wake. Again, invoking the assumption of large longitudinal separations, these vortices can be represented as infinite line vortices. The remainder of this section develops the analytical expression for the upwash/downwash distribution due to this wake model.

To begin, we invoke (2.11), the expression for the velocity induced at the point $\mathbf{x}$ due to an infinite line vortex of strength Γ,

$$\mathbf{u}(\mathbf{x}) = \frac{-\Gamma}{4\pi} \int_{-\infty}^{\infty} \frac{[\mathbf{x} - \mathbf{x}(s)] \times \frac{\mathrm{d}\mathbf{x}}{\mathrm{d}\mathbf{s}}\,\mathrm{d}s}{|\mathbf{x} - \mathbf{x}(s)|^3}. \tag{6.1}$$

We make note that the velocity induced by a set of N infinite line vortices at the point $\mathbf{x}$ can be written as the linear superposition of (6.1),

$$\mathbf{u}(\mathbf{x}) = -\sum_{i=1}^{N} \frac{\Gamma_i}{4\pi} \int_{-\infty}^{\infty} \frac{[\mathbf{x} - \mathbf{x}_i(s)] \times \frac{\mathrm{d}\mathbf{x_i}}{\mathrm{d}s}\,\mathrm{d}s}{|\mathbf{x} - \mathbf{x}_i(s)|^3}. \tag{6.2}$$

For the remainder of the current discussion, we will consider the case of two straight infinite line vortices of equal and opposite strength, both of which run parallel to the wing's longitudinal axis. That is,

$$N = 2,$$

$$\Gamma_2 = -\Gamma_1,$$

$$\frac{\mathrm{d}x_1}{\mathrm{d}s} \mid\mid \frac{\mathrm{d}x_2}{\mathrm{d}s} \mid\mid \hat{\mathbf{e}}_x.$$

In such a case, we have the following expression for the vortex induced *upwash* (i.e. induced velocity projected in the body-fixed z-direction) at the point (y, z),

$$w_o(y; \Gamma_o, y_{o,1}, z_{o,1}, y_{o,1}, z_{o,2}) = \frac{\Gamma_o(y - y_{o,1})}{2\pi[z_{o,1}^2 + (y - y_{o,1})^2]} - \frac{\Gamma_o(y - y_{o,2})}{2\pi[z_{o,2}^2 + (y - y_{o,2})^2]} \tag{6.3}$$

where $(y_{o,1}, z_{o,1})$ and $(y_{o,2}, z_{o,2})$ denote the locations of the first and second vortex cores, respectively, and $\Gamma_o = \Gamma_2 = -\Gamma_1$.

Further, if we assume the two line vortices are coplanar with a plane running parallel to the ground (i.e. with zero roll angle), then we can write this expression as a function of the vortex separation distance b,

$$w_o(y; \Gamma_o, y_o, z_o, b) = \frac{\Gamma_o(y - y_o + \frac{b}{2})}{2\pi[z_o^2 + (y - y_o + \frac{b}{2})^2]} - \frac{\Gamma_o(y - y_o - \frac{b}{2})}{2\pi[z_o^2 + (y - y_o - \frac{b}{2})^2]}. \tag{6.4}$$

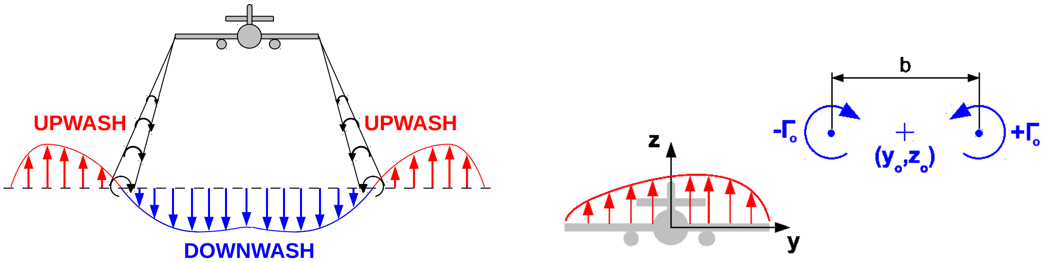

(a) Lead Aircraft Upwash-Field (b) Wake Vortex Coordinate System

Figure 6.2: (a) The upwash-field attributed to the lead aircraft is equivalent to that of a horseshoe vortex. (b) The wake vortex system is defined with respect to the center of the trailing aircraft. This wake leaves an aerodynamic signature, such as $\Delta C_p(y)$ or $\alpha(y)$, on the lifting surfaces of the trailing aircraft.

This nonlinear expression represents the wake's direct influence on the upwash-field and, as will be seen, is the fundamental nonlinearity associated with wake estimation.

6.2.2 Trailing Aircraft Representation

With the wake model established, it is now necessary to develop a mapping from the wake representation to an aircraft's aerodynamic response to it. The physics of the problem lends itself to a classical lifting line approach. Here, we develop the classical approach for a lifting surface flying in isolation, then augment the model to accommodate the presence of an upwash-field due to the presence of a nearby wake. Such a model provides the necessary mapping from the wake parameters to the associated aerodynamic response and does so while keeping the model dimensionality sufficiently small for use in real-time wake estimation.

Consider a finite wing represented as a bound vortex sheet connected to a wake represented as a free vortex sheet. We can represent these vortex sheets as a single spanwise distribution of horseshoe vortices of strength $\Gamma(y)$. The bound vortex sheet is then represented by the so-called "lifting-line" where the forces due to this horseshoe system are evaluated. This representation is equivalent to a vortex-lattice method that employs only a single chordwise panel, but an infinite set of spanwise panels. The trailing vortex system is then the semi-infinite plane behind the lifting-line defined by

$$x \geq c(y)_{1/4}, \ |y| \leq \frac{\tilde{b}}{2}, \text{ and } z = 0.$$

Though the theory of this model is not adequate for highly swept wings, it is expected to perform well for the problems of interest here. Geometric sophistication can later be introduced through invocations of so-called "extended" or "modern" lifting line methods. Such sophistication is not considered presently, as it is deemed more important to gain basic understanding in simple configurations prior to applying the scheme to more complex geometries.

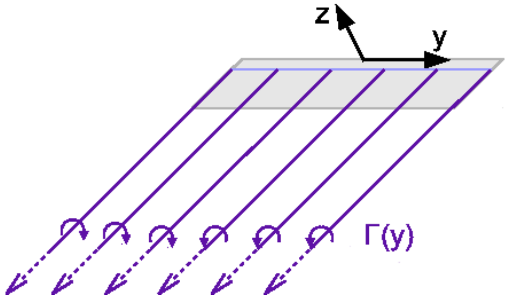

Figure 6.3: The lifting line vortex system provides a reasonable representation of lifting surfaces, and provides a basis by which to compute aerodynamic distributions and responses.

Invoking the Kutta-Joukowski theorem (as in the vortex-lattice method), the lift and induced drag per unit span, L' and D_i' respectively, can be computed. Assuming a small angle of attack α and a small downwash w, relative to U_∞, we have

$$\begin{aligned} L'(y) &\approx \rho U_\infty \Gamma(y) && (6.5) \\ D_i'(y) &\approx \rho w(y) \Gamma(y) \\ &\approx \rho U_\infty \Gamma(y) \alpha_i(y) && (6.6) \end{aligned}$$

where α_i is the induced angle of attack defined by

$$\alpha_i := \text{atan}(\frac{w}{U_\infty}) \approx \frac{w}{U_\infty}.$$

The main difference between lifting-line theory and the vortex-lattice method arises in the approach used in evaluating the strength distribution of the bound vortex sheet $\Gamma(y)$. The lifting-line approach assumes that two-dimensional lift-coefficients are valid at any spanwise location, whereas the vortex lattice method explicitly satisfies the no flow penetration condition at a finite set of collocation points distributed about the wing. Thus for the lifting line method we have,

$$C_l = m_o \left(\alpha - \alpha_{l=0} - \alpha_i\right), \tag{6.7}$$

where m_o and $\alpha_{l=0}$ are the two-dimensional lift-curve slope and zero-lift angle of attack, respectively. These parameters can be found a number of ways (e.g. theoretically, experimentally, or computationally). Additionally, the induced angle of attack α_i accounts for the reduction in the effective angle of attack due to finite wing effects, such as trailing vortices. Clearly, the assumption of locally two-dimensional flow at every spanwise station is a best approximation when the span is large relative to the mean chord; that is, for large aspect ratio wings,

$$AR := \frac{\tilde{b}^2}{S} >> 1.$$

Since,

$$C_l := \frac{L'}{\frac{1}{2}\rho U_\infty^2 c(y)}, \tag{6.8}$$

we can determine the load distribution $\Gamma(y)$ by substituting into (6.5),

$$\begin{aligned} \Gamma(y) = \frac{L'(y)}{\rho U_\infty} &= \frac{1}{2} C_l U_\infty c(y) \\ &= \frac{1}{2} m_o(y) U_\infty c(y) \left[\alpha - \alpha_{l=0}(y) - \alpha_i(y)\right]. \end{aligned} \tag{6.9}$$

Our calculation of α_i at the lifting-line is greatly simplified by the planar topology we assumed of the trailing vortex system. We can draw upon the result of an infinite two-dimensional vortex sheet, making note of the fact that the free vortex sheet here supplies only half that contribution (since it's modeled as a *semi*-infinite sheet). Thus, the downwash distribution on the lifting line is,

$$w(y) = \frac{-1}{4\pi} \oint_{-\tilde{b}/2}^{\tilde{b}/2} \frac{\gamma_x}{y - \eta} \mathrm{d}\eta. \tag{6.10}$$

We note that $\gamma_x = -\mathrm{d}\Gamma/\mathrm{d}y$, so we can write,

$$\alpha_i(y) \approx \frac{1}{4\pi U_\infty} \fint_{-\tilde{b}/2}^{\tilde{b}/2} \frac{\mathrm{d}\Gamma/\mathrm{d}\eta}{y-\eta}\mathrm{d}\eta. \tag{6.11}$$

Substituting this expression back into our original expression for $\Gamma(y)$ yields the following integro-differential equation for the strength distribution along the lifting line,

$$\Gamma(y) = \frac{1}{2}U_\infty c(y) m_o(y) \left[\alpha - \alpha_{l=0}(y) - \frac{1}{4\pi U_\infty} \fint_{-\tilde{b}/2}^{\tilde{b}/2} \frac{\mathrm{d}\Gamma/\mathrm{d}\eta}{y-\eta}\mathrm{d}\eta\right] \tag{6.12}$$

with the boundary conditions,

$$\Gamma(-\tilde{b}/2) = \Gamma(\tilde{b}/2) = 0 \tag{6.13}$$

to ensure no lift generation at the wing tips.

This expression is of course only valid for a single isolated wing undergoing steady trimmed flight. If we wish to consider quasi-steady maneuvers in the presence of line vortices, we must expand upon the expression above by introducing additional terms to the upwash distribution along the span. For example, any vertical translational velocity W_{AC} will introduce a uniformly distributed downwash along the span. Additionally, rolling maneuvers (i.e. rotations about the body-fixed x-axis) will induce a downwash proportional to the distance from the center of rotation $\Omega_x y$). Here we assume the center of rotation is located at mid-span of the wing (i.e. $y_{C.G.} = 0$). Finally, pitching maneuvers (i.e. rotations about the body-fixed y-axis) will introduce a downwash proportional to the difference in position between the wing's center of gravity and the quarter-chord as $\Omega_y(c_{1/4}(y) - x_{C.G.})$. For our purposes, we will assume $c_{1/4}(y) - x_{C.G.}$ is negligible, thus we will ignore this term. This assumption is also consistent with that of small sweep angles, which is inherent in the use of lifting-line theory in the first place. We finally include a term $w_o(y; \Gamma_o, y_o, z_o)$, which represents the upwash distribution associated with the presence of a finite set of line vortices to account for the presence of the wake.

The final form of our generalized lifting-line integro-differential equation becomes,

$$\Gamma(y) = K_L(y)\left[U_\infty\left[\alpha(y) - \alpha_{l=0}(y)\right] - W_{\mathrm{AC}} - \Omega_x y + w_o(y; \Gamma_o, y_o, z_o) - \frac{1}{4\pi}\int_{\tilde{b}/2}^{\tilde{b}/2} \frac{\mathrm{d}\Gamma/\mathrm{d}\eta}{y-\eta}\mathrm{d}\eta\right] \tag{6.14}$$

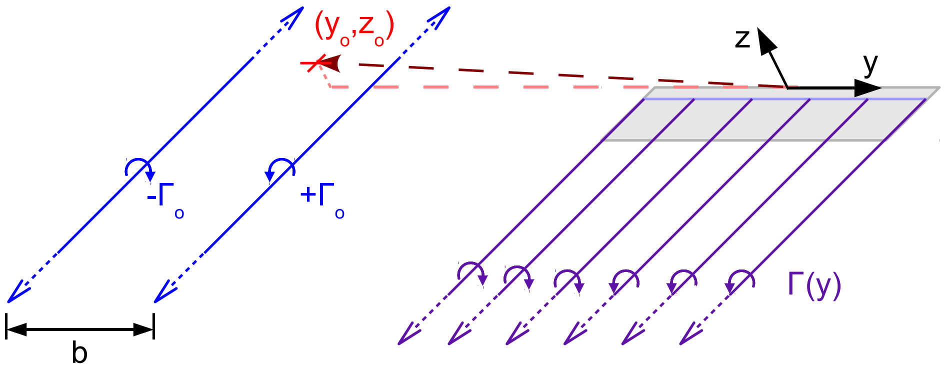

Figure 6.4: The augmented lifting line model is constructed via the standard lifting line vortex system with wake contributions resulting from a representative line vortex system.

where $K_L(y) := \frac{1}{2}c(y)m_o(y)$, with the boundary conditions,

$$\Gamma(-\tilde{b}/2) = \Gamma(\tilde{b}/2) = 0. \tag{6.15}$$

For discussion on solving this integro-differential equation via the collocation method, consult Section 6.2.2.1.

Once this integro-differential equation is solved for the $\Gamma(y)$ distribution, many other terms of interest easily follow. For example, it can be shown that for a flat plate the distribution of differential pressure coefficient will take the form

$$\Delta C_p(x,y) = -4\frac{\Gamma(y)}{\pi U_\infty c(y)}\left(\frac{c(y)}{x} - 1\right)^{1/2}. \tag{6.16}$$

6.2.2.1 Lifting Line Solution by the Collocation Method

We now present a method of solution for (6.14) with associated boundary conditions (6.15). A Fourier sine expansion is invoked for solving the integro-differential equation since the sine function automatically satisfies the boundary conditions at $y = -b/2$ and $y = b/2$. Let $\Gamma(\theta_i) = 2U_\infty b\sum_{n=1}^{\infty} a_n \sin n\theta_i$, with $y(\theta_i) = -(b/2)\cos\theta_i$. We first look at the integral term. We have,

$$\frac{\mathrm{d}\Gamma(\eta)}{\mathrm{d}\eta}\mathrm{d}\eta = \frac{\mathrm{d}\Gamma}{\mathrm{d}\theta}\frac{\mathrm{d}\theta}{\mathrm{d}\eta}\mathrm{d}\eta = \frac{\mathrm{d}\Gamma}{\mathrm{d}\theta}\mathrm{d}\theta = 2U_\infty b\sum_{n=1}^{\infty} n a_n \cos n\theta \mathrm{d}\theta.$$

Hence,

$$\frac{1}{4\pi}\int_{-b/2}^{b/2}\frac{\mathrm{d}\Gamma/\mathrm{d}\eta}{\eta-y}\mathrm{d}\eta=\frac{1}{4\pi}\int_{0}^{\pi}\frac{2U_\infty b\sum_{n=1}^{\infty}na_n\cos n\theta}{-\frac{b}{2}\cos\theta+\frac{b}{2}\cos\theta_i}\mathrm{d}\theta.$$

Substituting this into the original integro-differential equation (6.14) yields,

$$\begin{aligned}2U_\infty b\sum_{n=1}^{\infty}a_n\sin n\theta_i &= K_L(y(\theta_i))\left[R(\theta_i)-w_o(y(\theta_i);\Gamma_o,y_o,z_o)-\frac{U_\infty}{\pi}\int_0^{\pi}\sum_{n=1}^{\infty}\frac{na_n\cos n\theta}{\cos\theta-\cos\theta_i}\mathrm{d}\theta\right]\\ &= K_L(y(\theta_i))\left[R(\theta_i)-w_o(y(\theta_i);\Gamma_o,y_o,z_o)-\frac{U_\infty}{\pi}\sum_{n=1}^{\infty}na_n\int_0^{\pi}\frac{\cos n\theta}{\cos\theta-\cos\theta_i}\mathrm{d}\theta\right]\end{aligned}$$

where $R(\theta_i):=U_\infty\alpha(y(\theta_i))-W_{\mathrm{AC}}-\Omega_x y(\theta_i)$.

We now note the following integral identity,

$$\int_0^{\pi}\frac{\cos n\theta}{\cos\theta-\cos\theta_i}\mathrm{d}\theta=\pi\frac{\sin n\theta_i}{\sin\theta_i}.$$

Thus,

$$\sum_{n=1}^{\infty}a_n\sin n\theta_i=\frac{K_L(y(\theta_i))}{2U_\infty b}\left[R(\theta_i)-w_o(y(\theta_i);\Gamma_o,y_o,z_o)-U_\infty\sum_{n=1}^{\infty}\frac{na_n\sin n\theta_i}{\sin\theta_i}\right]$$

Upon rearranging terms and defining $\mu(\theta_i):=K_L(y(\theta_i))/2b$,

$$\sum_{n=1}^{\infty}\left\{a_n\sin n\theta_i\sin\theta_i+\mu(\theta_i)na_n\sin n\theta_i\right\}=\frac{\mu(\theta_i)}{U_\infty}\sin\theta_i\left[R(\theta_i)-w_o(y(\theta_i);\Gamma_o,y_o,z_o)\right].$$

We can finally write,

$$\sum_{n=1}^{\infty}a_n\sin n\theta_i\left(\sin\theta_i+\mu(\theta_i)n\right)=\frac{\mu(\theta_i)}{U_\infty}\sin\theta_i\left[R(\theta_i)-w_o(y(\theta_i);\Gamma_o,y_o,z_o)\right]. \qquad (6.17)$$

This equation can now be solved by truncating the series at a finite number and solving the resulting linear system of equations for the coefficients a_n.

6.3 Wake Observability

With the aerodynamic model established, preliminary considerations of system observability will provide general insights into the estimation problem at hand.

6.3.1 System Observability and Conditioning

The notion of system observability is well established in the context of identification and estimation of dynamical systems. If a system is observable, then its initial state can be determined uniquely from the sequence of system outputs taken during a given time interval. In the analysis of linear systems, a common test for system observability is the rank condition of the observability matrix $\mathcal{O}$. That is, for the system represented as

$$\begin{aligned} \mathbf{x}_{k+1} &= F\mathbf{x}_k + G\mathbf{u}_k \qquad (6.18) \\ \mathbf{z}_k &= H\mathbf{x}_k \qquad (6.19) \end{aligned}$$

with $\mathbf{x}_k \in \mathbb{R}^N$, $\mathbf{z}_k \in \mathbb{R}^M$, $F \in \mathbb{R}^{N\times N}$, $G \in \mathbb{R}^{N\times P}$, and $H \in \mathbb{R}^{M\times N}$, the system is said to be observable if and only if

$$\mathrm{rank}\mathcal{O} = \dim \mathbf{x} = N \qquad (6.20)$$

where

$$\mathcal{O} := \begin{bmatrix} H \\ HF \\ HF^2 \\ \vdots \\ HF^{M-1} \end{bmatrix}. \qquad (6.21)$$

For a static system, or equivalently one in steady-state, $F = I$. In this case, the rank condition for observability is equivalent to

$$\mathrm{rank}H = N. \qquad (6.22)$$

A similar rank condition can also be employed to determine the local observability of a non-linear system for a given state, though concepts from differential geometry are requisite in the resulting test. For static systems, however, the rank test is equivalent to that for linear systems. That is, satisfaction of (6.22) demonstrates local observability about a nominal state for a static nonlinear system. Of course, for general non-linear systems, even if the rank condition is satisfied, it may not be possible to determine the initial state uniquely because the rank test only applies to *local* observability. To determine the sensitivity of the measurements to the system states, we invoke the notion of the condition number from numerical analysis.

In general, the condition number for the matrix $A \in \mathbb{R}^{m \times n}$ is defined as

$$\kappa(A) := \|A\| \|A^{+}\| \tag{6.23}$$

and is a standard measure of the sensitivity of a matrix to numerical operations. It can also be interpreted as a measure of a system's sensitivity to small perturbations. That is, a large condition number implies that any small perturbation in the problem may be magnified greatly in the solution of the system.

As such, considering the condition number of $\mathcal{O}$ provides a basis for determining the well-posedness of the estimation problem under consideration, and thus represents an objective measure of the observability of a given nominal state from a prescribed set of measurements. The conditioning of the local observability matrix also provides a reasonable performance index for the sensor placement optimization problem. By determining a sensor configuration such that condition number is below a certain threshold over the region of interest, and such that the average condition number is minimized, the sensors configuration can be declared an optimal one.

6.3.2 Lifting Line Based Measurement Jacobian

The measurement Jacobian associated with the augmented lifting line model is useful in assessing the observability of the system, as described above. It can also be used to provide an analytical form for the filtering algorithms of Chapter 5.

Given a particular wing geometry, the lifting line matrix L can be constructed. In conjunction with knowledge of the external flow-field (which is a function of the vortex parameters $\mathbf{x}$), the strength distribution $\mathbf{\Gamma}(\mathbf{y}; \mathbf{x})$ can be determined as

$$\mathbf{\Gamma}(\mathbf{y}; \mathbf{x}) = 2U_{\infty} b \tilde{S} \mathbf{a} \tag{6.24}$$

where

$$\mathbf{a} = L^{-1}\mathbf{b}(\mathbf{y};\mathbf{x}) \tag{6.25}$$

with

$$\begin{aligned}
\mathbf{b}(\mathbf{y};\mathbf{x}) &:= \frac{1}{U_\infty} Q(y)\tilde{S}_D(y)\left[\mathbf{r}(\mathbf{y}) - \mathbf{w}_o(\mathbf{y};\mathbf{x})\right]^{\mathsf{T}} \in \mathbb{R}^M && (6.26)\\
Q(\mathbf{y}) &:= \operatorname{diag}\left[\begin{array}{ccccc} \mu(\theta(y_1)) & \dots & \mu(\theta(y_i)) & \dots & \mu(\theta(y_M)) \end{array}\right] \in \mathbb{R}^{M\times M} && (6.27)\\
\tilde{S}_D(\mathbf{y}) &:= \operatorname{diag}\left[\begin{array}{ccccc} \sin(\theta(y_1) & \dots & \sin(\theta(y_i))) & \dots & \sin(\theta(y_M)) \end{array}\right] \in \mathbb{R}^{M\times M} && (6.28)
\end{aligned}$$

and

$$\tilde{S} := \begin{bmatrix}
\sin(\theta(y_1)) & \dots & \sin(n\theta(y_1)) & \dots & \sin(M\theta(y_1)) \\
\vdots & \vdots & \vdots & \vdots & \vdots \\
\sin(\theta(y_i)) & \dots & \sin(n\theta(y_i)) & \dots & \sin(M\theta(y_i)) \\
\vdots & \vdots & \vdots & \vdots & \vdots \\
\sin(\theta(y_M)) & \dots & \sin(n\theta(y_M)) & \dots & \sin(M\theta(y_M))
\end{bmatrix} \in \mathbb{R}^{M\times M}. \tag{6.29}$$

The measurement Jacobian matrix H is defined as

$$H(\mathbf{y};\mathbf{x}) := \frac{\partial \mathbf{h}(\mathbf{y};\mathbf{x})}{\partial \mathbf{x}} \in \mathbb{R}^{M\times N}. \tag{6.30}$$

Here, $\mathbf{h}(y;\mathbf{x}) = \Delta\mathbf{C}_p(\mathbf{y};\mathbf{x}) \in \mathbb{R}^M$, where $\Delta\mathbf{C}_p$ is determined from the solution of the lifting line equation as

$$\Delta\mathbf{C}_p(\mathbf{y};\mathbf{x}) = K\boldsymbol{\Gamma}(\mathbf{y};\mathbf{x}) \tag{6.31}$$

where

$$K := \operatorname{diag}\left[\begin{array}{ccccc} \kappa_1 & \dots & \kappa_i & \dots & \kappa_M \end{array}\right] \in \mathbb{R}^{M\times M} \tag{6.32}$$

is a constant diagonal matrix with given elements κ_i.

We now consider $H = \partial(\Delta\mathbf{C}_p)/\partial\mathbf{x}$ via successive invocations of the chain rule of matrix calculus (with some abuse of notation in representing vector valued functions as their matrix counterparts).

$$\begin{aligned} H &= \frac{\partial(\Delta\mathbf{C}_p)}{\partial\mathbf{x}} = \frac{\partial(K\mathbf{\Gamma})}{\partial\mathbf{x}} = K\frac{\partial\mathbf{\Gamma}}{\partial\mathbf{x}} && (6.33) \\ &= K\frac{\partial(2U_\infty b\tilde{S}\mathbf{a})}{\partial\mathbf{x}} = 2U_\infty bK\tilde{S}\frac{\partial\mathbf{a}}{\partial\mathbf{x}} && (6.34) \\ &= 2U_\infty bK\tilde{S}\frac{\partial(L^{-1}\mathbf{b})}{\partial\mathbf{x}} = 2U_\infty bK\tilde{S}L^{-1}\frac{\partial\mathbf{b}}{\partial\mathbf{x}} && (6.35) \\ &= 2U_\infty bK\tilde{S}L^{-1}\frac{\partial}{\partial\mathbf{x}}\left\{\frac{1}{U_\infty}Q\tilde{S}_D\left[\mathbf{r}(\mathbf{y})-\mathbf{w}_o(\mathbf{y};\mathbf{x})\right]\right\} && (6.36) \\ &= 2bK\tilde{S}L^{-1}Q\tilde{S}_D\left[\frac{\partial\mathbf{r}}{\partial\mathbf{x}}-\frac{\partial\mathbf{w}_o}{\partial\mathbf{x}}\right] && (6.37) \end{aligned}$$

Since, $\mathbf{r}(\mathbf{y})$ is not a function of the vortex parameters, we finally have

$$H(\mathbf{y};\mathbf{x}) = -2bK\tilde{S}L^{-1}Q\tilde{S}_D\frac{\partial\mathbf{w}_o(\mathbf{y};\mathbf{x})}{\partial\mathbf{x}}. \qquad (6.38)$$

Before moving forward, we note that this result highlights the significance of the wake nonlinearity within the estimation problem. If we rewrite (6.38) as

$$H(\mathbf{y};\mathbf{x}) = A\frac{\partial\mathbf{w}_o(\mathbf{y};\mathbf{x})}{\partial\mathbf{x}} \qquad (6.39)$$

where $A := -2bK\tilde{S}L^{-1}Q\tilde{S}_D$, then we can identify the necessary conditions for the wake's local observability. Because

$$\text{rank}(BC) \leq \min\left\{\text{rank}B, \text{rank}C\right\}, \qquad (6.40)$$

we can say that in order for the wake to be locally observable, it is *necessary* that

$$\text{rank}\left\{\frac{\partial\mathbf{w}_o(\mathbf{y};\mathbf{x})}{\partial\mathbf{x}}\right\} = N. \qquad (6.41)$$

Stated another way,

$$\text{rank}H = N \longrightarrow \text{rank}\left\{\frac{\partial\mathbf{w}_o(\mathbf{y};\mathbf{x})}{\partial\mathbf{x}}\right\} = N. \qquad (6.42)$$

This only serves as a necessary condition because the rank of the linear mapping A also has influence on the observability structure of the wake.

Finally, the term $\partial \mathbf{w}_o/\partial \mathbf{x}$ depends on the number of vortex parameters under consideration. In the present context, we consider the case of $N = 3$ where

$$\mathbf{x} := \begin{bmatrix} \Gamma_o & y_o & z_o \end{bmatrix}^\mathsf{T} \in \mathbb{R}^3. \tag{6.43}$$

Then,

$$\mathbf{w}_o := \begin{bmatrix} w_{o,1} \\ \vdots \\ w_{o,i} \\ \vdots \\ w_{o,M} \end{bmatrix} = \begin{bmatrix} \frac{\Gamma_o}{2\pi}\left\{\frac{y_1-y_o+\frac{b}{2}}{(y_1-y_o+\frac{b}{2})^2+(z_1-z_o)^2} - \frac{y_1-y_o-\frac{b}{2}}{(y_1-y_o-\frac{b}{2})^2+(z_1-z_o)^2}\right\} \\ \vdots \\ \frac{\Gamma_o}{2\pi}\left\{\frac{y_i-y_o+\frac{b}{2}}{(y_i-y_o+\frac{b}{2})^2+(z_i-z_o)^2} - \frac{y_i-y_o-\frac{b}{2}}{(y_i-y_o-\frac{b}{2})^2+(z_i-z_o)^2}\right\} \\ \vdots \\ \frac{\Gamma_o}{2\pi}\left\{\frac{y_M-y_o+\frac{b}{2}}{(y_M-y_o+\frac{b}{2})^2+(z_M-z_o)^2} - \frac{y_M-y_o-\frac{b}{2}}{(y_M-y_o-\frac{b}{2})^2+(z_M-z_o)^2}\right\} \end{bmatrix} \in \mathbb{R}^M \tag{6.44}$$

$$\frac{\partial \mathbf{w}_o}{\partial \mathbf{x}} = \begin{bmatrix} \frac{\partial w_{o,1}}{\partial \Gamma_o} & \frac{\partial w_{o,1}}{\partial y_o} & \frac{\partial w_{o,1}}{\partial z_o} \\ \vdots & \vdots & \vdots \\ \frac{\partial w_{o,i}}{\partial \Gamma_o} & \frac{\partial w_{o,i}}{\partial y_o} & \frac{\partial w_{o,i}}{\partial z_o} \\ \vdots & \vdots & \vdots \\ \frac{\partial w_{o,M}}{\partial \Gamma_o} & \frac{\partial w_{o,M}}{\partial y_o} & \frac{\partial w_{o,M}}{\partial z_o} \end{bmatrix} \in \mathbb{R}^{M\times 3} \tag{6.45}$$

where

$$\frac{\partial w_{o.i}}{\partial \Gamma_o} = \frac{1}{2\pi}\left\{\frac{y_i - y_o + \frac{b}{2}}{(y_i - y_o + \frac{b}{2})^2 + (z_i - z_o)^2} - \frac{y_i - y_o - \frac{b}{2}}{(y_i - y_o - \frac{b}{2})^2 + (z_i - z_o)^2}\right\} \tag{6.46}$$

$$\frac{\partial w_{o.i}}{\partial y_o} = \frac{\Gamma_o}{2\pi}\left\{\frac{(y_i - y_o + \frac{b}{2})^2 - (z_i - z_o)^2}{\left[(y_i - y_o + \frac{b}{2})^2 + (z_i - z_o)^2\right]^2} - \frac{(y_i - y_o - \frac{b}{2})^2 - (z_i - z_o)^2}{\left[(y_i - y_o - \frac{b}{2})^2 + (z_i - z_o)^2\right]^2}\right\} \tag{6.47}$$

$$\frac{\partial w_{o.i}}{\partial z_o} = \frac{\Gamma_o}{2\pi}\left\{\frac{2(y_i - y_o + \frac{b}{2})(z_i - z_o)}{\left[(y_i - y_o + \frac{b}{2})^2 + (z_i - z_o)^2\right]^2} - \frac{2(y_i - y_o - \frac{b}{2})(z_i - z_o)}{\left[(y_i - y_o - \frac{b}{2})^2 + (z_i - z_o)^2\right]^2}\right\}. \tag{6.48}$$

6.3.3 Wake Observability and Conditioning Comparison

Thus far, the only measurements considered have been linear mappings of the nonlinear *upwash* distribution associated with the wake. This proves to be problematic because the vertical separation is an indistinguishable state when seen through upwash distribution alone. To make this fact clear, consider the upwash distribution rewritten in the following manner,

$$w_o(y;\mathbf{x}) = \frac{\Gamma_o}{2\pi}\left[\frac{\Delta y + \frac{b}{2}}{(\Delta y + \frac{b}{2})^2 + (\Delta z)^2} - \frac{\Delta y - \frac{b}{2}}{(\Delta y - \frac{b}{2})^2 + (\Delta z)^2}\right]. \tag{6.49}$$

Since the term Δz only appears in the form $(\Delta z)^2$, it is clear that there is no distinction between $\pm\Delta z$ from mappings of the upwash distribution. One way of resolving this issue is by augmenting the measurements associated with upwash distribution with additional measurement related to sidewash distribution,

$$v_o(y;\mathbf{x}) = \frac{\Gamma_o}{2\pi}\left[\frac{\Delta z}{(\Delta y + \frac{b}{2})^2 + (\Delta z)^2} - \frac{\Delta z}{(\Delta y - \frac{b}{2})^2 + (\Delta z)^2}\right]. \tag{6.50}$$

In doing so, the vertical separation of the wake is introduced as Δz, leading to the ability to distinguish between $\pm\Delta z$. We note that using mappings of the sidewash distribution alone leads to the same problem as before, except that now lateral separation becomes the indistinguishable state. A successful method must incorporate mappings of *both* upwash and sidewash distribution.

An additional method of increasing the observability of the wake parameters is to specify any sign restrictions within the problem statement. For example, since it is known a priori that the formation flies in the same direction, something can be said regarding the sign of Γ_o. In constructing the filter, it is useful to consider estimates such that $\Gamma_o > 0$. This helps alleviate any issues regarding distinctions in the sign of Γ_o.

We now quantify the observability structure of the wake as a field quantity based on condition number. The conditioning of the observability matrix will be assessed for static configurations making use of three different measurements: (1) wake-induced upwash, (2) wake-induced sidewash, and (3) both wake-induced upwash and sidewash. For the current analysis, it is assumed that the velocity field is due to the presence of the wake alone (i.e. the disturbance field associated with the aircraft and measurement probes is ignored). Since the aerodynamic measurements of interest can be represented as linear mappings of these distributions, it is useful to consider the isolated wake's observability structure. Based on (6.42), the isolated wake's observability matrix conditioning-map provides a "best-case" observability structure for the problem. The correctness of this map depends on the conditioning of the linear mapping that accounts for the presence of the body. The current study is mainly intended to illustrate the advantage of one measurement configuration over another.

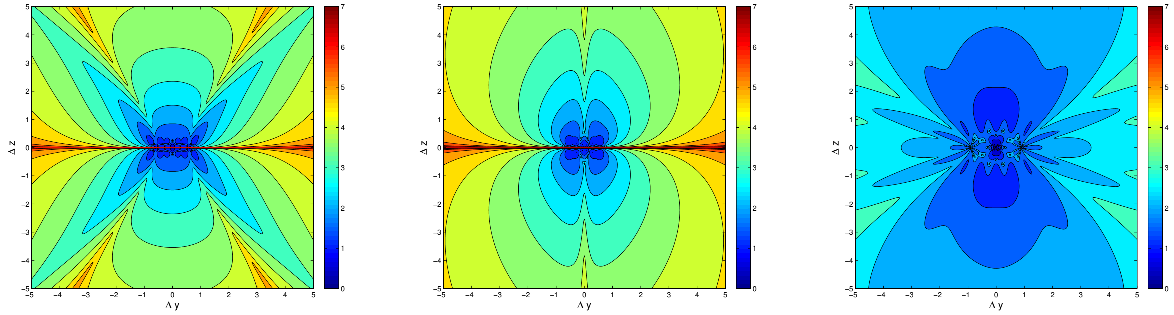

(a) upwash sensors

(b) sidewash sensors

(c) upwash and sidewash sensors

Figure 6.5: Observability conditioning based on various sensor-types. True wake strength is set to $\Gamma_o = 0.03$ and vortex separation is $b = 0.8$. The contours represent $\log_{10}(\kappa)$ of the local observability matrix at each field point. The sub-figures correspond to (a) 4 upwash measurements uniformly distributed from wing tip to wing tip. (b) 4 sidewash measurements uniformly distributed from wing tip to wing tip, and (c) 2 upwash and 2 sidwash measurements placed at the wing tips (i.e. two probe stations).

Based on the observability results presented in Figure 6.5, we see that the use of *both* upwash and sidewash measurements greatly improves the local observability structure of the wake in the full domain when compared to using *only* upwash or sidewash measurements. Of course, the actual sensors do not necessarily need to be altered if one is clever with regards to the final estimator implementation. For example, by rolling the aircraft with respect to the wake, both upwash and sidewash come into play. Thus, a sensor that only relies upon local upwash can be used to measure upwash- and sidewash-based quantities by manipulating the aircraft body-fixed coordinate system through specialized maneuvers.

6.4 Wake Estimation Algorithm

With the aerodynamic modeling established, a viable estimation strategy based on various nonlinear estimation approaches can be developed. The subsequent sections introduce a general framework for wake estimation that merges nonlinear estimation algorithms with the augmented lifting line model developed earlier in this chapter. Based on our review of nonlinear filtering and estimation in Chapter 5, we will focus on two classes of algorithms. First, Kalman-type algorithms will be considered, due to their computational simplicity and ability to handle process and measurement uncertainty. Additionally, particle filters are utilized to better handle the nonlinearities associated with the wake. All of the wake estimators developed in this work follow the same underlying approach (i.e. synthesizing distributed aerodynamic measurements with the aid of the augmented lifting line model developed in Section 6.2), but do so by means of different nonlinear stochastic estimation algorithms. The present section details various aspects pertaining to vortex model integration within the structure of these distinct algorithms.

We begin by defining the state and measurement vectors in Section 6.4.1. This is followed by discussion of measurement and process noises in Section 6.4.2. Our treatment of the measurement Jacobian for Kalman-type filters is reviewed in Section 6.4.3, while specific details of the particle filter are presented in Section 6.4.4. The vortex-based wake estimator requires a calibration step to prepare the filter for operation with arbitrary aircraft configurations. While many of the simulations conducted consider static aircraft configurations, several studies incorporate relative aircraft motions. The dynamics associated with these aircraft motions is detailed in Section 6.4.6.

6.4.1 States and Measurements

For the current discussion, we decide upon the following definitions,

$$\mathbf{x} := \begin{bmatrix} \Gamma_o \\ y_o \\ z_o \end{bmatrix} \in \mathbb{R}^3 \quad \text{and} \quad \mathbf{z} := \begin{bmatrix} \Delta C_{p_1} \\ \vdots \\ \Delta C_{p_i} \\ \vdots \\ \Delta C_{p_M} \end{bmatrix} \in \mathbb{R}^M \tag{6.51}$$

where $\mathbf{x}$ is the state vector and $\mathbf{z}$ is the measurement vector. Here, the states to be estimated are those associated with the relevant vortex parameters (c.f. Figures 6.2 and 6.3)

1. The strength of the pair, Γ_o, and
2. The lateral and vertical positions of the wake origin (i.e. the center of the vortex pair) relative to the aircraft's body-fixed coordinate system, (y_o, z_o).

Though we are mainly concerned with estimating the relative position of the wake, the associated vortex strength is an additional, but necessary, parameter to be estimated. In future works, the relative yaw angle (between the vortex-pair and wing axes) will need to be included as a parameter as well.

In the current implementation, we choose to use the spanwise differential pressure distribution as the measurement. The reason for this choice lies in simplifying the estimator's development process. Since the $\Gamma(y)$ distribution solved for within the lifting line model is directly related to $\Delta C_p(y)$ via equation (6.16), we have chosen the differential pressure distribution as the measurement within the current framework. Other measurements, such as angle of attack distribution, may also have merit. More importantly, the current algorithms are not restricted to distributed measurements alone; however, the use of distributed measurements allow valuable insights to be gained, so it is useful to consider such approaches first. If estimators relying upon distributed measurements lack in performance, then relying upon integrals over these distributions will be even more lacking. Although the ultimate hope is to rely upon on-board instrumentation exclusively for measurement data, validation under the distributed measurement framework must come first. The filter's ability to estimate the vortex parameters accurately from the on-board instrumentation alone has not yet been studied, but should be considered in future work.

6.4.2 Measurement and Process Noise

The process noise is currently only accounted for through the process covariance matrix W_k. No additive process noise is explicitly added within the simulation. Instead, process noise is implicitly introduced by means of model mismatch between the estimator model and the simulation environment. In an effort to keep the filter open, we always set $W_k > 0$. Since there is no process noise explicitly introduced within the simulation framework, W_k can be considered as a tuning parameter to be used in conditioning the filter for better performance.

Unlike the process noise, the measurement noise *is* explicitly introduced within the simulation. That is, the inputted measurement is assumed to have a white-noise signal, $\mathbf{v}_k \sim \mathcal{N}(0, V_k)$, added to it. Here, we assume the measurement has a "true" covariance of V_k^{true} when introducing noise to the measurement; however, within the filtering framework, we treat V_k as a tuning parameter. As such, V_k as defined within the context of the filter is not necessarily equal to V_k^{true}, and can be used to tune the filter.

We finally assume that our initial estimate for the vortex parameters is $\hat{\mathbf{x}}_o \sim \mathcal{N}(\bar{\mathbf{x}}_o, M_o)$. Again, the true estimate may have an initial covariance M_o^{true}, but we choose to treat M_o as a tuning parameter within the context of the filter.

6.4.3 Kalman-Type Filtering: Measurement Function Linearization

Kalman-type filters are one class of nonlinear estimation algorithm in this study. Details of the various algorithms can be found in Section 5.1 The present section only discusses computation of the measurement Jacobian matrix, H, which is required by Kalman-type filtering algorithms. For the vortex parameters $\mathbf{x}$ given above, this takes the form,

$$H = \begin{bmatrix} \frac{\partial \Delta C_{p_1}}{\partial \Gamma_o} & \frac{\partial \Delta C_{p_1}}{\partial y_o} & \frac{\partial \Delta C_{p_1}}{\partial z_o} \\ \vdots & \vdots & \vdots \\ \frac{\partial \Delta C_{p_i}}{\partial \Gamma_o} & \frac{\partial \Delta C_{p_i}}{\partial y_o} & \frac{\partial \Delta C_{p_i}}{\partial z_o} \\ \vdots & \vdots & \vdots \\ \frac{\partial \Delta C_{p_M}}{\partial \Gamma_o} & \frac{\partial \Delta C_{p_M}}{\partial y_o} & \frac{\partial \Delta C_{p_M}}{\partial z_o} \end{bmatrix} \in \mathbb{R}^{M \times 3}. \tag{6.52}$$

In the current implementation, the measurement Jacobian is computed numerically via first order finite differences applied to small perturbations about the nominal (estimated) state.

6.4.4 Particle Filtering Procedure

The second class of nonlinear estimation algorithm considered in this study is the Particle filter (PF). Particle filters approximate the Bayesian optimal filtering equations by means of Monte Carlo methods. The *a posteriori* probability density is represented by a set of random samples, or "particles", with associated weights. As the number of particles increases, the representation approaches the exact functional description of the probability distribution [RAG04].

As time progresses, the PF algorithm can lead to degeneracy due to overweighting a few samples, leaving the remaining ones useless. A common method of circumventing this issue comes in the form of a "resampling" step. The sequential important resampling (SIR) PF algorithm implemented in the present study makes use of a simple cumulative sum algorithm to resample particles at every time step. Further details regarding particle filters and resampling algorithms can be found in Section 5.2.

6.4.5 Offline Calibration

Prior to "hooking up" the filter, the lifting line model within the filter needs to be *calibrated in an isolated flight configuration.* That is, the lifting line model must be calibrated against the actual measurement data offline in order to initialize the model for best performance.

This is done by determining a linear gain vector ($\mathbf{k}_{\text{cal}} \in \mathbb{R}^M$) to apply to the model output,

$$\mathbf{k}_{\text{cal}} := \left[\begin{array}{ccccc} k_{\text{cal},1} & \ldots & k_{\text{cal},i} & \ldots & k_{\text{cal},M} \end{array} \right]^{\mathsf{T}}, \quad \text{where} \quad k_{\text{cal},i} := \frac{z_{i,\text{Measured}}}{z_{i,\text{Lifting Line}}}. \tag{6.53}$$

Calibration is important in the case of both simulation and flight testing. Within the context of simulation, calibration allows the filter to better account for variations between the aerodynamic model used to represent truth. Such calibration is also necessary for actual flight implementation because, in addition to modeling inaccuracies, unaccounted sensor biases may be present. In the case of pressure transducers, for example, such biases can be caused from installation or manufacturing errors. Calibrating the system offline introduces an element of robustness to the model because sensor biases can be better accounted for.

6.4.6 System Dynamics

The system dynamics studied in the current effort are simply prescribed sinusoidal changes in the relative vertical and lateral displacements between the wing and wake axes. Moreover, the constant amplitude and frequency of the sinusoidal velocity by which the wing moves is assumed to be fully known (i.e. there is no variance associated with these parameters). The vertical velocity of the wing influences the induced drag and, therefore, the pressure measurements. This is accounted for within the lifting line implementation. The lateral velocity is prescribed only for the purpose of "increasing the observability" of the vortex pair. Such prescribed motions are expected to increase the observability of the vortex pair because, though $\mathbf{h}_k(\mathbf{x}_k)$ is not necessarily invertible for all values of $\mathbf{x}_k$, the prescribed motions are more likely to describe a set $[\mathbf{h}_1(\mathbf{x}_1), \ldots, \mathbf{h}_{k-1}(\mathbf{x}_{k-1}), \mathbf{h}_k(\mathbf{x}_k)]$ that can only be generated from a unique set vortex parameters. From the standpoint of the system observability matrix, dynamics increases the number of rows in H, potentially leading to $\text{rank} H = N$. This is consistent with the discussion of incorporating both upwash and sidewash mappings as measurements for improved observability, since relative motions can serve as a means of introducing these mapping combinations.

We denote the lateral and vertical velocity components of the wing as $V_y(t_k)$ and $V_z(t_k)$

respectively. For the purpose of simulation, we choose to move the wake with respect to the aircraft rather than to move the aircraft with respect to the wake. In doing so, we may ignore upwash/sidewash effects due to motions of the lifting surfaces. This provides a greater opportunity of distinguishing the wake's upwash signature because it is less likely to be "washed out" by the presence of these additional disturbance-fields. Thus, for purposes of the estimator simulation, we can consider that the wing "sees" the vortex pair move with equal but opposite velocity components, ignoring all velocities due to motion of the solid bodies. Hence,

$$\begin{aligned} y_o^{(k+1)} &= y_o^{(k)} - V_y(t_k)\Delta t_k && (6.54) \\ z_o^{(k+1)} &= z_o^{(k)} - V_z(t_k)\Delta t_k. && (6.55) \end{aligned}$$

In other words, the dynamical equations for this system can be written as,

$$\begin{bmatrix} \Gamma_o \\ y_o \\ z_o \end{bmatrix}_{k+1} = \begin{bmatrix} \Gamma_o \\ y_o \\ z_o \end{bmatrix}_k + \begin{bmatrix} 0 \\ -V_y(t_k)\Delta t_k \\ -V_z(t_k)\Delta t_k \end{bmatrix}. \qquad (6.56)$$

Although other aspects of the aircraft dynamics have not been included here (e.g. roll and yaw kinematics), we plan to consider these aspects in future works. In the present study, only fundamental aspects of the filter have been considered. As such, we have dealt only with parameters that are expected to represent the capabilities of the filter, while keeping things as intuitive as possible.

6.5 Performance Results and Discussion

Vortex lattice simulations of a generic aircraft equipped with wing-distributed pressure sensors have been studied to assess the wake estimation algorithm's performance characteristics. The simplest possible aircraft is chosen for the present study because of the limitations associated with the classical lifting line approach in modeling sophisticated geometries such as sweep and dihedral. As previously mentioned, the classical lifting line approach can be replaced with more sophisticated aerodynamic models (e.g. modern/extended lifting line methods or vortex panel methods) in the future. However, the classical lifting line method was selected due to its simplicity. Since the current focus is on the assessment of an estimation algorithm, the aerodynamic model must only be capable of capturing the class of nonlinearity associated with the process. Classical lifting line theory is entirely capable of doing this; it also provides a simple framework for tracking the influence of the fundamental wake nonlinearity on the overall estimator dynamics.

Two main types of simulations are considered in the vortex lattice results that follow:

1. Static configuration—there is no relative motion between the aircraft and wake.
2. Prescribed relative motions—relative kinematics are prescribed between the aircraft and wake, thus introducing “dynamics”

In both instances, the same aircraft/sensor configuration is used (c.f. Figure 6.6). The level of noise associated with the sensor measurements is also consistent in both cases. Process noise is not present in the simulation, though a finite “truth” process noise is assumed for use in tuning the estimator. The corresponding noise levels are

$$\sigma_v^{\text{true}} = 1 \times 10^{-5}, \quad \sigma_w^{\text{true}} = 1 \times 10^{-3},$$

where σ_w^{true} refers to the initial uncertainty in the estimate (i.e. M_o discussed in Section 6.4.2) and is currently treated as a tuning parameter. Unless otherwise stated, the estimator tuning parameters have the following values

$$\sigma_v = 7 \times 10^{-3}, \quad \sigma_w = 3 \times 10^{-2}.$$

Finally, all values are presented in dimensionless form, using wing span, flight speed, and air density at 28,000 ft as factors for non-dimensionalization. A list of the various cases studied is presented in Table 6.1.

Case #	Wake Parameters (Γ_o, y_o, z_o)	Kinematics	Filtering Algorithm
1	$(0.03, -1, 0)$	Static	EKF
2a	$(0.03, -1.5, 1)$	Static	EKF
2b	$(0.03, -1.5, 1)$	Static	IEKF
2c	$(0.03, -1.5, 1)$	Static	SOEKF
2d	$(0.03, -1.5, 1)$	Static	PF
3	$(0.03, -1, 0)$	$A = 0.05, \omega = 0.05$	EKF
4a	$(0.03, -1.5, 1)$	$A = 0.5, \omega = 0.05$	EKF
4b	$(0.03, -1.5, 1)$	$A = 0.5, \omega = 0.001$	EKF

Table 6.1: Specifications of the cases studied based on Case #, Wake Parameters, Kinematics, and Filtering Algorithm. "Static" refers to a configuration with no relative motions between aircraft and wake, while cases with relative motions are defined with respect to the kinematic parameters A and ω defined in Section 6.5.2. The filtering algorithms presented here are the extended Kalman filter (EKF), the iterative EKF (IEKF), the second-order EKF (SOEKF), and the particle filter (PF).

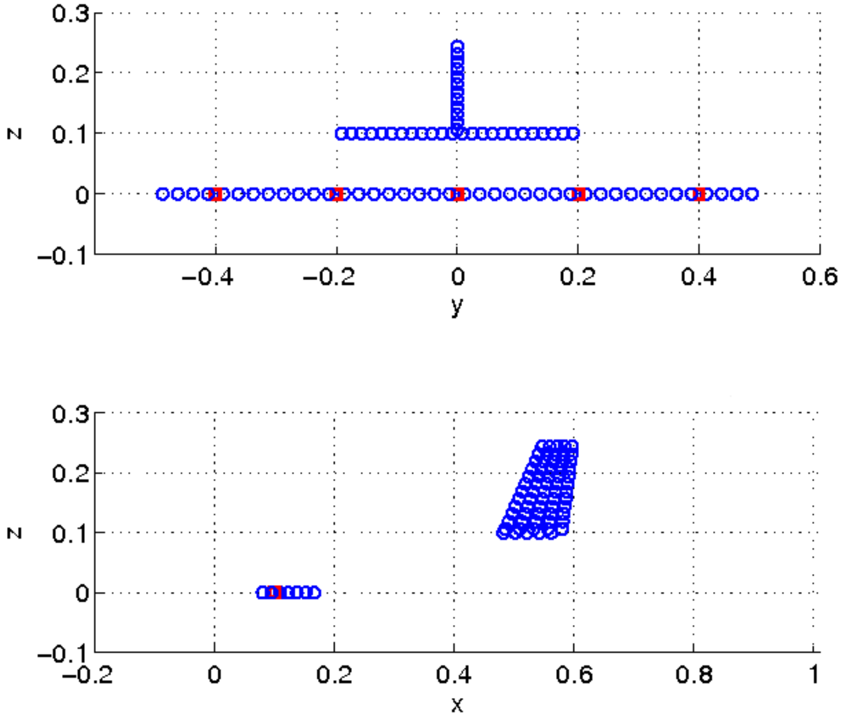

Figure 6.6: Aircraft configuration for the vortex panel simulation using five uniformly spaced wing-distributed pressure sensors. Vortex panel collocation points are denoted by ○, while the five uniformly spaced pressure sensors are denoted by □. The lower figure depicts the taper and sweep present in the vertical stabilizer as well as the relative position of the tail to the main lifting surface. All other lifting surfaces are untapered and unswept for the present study.

6.5.1 Two-Aircraft Static Configuration

Several simulation results for the static configuration are presented below. Case 1, presented in Figure 6.7 provides a validation for a simple case using an EKF; the wake is close to the trailing aircraft, thus leaving a relatively strong signature on it. Based on both the estimation trajectory map and the error histories, one can see that the estimator does a reasonable job zeroing in on the relative wake location. The estimate of the wake strength, however, does not perform as well. The error associated with the estimate of Γ_o is on the same order of the quantity itself. An interesting point to note is that this tends to be a common trend among most of the simulations conducted. Several studies were previously conducted, albeit briefly, on the effect of removing the wake strength Γ_o as a parameter to be estimated (i.e. assuming Γ_o is fully known). The results of these simulations, surprisingly, led to degraded estimator performance! This can be explained by reflecting on the large amount of error present in Γ_o when it is included as an estimation parameter. It turns out that much of the process uncertainty is lumped into Γ_o. As a result, when it is removed as an estimation parameter, the estimates of the wake coordinates are more greatly affected by these uncertainties. Since the wake coordinates are the parameters of interest in formation flight applications, the poor estimate of Γ_o is not of great concern and is kept so as to improve the quality of (y_o, z_o) estimates.

Case 2 considers a configuration with one and one-half wing spans of lateral separation and one wing span of vertical separation. Four different estimation algorithms were studied. The three Kalman-type filters (EKF, IEKF, SOEKF) yielded similar results, all of which led to significant biases or filter divergence depending on the initial estimates. The particle filter alleviated the bias issues, but divergence was still a problem. This indicates a potential unobservability that is not being properly handled by the sensor configuration, prompting need for further investigation.

6.5.1.1 Extended Kalman Filter

The EKF in Case 2a, presented in Figures 6.8 and 6.9, reveals the presence of attractors in the estimation error space. The position estimate follows a similar trajectory for several different initial estimates, and always leads to the same biased position estimate. In one of the cases presented, the estimate actually diverges! The wake nonlinearity and its associated observability structure are responsible for this behavior, though further investigation is necessary to determine methods for resolving these issues. Such investigations are considered in subsequent sections, and make use of different filtering methods as well as relative motions between aircraft. This allows the cause of bias and divergence to be isolated to either the wake nonlinearity or observability issues in an empirical manner.

6.5.1.2 Iterative Kalman Filter

The IEKF wake estimator of Case 2b resulted in no noticeable difference from the results of the EKF. The IEKF implementation used $\epsilon = 10^{-3}$ as a convergence criterion for each iteration, while the maximum allowable number of iterations was capped at 1000. Using ϵ values smaller than this, or allowable number of iterations larger than this, results in significant computational expense. For the implementation to be practical, we restricted the estimator values to the ones reported above. The fact that the IEKF results do not vary significantly from those of the EKF warrants use of a higher order filter, as will be done in the following section with the SOEKF.

Second Order Kalman Filter The SOEKF (Case 2c) failed to demonstrate significant performance differences from the EKF and IEKF implementations. In fact, Figures 6.12 and 6.13 are difficult to distinguish from the corresponding EKF and IEKF figures without the identifying labels. It is clear that the wake nonlinearity is sufficiently strong to motivate moving to a particle filtering approach.x

6.5.1.3 Particle Filter

In implementing the PF for wake estimation, we set the following parameter values

$$N_p = 1000, \quad \sigma_v = 3 \times 10^{-4}, \quad \sigma_w = 1 \times 10^{-2}.$$

The PF results, presented in Figures 6.14 and 6.15, demonstrate the greatest performance among the four wake estimation algorithms studied. Because the PF propagates statistics through the vortex nonlinearity directly, without relying upon successive linearizations, the biases due to small modeling errors are minimized. However, as a result of system unobservability, one of the estimates continues to diverge. In the next section, relative motions are shown to alleviate the divergent behavior. This empirical result demonstrates that the divergence is a result of an unobservable wake. Future work must focus on better understanding and reconciling this unobservability issue.

6.5.2 Two-Aircraft with Relative Motions

The divergence issues arising in Cases 2a and 2b are most likely attributed to wake unobservability. Since the PF also exhibited the same divergent behavior, the wake nonlinearity cannot be blamed for this shortcoming. To empirically verify that the observability structure of the wake is responsible for divergence, the following section considers the effect of relative motion on the performance of the wake estimation algorithm. It is hypothesized that introducing relative motions between the aircraft and the wake can lead to improvements in the wake's observability structure, which should aid in resolving filter divergence. As the aircraft moves closer to the wake, the signature becomes more pronounced. Thus, a time sequence of wake signatures should be more revealing than a single wake signature with additive noise.

In the present study, only lateral dither signals are introduced. These relative lateral motions are prescribed as

$$\mathbf{x}_{k+1} = F_k \mathbf{x}_k + \Lambda_k \mathbf{u}_k$$

where

$$\begin{aligned} F_k &= I^{N \times N} \\ \Lambda_k &= \begin{bmatrix} 0 & 0 \\ A\omega & 0 \\ 0 & 0 \end{bmatrix} \\ \mathbf{u}_k &= \begin{bmatrix} \cos(\omega t) \\ 0 \end{bmatrix}. \end{aligned}$$

with time quantities normalized by Δt, the time period between subsequent sensor measurements. Since these tests address the observability structure of the wake, only the EKF results with various values of A and ω are presented here. Since these tests address the observability structure of the wake, only the EKF results with various values of A and ω are presented here.

A simple example of the incorporation of kinematics is presented via Case 3 (equivalent to Case 1, but with relative motion) in Figure 6.16. We note that $\sigma_w = 1 \times 10^{-3}$ for Case 3 only. Although the estimate appears to lock in on the z_o value in terms of phase, the actual estimate has a periodic error value in steady-state. Though not apparent under such weak forcing magnitude, the unforced channels (i.e. Γ_o and y_o) also have periodic values appearing in steady-state.

Cases 4a and 4b consider different sets of lateral dither parameters, leading to significantly different performance characteristics. It is found that the divergent behavior of the estimator in Cases 2a and 2b (c.f. Figure 6.9) can be eliminated under the kinematics prescribed in Case 4a (c.f. Figure 6.17). However, the resulting converged estimate is far from the correct value. On the other hand, the kinematics prescribed in Case 4b (c.f. Figure 6.18) continues to result in filter divergence, thus demonstrating that prescribing kinematics does not guarantee convergence. This clearly demonstrates that arbitrary motions alone are not sufficient to yield performance gains. Although dynamics have been shown to influence the wake's observability structure, both here and in Section 6.3, further study is needed in this area. The influence of dynamics on optimal system observability and estimator performance must be carefully studied if vortex-based wake estimation is to be successful in practice.

6.6 Conclusions

The current study has made much progress in understanding the nature of wake estimation and in developing a viable wake sensing strategy based on distributed aerodynamic measurements. Multiple attractors have been identified in the estimation error space associated with Kalman-type filters acting on the wake nonlinearity. Particle filters have been shown to alleviate this resulting bias, though divergence issues associated with the wake observability structure still remain an issue in static formations. Relative motions between the aircraft and the wake can help reduce the issues with divergence. Further study of the effect of relative motions on the observability structure of the wake and on the performance of the wake estimators is a necessary endeavor.

Additional factors to be considered in the optimal observability problem include sensor array configurations and additional classes of sensors. Such studies may require substitution of the lifting line model with more sophisticated models, such as extended lifting line or vortex lattice models, in order to handle additional geometric complexities and multi-body sensor distributions. These methods are analogous to classical lifting line methods and operate on the wake nonlinearity in a similar manner to attain aerodynamic quantities of interest. Though the computational demand of these methods is greater than that of the classical lifting line method, several strategies exist for keeping the cost at a level amenable to real-time implementation. For example, the collocation matrices associated with lattice methods can be precomputed, assuming the aircraft geometry itself does not undergo significant changes. Additional approaches may rely upon table look-ups for distributed aerodynamic quantities based on the set of vortex parameters; although, such methods tend to suffer from large memory burdens associated with storing the aerodynamic tables.

With a better handle of wake observability by means of these proposed studies, it may be possible to use integrated values of the aerodynamic quantities to say something about the wake parameters reliably as well. For example, by integrating the pressure distribution, the forces and moments can be deduced. Since this is a linear operation of the pressures, it remains a linear mapping of the wake nonlinearity. The necessary conditions for successful wake sensing will still include the conclusions made in the present study. However, by relying upon forces and moments, much of the signature associated with the wake is lost, and greater complexity is introduced to the problem by reducing the fidelity of the measurements to be incorporated. As a result, such an approach will require further studies of observability optimization. The ultimate wake estimation algorithm will likely make use of both force and moment measurements as well as distributed aerodynamic quantities in order to make reliable estimates of the wake location.

Furthermore, although the effects of modeling error were studied by simulating the estimation strategy by means of a vortex lattice method, some classes of modeling errors were ignored. Prior to implementing the present estimation framework in physical experiments, it may be useful to consider the effects of wind gusts and transients, as well as wake-shape deformations, on estimator performance. Such tests can be conducted by way of the panel-particle method developed in Chapter 4

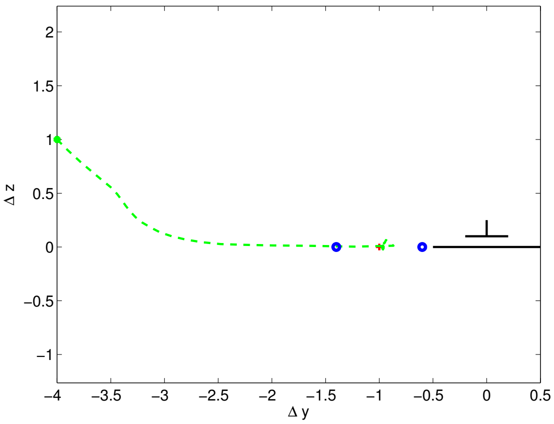

(a) Estimate Trajectory

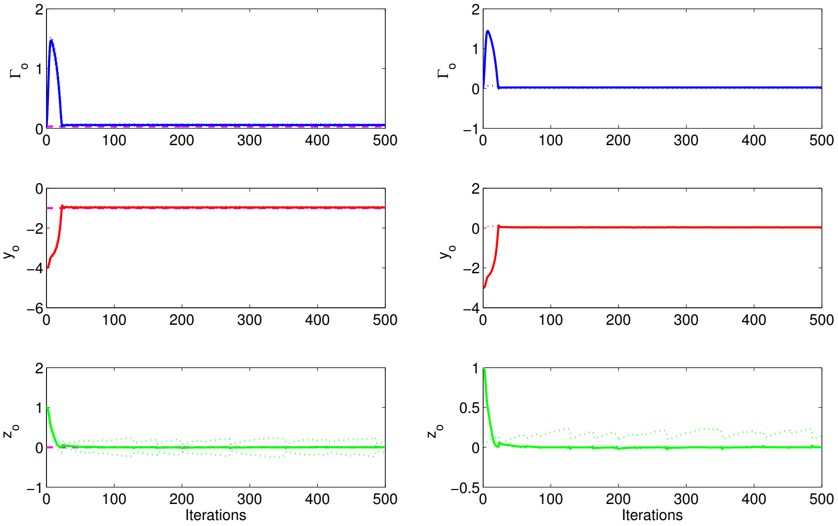

(b) Estimate Time History (c) Estimation Error Time History

Figure 6.7: Static wake simulation results for $\mathbf{x}_o = [0.03 \quad -1 \quad 0]^\mathsf{T}$ (Case 1) using the EKF estimator. In the estimated position trajectory map presented in (a), the vortex cores of the lead aircraft's wake are denoted by open circles ○ and their center by a cross +, the trailing (estimating) aircraft is drawn flying into the page, with the initial estimate denoted by a filled circle ● and the estimated trajectory drawn as a dashed line −−. In (b), the solid lines denote estimated values, the dotted lines denote 1-σ confidence levels surrounding the estimates, and the dashed line denote the true parameter value. In (c), the solid lines denote estimation errors and the dotted lines denote 1-σ confidence levels on the estimates.

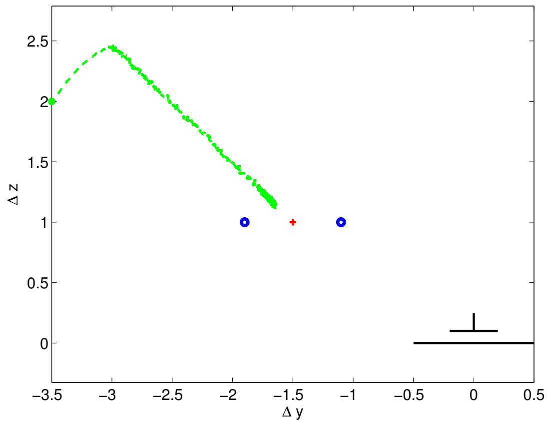

(a) Estimate Trajectory

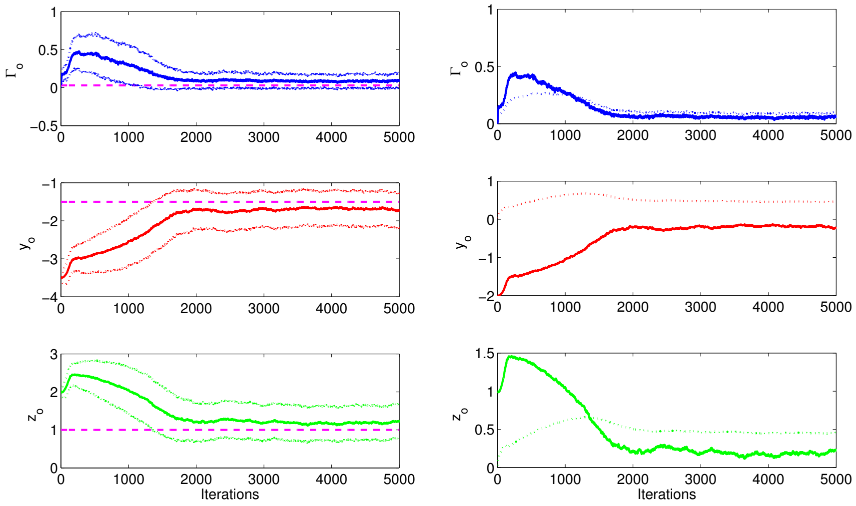

(b) Estimate Time History (c) Estimation Error Time History

Figure 6.8: Static wake simulation results for $\mathbf{x}_o = [0.03 \quad -1.5 \quad 1]^\mathsf{T}$ (Case 2a). In the estimated position trajectory map presented in (a), the vortex cores of the lead aircraft's wake are denoted by open circles ○ and their center by a cross +, the trailing (estimating) aircraft is drawn flying into the page, with the initial estimate denoted by a filled circle • and the estimated trajectory drawn as a dashed line −−. In (b), the solid lines denote estimated values, the dotted lines denote 1-σ confidence levels surrounding the estimates, and the dashed line denote the true parameter value. In (c), the solid lines denote estimation errors and the dotted lines denote 1-σ confidence levels on the estimates.

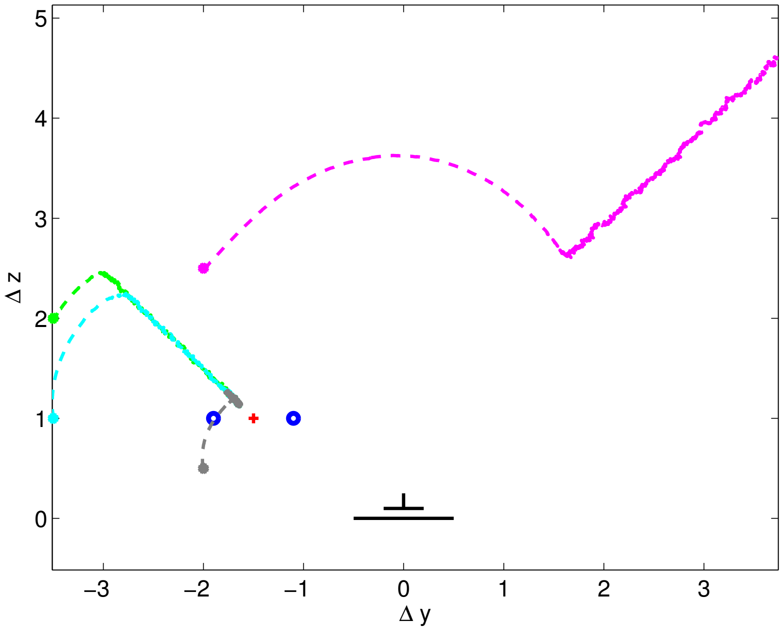

Figure 6.9: Estimated position trajectories associated with multiple initial estimates in Case 2a. In the estimated trajectory map presented, the vortex cores of the lead aircraft's wake are denoted by open circles ○ and their center by a cross +, the trailing (estimating) aircraft is drawn flying into the page, with the initial estimates denoted by various filled circles and the corresponding estimated trajectories are drawn as dashed lines.

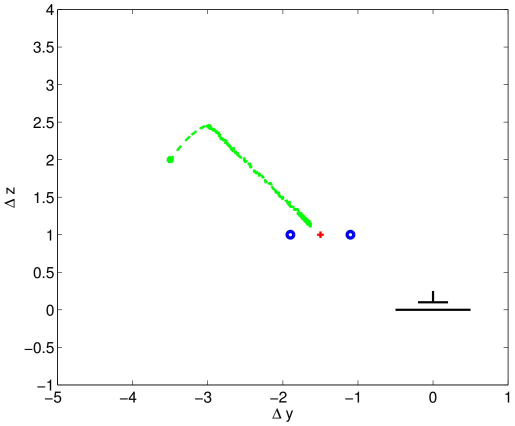

(a) Estimate Trajectory

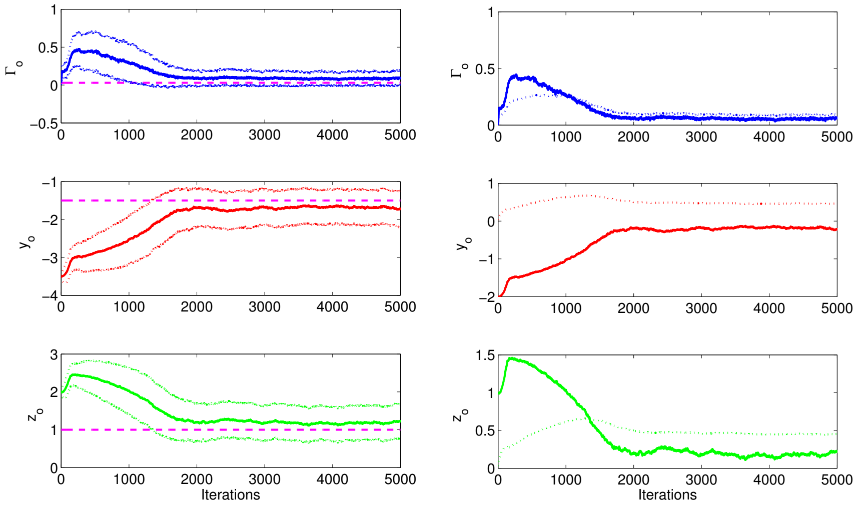

(b) Estimate Time History (c) Estimation Error Time History

Figure 6.10: Static wake simulation results for $\mathbf{x}_o = [0.03 \quad -1.5 \quad 1]^{\mathsf{T}}$ (Case 2b). In the estimated position trajectory map presented in (a), the vortex cores of the lead aircraft's wake are denoted by open circles ○ and their center by a cross +, the trailing (estimating) aircraft is drawn flying into the page, with the initial estimate denoted by a filled circle ● and the estimate trajectory drawn as a dashed line −−. In (b), the solid lines denote estimated values, the dotted lines denote 1-σ confidence levels surrounding the estimates, and the dashed lines denote the true parameter value. In (c), the solid lines denote estimation errors and the dotted lines denote 1-σ confidence levels on the estimates.

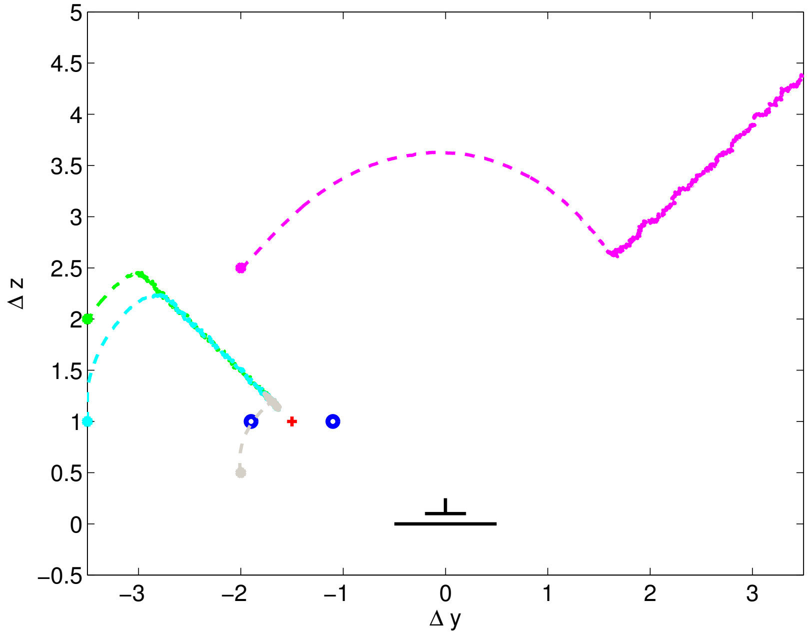

Figure 6.11: Estimated position trajectories associated with multiple initial estimates using the IEKF in Case 2b. In the estimate trajectory map presented, the vortex cores of the lead aircraft's wake are denoted by open circles ○ and their center by a cross +, the trailing (estimating) aircraft is drawn flying into the page, with the initial estimates denoted by various filled circles and the corresponding estimated trajectories are drawn as dashed lines.

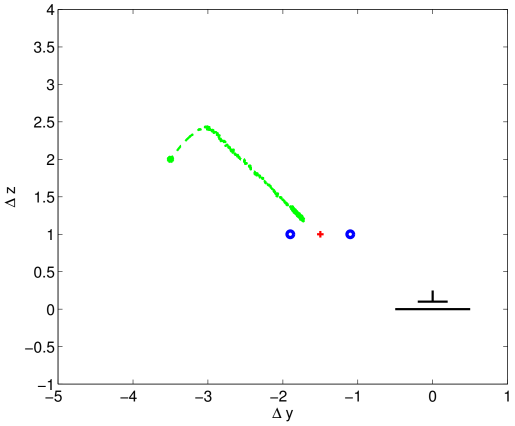

(a) Estimate Trajectory

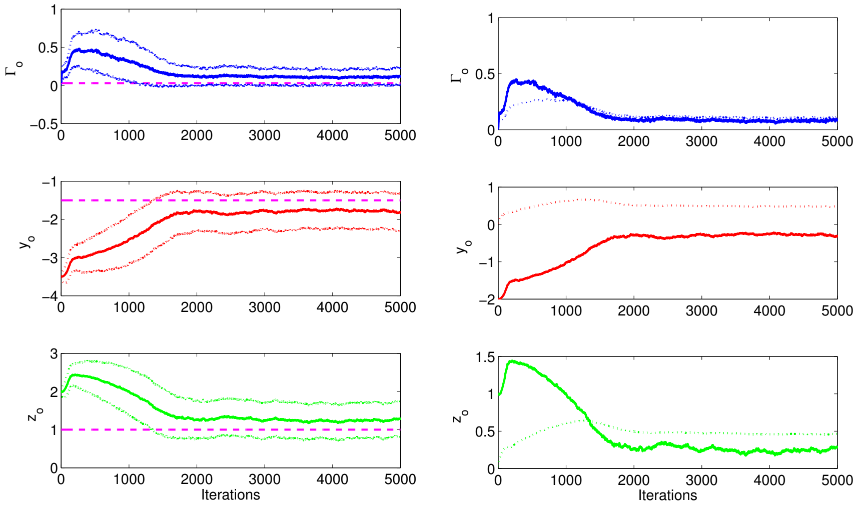

(b) Estimate Time History (c) Estimation Error Time History

Figure 6.12: Static wake simulation results for $\mathbf{x}_o = [0.03 \quad -1.5 \quad 1]^\mathsf{T}$ (Case 2c). In the estimated position trajectory map presented in (a), the vortex cores of the lead aircraft's wake are denoted by open circles ○ and their center by a cross +, the trailing (estimating) aircraft is drawn flying into the page, with the initial estimate denoted by a filled circle ● and the estimated trajectory drawn as a dashed line ——. In (b), the solid lines denote estimated values, the dotted lines denote 1-σ confidence levels surrounding the estimates, and the dashed lines denote the true parameter value. In (c), the solid lines denote estimation errors and the dotted lines denote 1-σ confidence levels on the estimates.

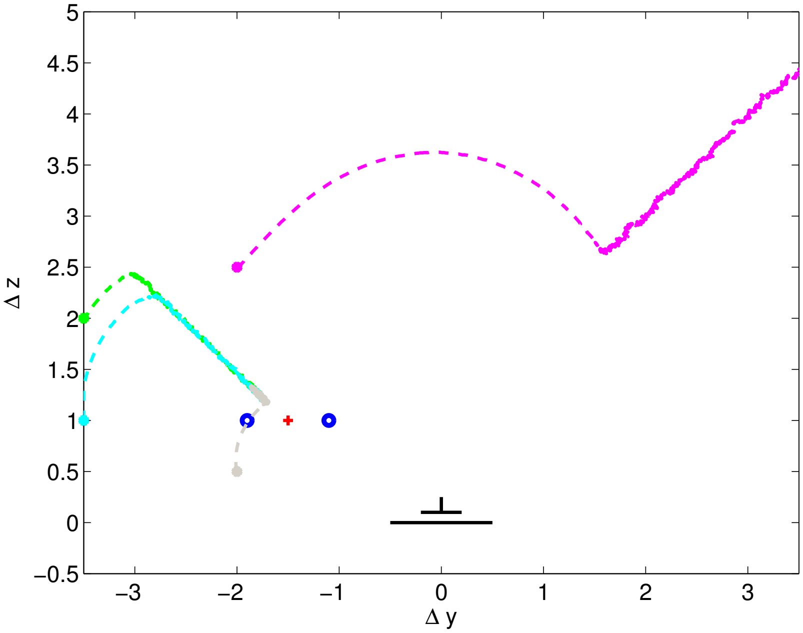

Figure 6.13: Estimated position trajectories associated with multiple initial estimates using the SOEKF in Case 2c. In the estimate trajectory map presented, the vortex cores of the lead aircraft's wake are denoted by open circles ○ and their center by a cross +, the trailing (estimating) aircraft is drawn flying into the page, with the initial estimates denoted by various filled circles and the corresponding estimated trajectories are drawn as dashed lines.

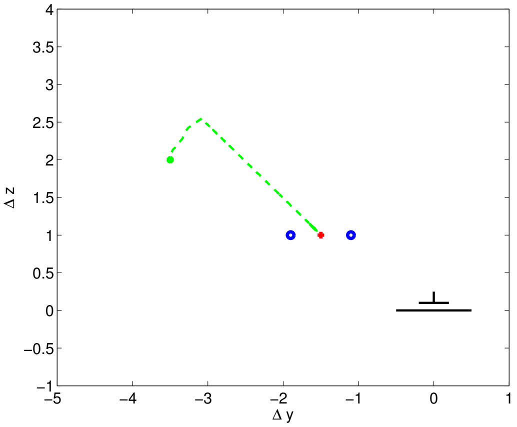

(a) Estimate Trajectory

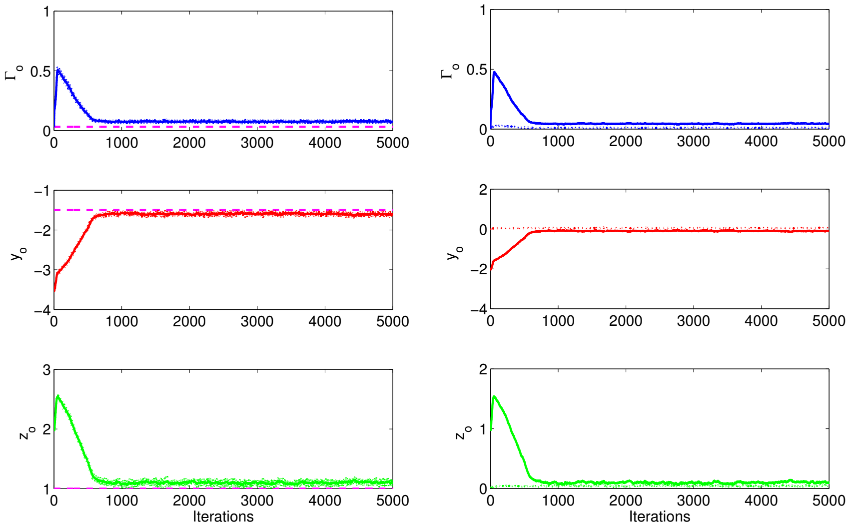

(b) Estimate Time History

(c) Estimation Error Time History

Figure 6.14: Static wake simulation results for $\mathbf{x}_o = [0.03 \quad -1.5 \quad 1]^\mathsf{T}$ (Case 2d). In the estimated position trajectory map presented in (a), the vortex cores of the lead aircraft's wake are denoted by open circles ○ and their center by a cross +, the trailing (estimating) aircraft is drawn flying into the page, with the initial estimate denoted by a filled circle • and the estimated trajectory drawn as a dashed line −−. In (b), the solid lines denote estimated values, the dotted lines denote 1-σ confidence levels surrounding the estimates, and the dashed line denote the true parameter value. In (c), the solid lines denote estimation errors and the dotted lines denote 1-σ confidence levels on the estimates.

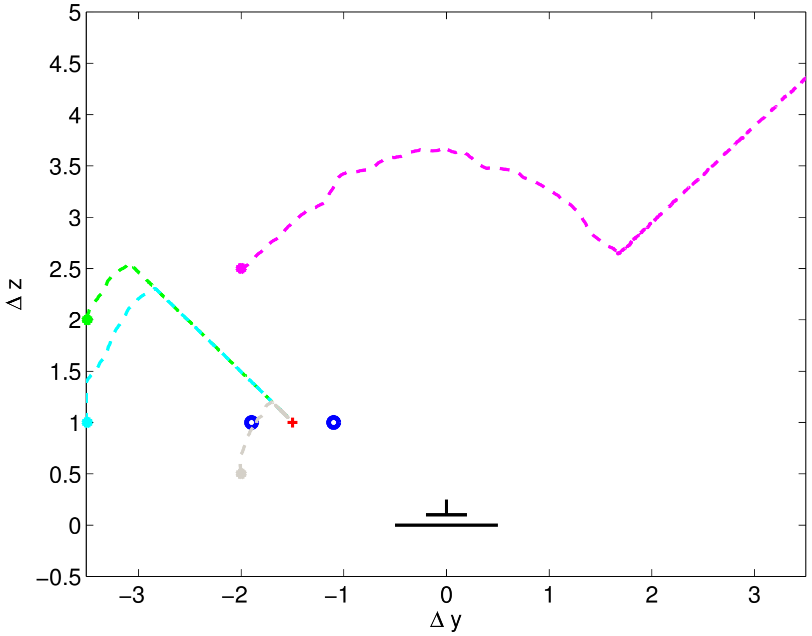

Figure 6.15: Estimated position trajectories associated with multiple initial estimates in Case 2d. In the estimated trajectory map presented, the vortex cores of the lead aircraft's wake are denoted by open circles ○ and their center by a cross +, the trailing (estimating) aircraft is drawn flying into the page, with the initial estimates denoted by circles of various colors and the corresponding estimated trajectories are drawn as dashed lines of the same color.

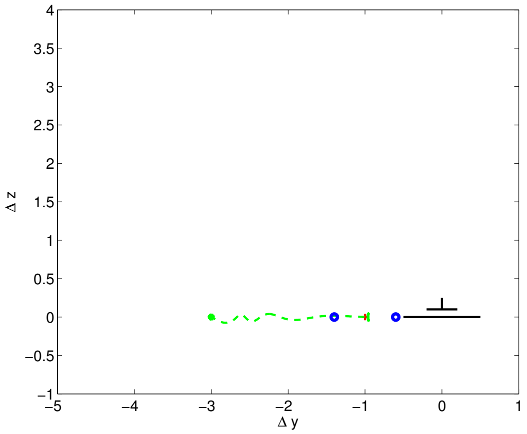

(a) Estimate Trajectory

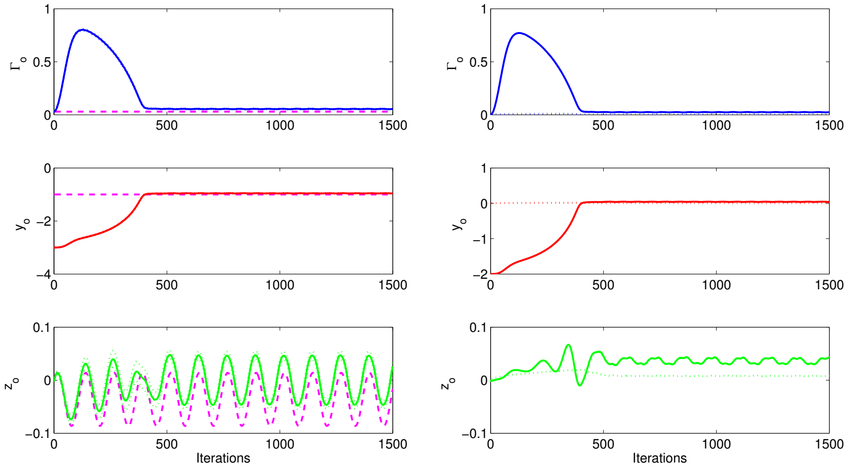

(b) Estimate Time History

(c) Estimation Error Time History

Figure 6.16: Relative motion simulation results for $\mathbf{x}_o = [0.03 \quad -1 \quad 0]^\mathsf{T}$ with $A = 0.05$ and $\omega = 0.05$ (Case 3). Note $\sigma_w = 1 \times 10^{-3}$ for this case only. In the estimate position trajectory map presented in (a), the vortex cores of the lead aircraft's wake are denoted by open circles ○ and their center by a cross +, the trailing (estimating) aircraft is drawn flying into the page, with the initial estimate denoted by a filled circle ● and the estimated trajectory drawn as a dashed line −−. In (b), the solid lines denote estimated values, the dotted lines denote 1-σ confidence levels surrounding the estimates, and the dashed line denote the true parameter value. In (c), the solid lines denote estimation errors and the dotted lines denote 1-σ confidence levels on the estimates.

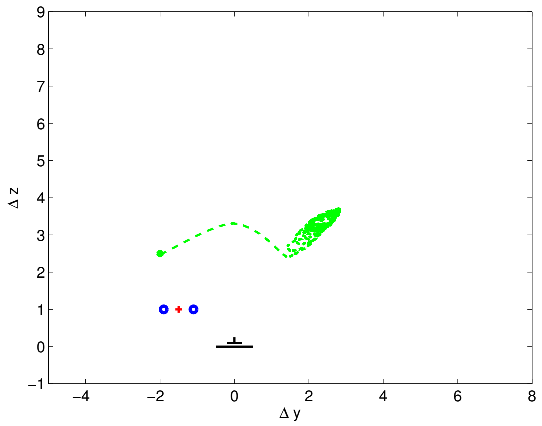

(a) Estimate Trajectory

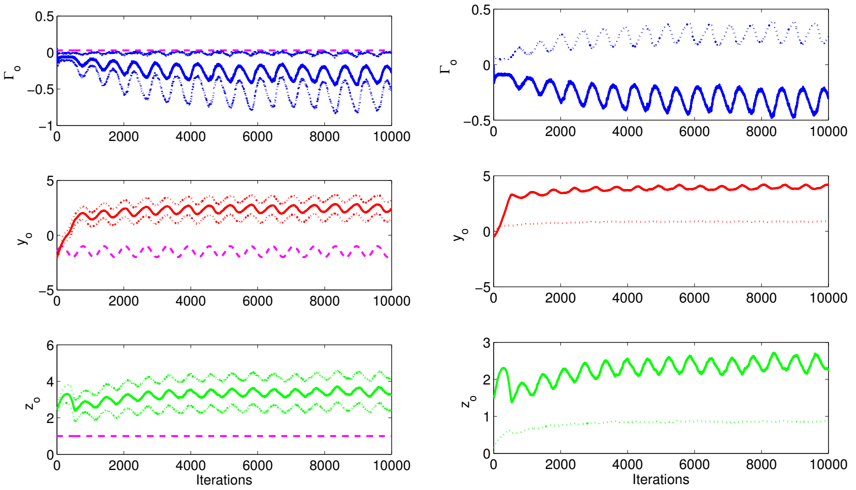

(b) Estimate Time History (c) Estimation Error Time History

Figure 6.17: Simulation identical to the static Case 2, but with relative motions prescribed as $A = 0.5$ and $\omega = 0.01$ (Case 4a). In the estimated position trajectory map presented in (a), the vortex cores of the lead aircraft's wake are denoted by open circles ○ and their center by a cross +, the trailing (estimating) aircraft is drawn flying into the page, with the initial estimate denoted by a filled circle ● and the estimated trajectory drawn as a dashed line −−. In (b), the solid lines denote estimated values, the dotted lines denote 1-σ confidence levels surrounding the estimates, and the dashed line denote the true parameter value. In (c), the solid lines denote estimation errors and the dotted lines denote 1-σ confidence levels on the estimates.

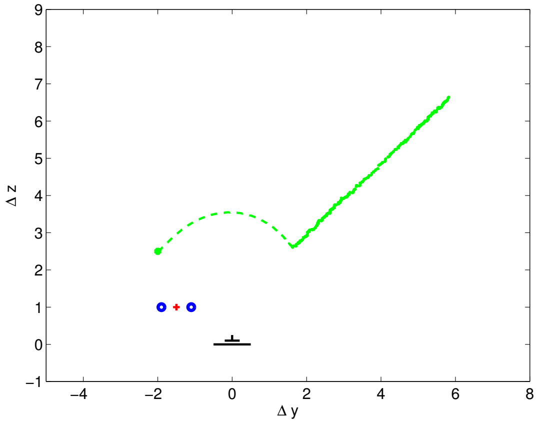

(a) Estimate Trajectory

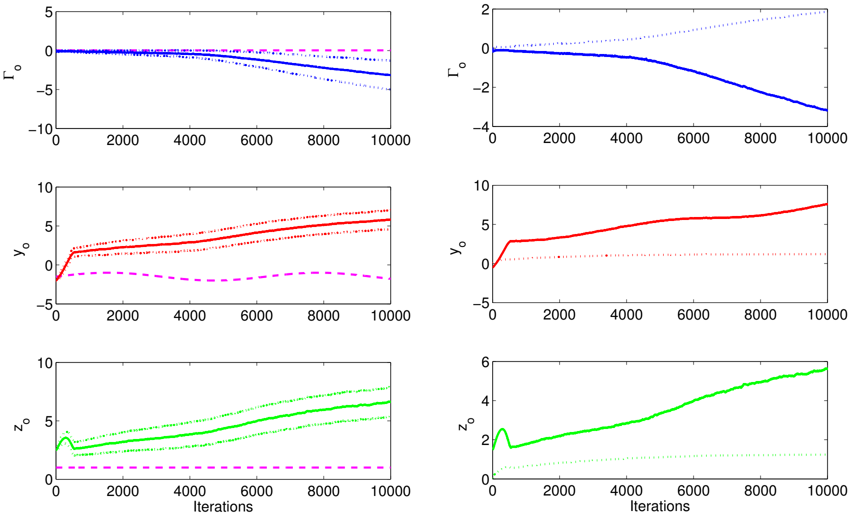

(b) Estimate Time History (c) Estimation Error Time History

Figure 6.18: Relative motion simulation identical to Case 4a, but with $A = 0.5$ and $\omega = 0.001$ (Case 4b). In the estimated position trajectory map presented in (a), the vortex cores of the lead aircraft's wake are denoted by open circles ○ and their center by a cross +, the trailing (estimating) aircraft is drawn flying into the page, with the initial estimate denoted by a filled circle ● and the estimated trajectory drawn as a dashed line −−. In (b), the solid lines denote estimated values, the dotted lines denote 1-σ confidence levels surrounding the estimates, and the dashed line denote the true parameter value. In (c), the solid lines denote estimation errors and the dotted lines denote 1-σ confidence levels on the estimates.

CHAPTER 7

Conclusions and Future Directions

Vortex-based aero- and hydrodynamic estimation has great potential to open avenues to new technologies in sensing and control for fluid mechanical systems. The present treatise discussed various aspects of the vortex-based estimation problem, namely modeling, simulation, and algorithm development. All of these aspects are requisite to the successful design and implementation of reliable flow estimation schemes.

Significant contributions to the modeling problem were made in Chapter 3, where a general vortex-based model reduction framework was established to guide improvements on low-order vortex models. We demonstrated the framework on Eldredge and Wang's impulse matching model [EW11, WE12] for two-dimensional pitching and translating wing maneuvers. By relaxing the Kutta conditions imposed in the original model, we were able to determine the optimal time rate of change in the leading and trailing edge vortex strengths so as to minimize the model predicted force error. In doing so, we highlighted the shortcomings of applying Kutta conditions at both edges for the classes of maneuvers considered. Additionally, we demonstrated the ability of a two point vortex model in accurately predicting the force response of a maneuvering wing. The results attained by means of the optimized models are quite remarkable; only six degrees of freedom were used in the vortex model, as opposed to $\mathcal{O}(10^6)$ for the high-fidelity results used as a baseline. This demonstration emphasizes the appeal of vortex-based models for real-time estimation and control of aero- and hydrodynamic systems.

In Chapter 4, we developed a pure particle implementation of a vortex panel-particle method for unsteady multi-body aerodynamic simulations. This tool serves as a reliable and efficient computational testbed for testing and validation of newly designed estimation and control strategies. By considering unsteady effects, such as wind gusts and wake evolution, the tool allows robustness issues to be revealed and resolved off-line with relative ease. There is no doubt that the availability of such a tool will enable more rapid development of viable controllers and estimators.

Additionally, much progress was made on wake sensing for aircraft formation flight missions. The full design, implementation, and test procedure for a vortex-based wake estimator was reported in Chapter 6. The strategy, which relied on a spanwise distribution of wing mounted pressure sensors, revealed challenges associated with the estimation task. We identified potential estimator bias and divergence issues that can arise when implementing estimators naïvely. A particle filter implementation was shown to overcome the issue of filter bias, primarily because it handled the nonlinear structure of the wake better than the Kalman-type filters. The challenge of filter divergence was shown to be one of poor wake observability, and was resolved by means of relative motions. However, further study is required to determine the best choice of maneuvers from an observability standpoint; the results reported in Chapter 6 alleviated divergence, but gave rise to additional biases.

The wake sensing problem is one of great interest for applications in aircraft formation flight, but it also serves as a basis for extending vortex-based aero- and hydrodynamic estimation to other application areas. For example, the past few decades have witnessed many efforts in actively controlling unsteady separation in a wide variety of application areas. A vortex-based approach to control and estimation has been considered by several authors, such as Cortelezzi et al. as presented in Section 1.3; however, such studies have yet to be pursued in more realistic settings. The optimized vortex models of Chapter 3 will likely enable further advancement in this area and make wing separation problems especially amenable to vortex-based control and estimation.

Advancements in autonomous underwater vehicle (AUV) systems can also be made using sensory feedback from the surrounding hydrodynamic environment. Not only are such inputs useful in determining the location of walls and sea-floors in dark waters, they also can serve to augment current mine detection and obstacle avoidance systems. Moreover, hydrodynamic sensing can prove advantageous in missions involving multiple underwater agents moving in swarms, especially when communication is limited due to physical signal or stealth mission restrictions. We can take inspiration from nature by observing that fish often experience dark and murky waters leading to strong selection for the use of non-visual senses. Among the mechanosensory systems utilized by fish, one of the most important is the lateral line system used in providing sensory feedback from the hydrodynamic environment [Jan04]. The lateral line system is essentially nature's extension of a vortex-based hydrodynamic estimator.

Within the last decade, much attention has been given to the problem of underwater object detection. Liu et al. have devised and implemented a MEMS-based lateral line system [FCZ02, PYJ06, YCE06], while Bouffanais et al. have made contributions to filtering algorithms for hydrodynamic object recognition from pressure sensors [BWY11]. Also noteworthy is the analysis of DeVries and Paley on the observability optimization problem for distributed flow sensing and control of a robotic fish [DP12]. Despite the advances made in this area, sensing technologies have not been adopted due to the lack of robustness associated with the hydrodynamic estimation schemes developed to date. A major aspect of this shortcoming in robustness is linked to the lack of a wake representation in most of the models considered. The vortex models discussed in the present work can be extended to provide reasonable wake models. The vortex-based estimation paradigm can then be invoked as a building-block in designing more reliable hydrodynamic estimation algorithms for use in AUV sensing applications.

It is clear that a variety of flow technologies stand to benefit from vortex-based aero- and hydrodynamic estimation. However, in order for these benefits to manifest themselves, future research must focus on reconciling the observability challenges that can arise from the vortex nonlinearity; appropriately managing this nonlinear structure is currently the limiting factor on reliable vortex-based estimation. With this obstacle surmounted, vortex-based flow control and estimation algorithms show great promise in advancing the state of the art a variety of application areas.

References

[ACG00] C.R. Anderson, Y.-C. Chen, and J.S. Gibson. "Control and Identification of Vortex Wakes." *Transactions of the ASME*, **122**:298–305, 2000.

[AK02] O.M. Aamo and M. Krstić. *Flow Control by Feedback.* Springer, 2002.

[AM79] B.O. Anderson and J.B. Moore. *Optimal Filtering.* Prentice-Hall, Englewood Cliffs, NJ, 1979.

[AMG02] M.S. Arulampalam, S. Maskell, N. Gordon, and T. Clapp. "A Tutorial on Particle Filters for Online Nonlinear/Non-Gaussian Bayesian Tracking." *IEEE Transactions on Signal Processing*, **50**(2):174–188, 2002.

[AR10] S. Ahuja and C.W. Rowley. "Feedback Control of Unstable Steady States of Flow Past a Flat Plate Using Reduced-Order Estimators." *Journal of Fluid Mechanics*, **645**:447–478, 2010.

[Ari62] R. Aris. *Vectors, Tensors, and the Basic Equations of Fluid Mechanics.* Dover Publications, New York, 1962.

[AS08] S. Alben and M.J. Shelley. "Flapping States of a Flag in an Inviscid Fluid: Bistability and the Transition to Chaos." *Physical Review Letters*, **100**(074301), 2008.

[AZK06] S.A. Ansari, R. Zbikowski, and K. Knowles. "Non-Linear Unsteady Aerodynamic Model for Insect-Like Flapping Wings in the Hover. Part 1: Methodology and Analysis." *Proceedings IMechE, Part G: Journal of Aerospace Engineering*, **220**(G2):61–83, 2006.

[BAK03] P. Binetti, K.B. Ariyur, and M. Krstić. "Formation Flight Optimization Using Extremum Seeking Feedback." *Journal of Guidance, Control, and Dynamics*, **26**(1):132–142, January–February 2003.

[Bat67] G.K. Batchelor. *An Introduction to Fluid Dynamics.* Cambridge University Press, Cambridge, 1967.

[BD67] J. Bellatoni and K. Dodge. "A Square Root Formulation of the Kalman-Schmidt Filter." *AIAA Journal*, **5**:1309–1314, 1967.

[BH75] A.E. Bryson and Y-.C. Ho. *Applied Optimal Control.* Hemisphere Publishing Corp., Washington, D.C., 1975.

[BM54] C.E. Brown and W.H. Michael. "Effect of Leading Edge Separation on the Lift of a Delta Wing." *Journal of the Aeronautical Sciences*, **21**:690–694, 1954.

[BM98] W. Blake and D. Multhopp. "Design, Performance and Modeling Considerations for Close Formation Flight." AIAA-98-4343, August 1998.

[BM08] G. Bramesfeld and M.D. Maughmer. "Effects of Wake Rollup on Formation-Flight Aerodynamics." *Journal of Aircraft*, **45**(4):1167–1173, July–August 2008.

[BMH07] S. Bradley, E. Mursch-Radlgruber, and S. von Hünerbein. "Sodar Measurements of Wing Vortex Strength and Position." *Journal of Atmospheric and Oceanic Technology*, **24**:141–155, February 2007.

[BR11] S.L. Brunton and C.W. Rowley. "Low-Dimensional Representations for Classical Unsteady Aerodynamic Models." In *AIAA Paper 2011-476*, 49th AIAA Aerospace Sciences Meeting, Orlando, FL, January 4–7 2011.

[BSA06] Z.A. Bangash, R.P. Sanchez, A. Ahmed, and M.J. Khan. "Aerodynamics of Formation Flight." *Journal of Aircraft*, **43**(4):907–912, July–August 2006.

[BTG02] O. Brun, V. Teuliere, and J-.M. Garcia. "Parallel Particle Filtering." *Journal of Parallel and Distributed Computing*, **62**:1186–1202, 2002.

[BWY11] R. Bouffanais, G.D. Weymouth, and D.K.P. Yue. "Hydrodynamic Object Recognition Using Pressure Sensing." *Proceedings of the Royal Society A*, **467**:19–38, 2011.

[CGS07] G. Campa, Y. Gu, B. Seanor, M.R. Napolitano, L. Pollini, and M.L. Fravolini. "Design and Flight-Testing of Non-Linear Formation Control Laws." *Journal of Control Engineering Practice*, **15**:1077–1092, 2007.

[CK00] G.-H. Cottet and P.D. Koumoutsakos. *Vortex Methods: Theory and Practice.* Cambridge University Press, Cambridge, 2000.

[CL93] L. Cortelezzi and A. Leonard. "Point Vortex Model of the Unsteady Separated Flow Past a Semi-Infinite Plate with Transverse Motion." *Fluid Dynamics Research*, **11**:263–295, 1993.

[CLD94] L. Cortelezzi, A. Leonard, and J.C. Doyle. "An Example of Active Circulation Control of the Unsteady Separated Flow Past a Semi-Infinite Plate." *Journal of Fluid Mechanics*, **260**:127–154, 1994.

[Cle73] R.R. Clements. "An Inviscid Model for Two-Dimensional Vortex Shedding." *Journal of Fluid Mechanics*, **57**(2):321–336, 1973.

[CS06] Y. Chen and C. Snyder. "Assimilating Vortex Position with an Ensemble Kalman Filter." *Monthly Weather Review*, **135**:1828–1845, 2006.

[CSF05] D.F. Chichka, J.L. Speyer, C. Fanti, and C.G. Park. "Peak-Seeking Control for Drag Reduction in Formation Flight." *Journal of Guidance, Control, and Dynamics*, **29**(5):1221–1230, September–October 2005.

[CTR12] K.K. Chen, J.H. Tu, and C.W. Rowley. "Variants of Dynamic Mode Decomposition: Boundary Condition, Koopman, and Fourier Analyses." *Journal of Nonlinear Science*, **22**(6):887–915, December 2012.

[CWS02] D.F. Chichka, J.D. Wolfe, and J.L. Speyer. "Aerodynamically Coupled Formation Flight of Aircraft." In *Proceedings of the 10th Mediterranean Conference on Control and Automation–MED2002*, Lisbon, Portugal, July 9-12 2002.

[Dav57] C.H. Davis. *Theory of the Motion of the Heavenly Bodies Moving about the Sun in Conic Sections: A Translation of Gauss's "Theoria Motus"*. Little, Brown, and Company, Boston, 1857.

[Dor66] B.D. Dore. "The Unsteady Forces on Finite Wings in Transient Motion." Technical Report 3456, Ministry of Aviation Aeronautical Research Council, 1966.

[DP12] L. DeVries and D.A. Paley. "Observability-Based Optimization for Distributed Flow Sensing and Control of a Robotic Fish in a Uniform Flowfield." International Symposium on Distributed Autonomous Robotic Systems, Baltimore, MD, November 8–11 2012.

[Dri12] R. Drinnon. "'Vortex Surfing' Could Be Revolutionary." Official Website of the US Air Force [online], 10 October 2012. [retrieved 15 October 2012].

[Eld07] J.D. Eldredge. "Numerical Simulation of the Fluid Dynamics of 2D Rigid Body Motion with the Vortex Particle Method." *Journal of Computational Physics*, **221**:626–648, 2007.

[Eld09] J.D. Eldredge. "A Reconciliation of Viscous and Inviscid Approaches to Computing Locomotion of Deforming Bodies." *Experimental Mechanics*, **50**(9):1349–1353, 2009.

[EW10] J.D. Eldredge and C. Wang. "High Fidelity Simulations and Low-Order Modeling of a Rapidly Pitching Plate." In *AIAA Paper 2010-4281*, 40th AIAA Fluid Dynamics Conference and Exhibit, Chicago, Illinois, June 28–July 1 2010.

[EW11] J.D. Eldredge and C. Wang. "Improved Low-Order Modeling of a Pitching and Perching Plate." In *AIAA Paper 2011-3579*, 41st AIAA Fluid Dynamics Conference and Exhibit, Honolulu, Hawaii, June 27–30 2011.

[FB12] C.W. Pitt Ford and H. Babinsky. "Lift and the Leading Edge Vortex." In *AIAA Paper 2012-0911*, 50th AIAA Aerospace Sciences Meeting, Nashville, TN, January 9–12 2012.

[FCZ02] Z. Fan, J. Chen, J. Zou, D. Bullen, C. Liu, and F. Delcomyn. "Design and Fabrication of Artificial Lateral Line Flow Sensors." *Journal of Micromechanics and Microengineering*, **12**:655–661, 2002.

[FG03] J.W. Frazier and A. Gopalarathnam. "Optimum Downwash behind Wings in Formation Flight." *Journal of Aircraft*, **40**(4):799–803, July–August 2003.

[Gad00] M. Gad-el-Hak. *Flow Control: Passive, Active, and Reactive Flow Management.* Cambridge University Press, Cambridge, 2000.

[Gel74] A. Gelb, editor. *Applied Optimal Control.* M.I.T. Press, Cambridge, MA, 1974.

[Gin99] D.R. Gingras. “Experimental Investigation of a Multi-Aircraft Formation.” AIAA-99-4143, June 1999.

[GIN05] F. Giulietti, M. Innocenti, M. Napolitano, and L. Pollini. “Dynamics and Control Issues of Formation Flight.” *Journal of Aerospace Science and Technology*, **9**:65–71, 2005.

[GK94] M.G. Goman and A.N. Khrabrov. “State-Space Representation of Aerodyanmics Characteristics of an Aircraft at High Angles of Attack.” *Journal of Aircraft*, **31**(5):1109–1115, 1994.

[GOG10] K. Granlund, M.V. Ol, D.J. Garmann, M.R. Visbal, and L. Bernal. “Experiments and Computations on Abstractions of Perching.” In *AIAA Paper 2010-4943*, 48th AIAA Applied Aerodynamics Conference, Chicago, IL, 2010.

[GR88] L. Greengard and V. Rokhlin. “The Rapid Evaluation of Potential Fields in Three Dimensions.” *Lecture Notes in Mathematics*, **1360**:121–141, 1988.

[Gra80] J.M.R Graham. “The Forces on Sharp-Edged Cylinders in Oscillatory Flow at Low Keulegan-Carpenter Numbers.” *Journal of Fluid Mechanics*, **97**(1):331–346, 1980.

[Gri03] G. Grisetti. *Bayesian State Estimation.* PhD thesis, Sapienza – Università di Roma, 2003.

[Gun95] M.D. Gunzburger, editor. *Flow Control.* Springer-Verlag, New York, 1995.

[Hen82] R. Henriksen. “The Truncated Second-Order Nonlinear Filter Revisited.” *IEEE Transactions on Automatic Control*, **27**(1):247–251, 1982.

[HES12] M.S. Hemati, J.D. Eldredge, and J.L. Speyer. “Aircraft Wake Sensing.” In *AIAA Paper 2012-4768*, AIAA Guidance, Navigation, and Control Conference, Minneaplis, MN, August 2012.

[HES13a] M.S. Hemati, J.D. Eldredge, and J.L. Speyer. “Aircraft Wake Sensing.” Submitted to *Journal of Guidance, Control, and Dynamics*, 2013.

[HES13b] M.S. Hemati, J.D. Eldredge, and J.L. Speyer. “Improving Vortex Models via Optimal Control Theory.” In *AIAA Paper 2013-0351*, 51st AIAA Aerospace Sciences Meeting, Grapevine, TX, January 2013.

[HLB97] P.J. Holmes, J.L. Lumley, G. Berkooz, J.C. Mattingly, and R.W. Wittenberg. “Low-Dimensional Models of Coherent Structures in Turbulence.” *Physics Reports*, **187**:337–384, 1997.

[HLB12] P. Holmes, J.L. Lumley, G. Berkooz, and C.W. Rowley. *Turbulence, Coherent Structures, Dynamical Systems, and Symmetry.* Cambridge University Press, Cambridge, second edition, 2012.

[HYK02] M. Harris, R.I. Young, F. Köpp, A. Dolfi, and J.-P. Cariou. "Wake Vortex Detection and Monitoring." *Journal of Aerospace Science and Technology*, **6**:325–331, 2002.

[Ian02] B. Iannotta. "Vortex Draws Flight Research Forward." *Aerospace America*, **40**(3):26–30, March 2002.

[IG97a] K. Ide and M. Ghil. "Extended Kalman Filtering for Vortex Systems. Part I: Methodology and Point Vortices." *Dynamics of Atmospheres and Oceans*, **27**:301–332, 1997.

[IG97b] K. Ide and M. Ghil. "Extended Kalman Filtering for Vortex Systems. Part II: Rankine Vortices and Observing-System Design." *Dynamics of Atmospheres and Oceans*, **27**:333–350, 1997.

[Jan04] J. Janssen. *Lateral Line Sensory Ecology.* The Senses of Fish: Adaptations for the Reception of Natural Stimuli. Kluwer Academic Publishers, Dordrecht, The Netherlands, 2004.

[Jaz07] A.H. Jazwinski. *Stochastic Processes and Filtering Theory.* Dover Publications, Mineola, NY, 2007.

[Jon40] R.T. Jones. "The Unsteady Lift of a Wing of Finite Aspect Ratio." Technical Report 681, NACA, 1940.

[Jon03] M.A. Jones. "The Separated Flow of an Inviscid Fluid around a Moving Flat Plate." *Journal of Fluid Mechanics*, **496**:405–441, 2003.

[JP00] K.D. Jones and M.F. Platzer. "Flapping-Wing Propulsion for Micro Air Vehicle." In *AIAA Paper 2000-0897*, 38th AIAA Aerospace Sciences Meeting, Reno, NV, January 2000.

[Kal60] R.E. Kalman. "A New Approach to Linear Filtering and Prediction Theory." *Transactions of the ASME, Series D: Journal of Basic Engineering*, **82**:35–45, 1960.

[Kar80] K. Karamcheti. *Principles of Ideal-Fluid Aerodynamics.* Wiley, New York, 1980.

[KB07] J. Kim and T.R. Bewley. "A Linear Systems Approach to Flow Control." *Annual Review of Fluid Mechanics*, **39**:383–417, 2007.

[KIJ03] L. Kuznetsov, K. Ide, and C.K.R.T. Jones. "A Method for Assimilation of Lagrangian Data." *Monthly Weather Review*, **131**:2247–2260, 2003.

[Kir04] D.E. Kirk. *Optimal Control Theory: An Introduction.* Dover Publications, Mineola, NY, 2004.

[KP01] J. Katz and A. Plotkin. *Low-Speed Aerodynamics.* Cambridge University Press, New York, second edition, 2001.

[Kra91] R. Krasny. "Vortex Sheet Computations: Roll-Up, Wakes, Separation." In C. Greengard C.R. Anderson, editor, *Lectures in Applied Mathematics*, volume 28, pp. 385–402. Applied Mathematical Society, 1991.

[Kro84] I. Kroo. "A General Approach to Multiple Lifting Surface Design and Analysis." AIAA-84-2507, October 1984.

[Kro01] I. Kroo. "Drag Due to Lift: Concepts for Prediction and Reduction." *Annual Review of Fluid Mechanics*, **33**:587–617, 2001.

[KS38] T. von Kármán and W.R. Sears. "Airfoil Theory for Non-Uniform Motion." *Journal of the Aeronautical Sciences*, **5**(10):379–390, 1938.

[KW78] J. Katz and D. Weihs. "Behavior of Vortex Wakes from Oscillating Airfoils." *AIAA Journal*, **15**(12):861–863, 1978.

[Lew86] F.L. Lewis. *Optimal Estimation.* John Wiley & Sons, New York, 1986.

[Lew91] R.I. Lewis. *Vortex Element Methods for Fluid Dynamic Analysis of Engineering Systems.* Cambridge University Press, Cambridge, 1991.

[Liu09] Y. Liu. *Fast Multipole Boundary Element Method.* Cambridge University Press, New York, 2009.

[LLN05] O. Lehmann, M. Luchtenburg, B.R. Noack, R. King, M. Morzyński, and G. Tadmor. "Wake Stabilization Using POD Galerkin Models with Interpolated Modes." In *Proceedings of the 44th IEEE Conference on Decision and Control, and the European Control Conference*, Seville, Spain, December 2005.

[Loh01] R. Lohner. *Applied CFD Techniques: An Introduction Based on Finite Element Methods.* John Wiley & Sons, West Sussex, England, 2001.

[LTL06] M. Luchtenburg, G. Tadmor, O. Lehmann, B.R. Noack, R. King, and M. Morzyński. "Tuned POD Galerkin Models for Transient Feedback Regulation of the Cylinder Wake." In *AIAA Paper 2006-1407*, 44th AIAA Aerospace Sciences Meeting, Reno, NV, January 2006.

[Mar01] J.S. Marshall. *Inviscid Incompressible Flow.* John Wiley & Sons, New York, 2001.

[Mar03] L. Marino. "A Simple Model Revisited for Wing-Wings and Wings-Ground Interference Problems.", June 2003.

[MAR11] Z. Ma, S. Ahuja, and C.W. Rowley. "Reduced Order Models for Control of Fluids Using the Eigensystem Realization Algorithm." *Theoretical and Computational Fluid Dynamics*, **25**(1):233–247, 2011.

[May79] P.S. Maybeck. *Stochastic Models, Estimation, and Control*, volume 1. Academic Press, New York, 1979.

[Mil73] L.M. Milne-Thompson. *Theoretical Aerodynamics.* Dover Publications, New York, fourth edition, 1973.

[Mil96] L.M. Milne-Thomson. *Theoretical Hydrodynamics.* Dover Publications, New York, 1996.

[Mor84] J. Moran. *Introduction to Theoretical and Computational Aerodynamics.* John Wiley & Sons, New York, 1984.

[MS09] S. Michelin and S.G. Llewelyn Smith. "An Unsteady Point Vortex Method for Coupled Fluid-Solid Problems." *Theoretical and Computational Fluid Dynamics*, **23**:127–153, 2009.

[NAM03] B.R. Noack, K. Afanasiev, M. Morzyński, G. Tadmor, and F. Thiele. "A Hierarchy of Low-Dimensional Models for the Transient and Post-Transient Cylinder Wake." *Journal of Fluid Mechanics*, **497**:335–362, 2003.

[NK94] M. Nitsche and R. Krasny. "A Numerical Study of Vortex Ring Formation at the Edge of a Circular Tube." *Journal of Fluid Mechanics*, **276**:139–161, 1994.

[NMT04] B.R. Noack, I. Mezić, G. Tadmor, and A. Banaszuk. "Optimal Mixing in Recirculation Zones." *Physics of Fluids*, **16**(4):867–888, 2004.

[NMT11] B.R. Noack, M. Morzyński, and G. Tadmor, editors. *Reduced-Order Modelling for Flow Control.* CISM Courses and Lectures 528. Springer, 2011.

[OG92] I. Olwi and M. Ghazi. "Effect of Wing Tip Vortices on Trailing Aircraft." *AIAA Journal*, **30**(9):2186–2187, September 1992.

[Pan05] R.L. Panton. *Incompressible Flow.* John Wiley & Sons, Hoboken, NJ, third edition, 2005.

[PCC01] R.D. Prabhu, S.S. Collins, and Y. Chang. "The Influence of Control on Proper Orthogonal Decomposition of Wall-Bounded Flows." *Physics of Fluids*, **13**(2):502–537, 2001.

[Pis37] E. Pistolesi. "Considerations Respecting the Mutual Influence Systems of Aerofoils." In *Collected Lectures of the 1937 Principal Meeting of the Lilienthal Society*, Berlin, 1937.

[PL98] B. Podvin and J. Lumley. "Reconstructing the Flow in the Wall Region from Wall Sensors." *Physics of Fluids*, **10**(5):1182–1190, 1998.

[Pre98] S. Preidikman. *Numerical Simulations of Interactions Among Aerodynamics, Structural Dynamics, and Control Systems.* PhD thesis, Virginia Polytechnic Institute and State University, 1998.

[Pro08] B. Protas. "Vortex Dynamics Models in Flow Control." *Nonlinearity*, **21**(9):R204–R250, 2008.

[PT34] L. Prandtl and O.G. Tietjens. *Fundamentals of Hydro- and Aeromechanics.* Dover Publications, New York, 1934.

[PW04] D.I. Pullin and Z.J. Wang. "Unsteady Forces on an Accelerating Plate and Application to Hovering Insect Flight." *Journal of Fluid Mechanics*, **509**:1–21, 2004.

[PYJ06] S. Pandya, Y. Yang, D.L. Jones, J. Engel, and C. Liu. "Multisensor Processing Algorithms for Underwater Dipole Localization and Tracking Using MEMS Artificial Lateral-Line Sensors." *EURASIP Journal on Applied Signal Processing*, **2006**:1–8, 2006.

[RAG04] B. Ristic, S. Arulampalam, and N. Gordon. *Beyond the Kalman Filter: Particle Filters for Tracking Applications.* Artech House, Boston, 2004.

[RCM03] C.W. Rowley, T. Colonius, and R.N. Murray. "Model Reduction for Compressible Flows Using POD and Galerkin Projection." *Physica D: Nonlinear Phenomena*, **189**(1–2):115–129, 2003.

[RCV02] R.J. Ray, B.R. Cobleigh, M.J. Vachon, and C. St. John. "Flight Test Techniques Used to Evaluate Performance Benefits During Formation Flight." Technical Report NASA/TP-2002-210730, NASA Dryden Flight Research Center, Edwards, CA, August 2002.

[RDJ07] R.J. Rodenhiser, W.W. Durgin, and H. Johari. "Ultrasonic Method for Aircraft Wake Vortex Detection." *Journal of Aircraft*, **44**(3):726–732, May–June 2007.

[RG12] K. Ramesh and A. Gopalarathnam. "Theoretical Modeling of Leading Edge Vortices Using the Leading Edge Suction Parameter." In *AIAA Paper 2012-3027*, 30th AIAA Applied Aerodynamics Conference, New Orleans, LA, June 25–28 2012.

[RLH03] D. Rutishauser, G. Lohr, D. Hamilton, R. Powers, B. McKissick, C. Adams, and E. Norris. *Wake Vortex Advisory System (WakeVAS) Concept of Operations.* NASA TM-2003-212176, April 2003.

[Ros31] L. Rosenhead. "The Formation of Vortices from a Surface of Discontinuity." *Proceedings of the Royal Society of London. Series A, Containing Papers of a Mathematical and Physical Character*, **134**(823):170–192, 1931.

[Ros99] V.J. Rossow. "Lift-Generated Vortex Wakes of Subsonic Transport Aircraft." *Progress in Aerospace Sciences*, **35**(6):507–660, August 1999.

[Row05] C.W. Rowley. “Model Reduction for Fluids Using Balanced Proper Orthogonal Decomposition.” *International Journal of Bifurcation and Chaos*, **15**(3):997–1013, 2005.

[RS10] J.J. Ryan and J.L. Speyer. “Peak-Seeking Control Using Gradient and Hessian Estimates.” In *Proceedings of the American Control Conference*, pp. 611–616, Baltimore, MD, June 2010. IEEE.

[Rub00] W.L. Rubin. “Radar-Acoustic Detection of Aircraft Wake Vortices.” *Journal of Atmospheric and Oceanic Technology*, **17**:1058–1065, August 2000.

[Saf92] P.G. Saffman. *Vortex Dynamics*. Cambridge University Press, Cambridge, 1992.

[Sar94] T. Sarpkaya. “Vortex Element Methods for Flow Simulation.” In J.W. Hutchinson and T.Y. Wu, editors, *Advances in Applied Mechanics*, volume 31, pp. 113–247. Academic Press, San Diego, 1994.

[SC03] T. Suzuki and T. Colonius. “Inverse-Imaging Method for Detection of a Vortex in a Channel.” *AIAA Journal*, **41**(9):1743–1751, September 2003.

[SC08] J.L. Speyer and W.H. Chung. *Stochastic Processes, Estimation, and Control Theory*. SIAM, Philadelphia, 2008.

[SE07] R.K. Shukla and J.D. Eldredge. “An Inviscid Model for Vortex Shedding from a Deforming Body.” *Theoretical and Computational Fluid Dynamics*, **21**:343–368, 2007.

[Sim06] D. Simon. *Optimal State Estimation: Kalman, H_∞, and Nonlinear Approaches*. John Wiley & Sons, Hoboken, NJ, 2006.

[SJ10] J.L. Speyer and D.H. Jacobson. *Primer on Optimal Control Theory*. SIAM, Philadelphia, 2010.

[SJD03] R. Stuijs, G. Jonville, D. Darracq, and R. Heinrich. “Inviscid Computation of Effect of Wake Vortices on a Scale-Model Airplane.” *Journal of Aircraft*, **40**(1):100–109, January–February 2003.

[Smi90] A.M.O. Smith. *Applied Computational Aerodynamics*, volume 125 of *Progress in Astronautics and Aeronautics*. AIAA, Washington, D.C., 1990.

[Sor70] H.W. Sorenson. “Least-Squares Estimation: From Gauss to Kalman.” *IEEE Spectrum*, **7**:63–68, 1970.

[Spa98] P.R. Spalart. “Airplane Trailing Vortices.” *Annual Review of Fluid Mechanics*, **30**:107–138, 1998.

[SR10] I.N. Smalikho and S. Rham. “Lidar Investigations of the Effects of Wind and Atmospheric Turbulence on an Aircraft Wake Vortex.” *Journal of Atmospheric and Oceanic Optics*, **23**(2):137–146, 2010.

[TH13] H.E. Taha and M.R. Hajj. “Unsteady Nonlinear Aerodynamics of Hovering MAVs/Insects.” In *AIAA Paper 2013-0504*, 51st AIAA Aerospace Sciences Meeting, Grapevine, TX, January 7–10 2013.

[The35] T. Theodorsen. “General Theory of Aerodynamic Instability and the Mechanism of Flutter.” Technical Report 496, NACA, 1935.

[Thu10] K. Thuloweit. “Formation Flight System Keeps C-17s in Line.” Official Website of Edwards Air Force Base [online], 22 September 2010. [retrieved 23 September 2010].

[TLN11] G. Tadmor, O. Lehmann, B.R. Noack, L. Cordier, J. Delville, J-.P. Bonnet, and M. Morzyński. “Reduced-Order Models for Closed-Loop Wake Control.” *Philosophical Transactions of the Royal Society A*, **369**:1513–1524, 2011.

[TN11] G. Tadmor and B.R. Noack. “Bernoulli, Bode, and Budgie.” *IEEE Control Systems Magazine*, **31**(2):18–23, 2011.

[VM02] D. Vainchtein and I. Mezić. “Control of a Vortex Pair Using a Weak External Flow.” *Journal of Turbulence*, **3**(51):2–7, 2002.

[VRW02] M.J. Vachon, R.J. Ray, K.R. Walsh, and K. Ennix. “F/A-18 Aircraft Performance Benefits Measured During Autonomous Formation Flight Project.” AIAA-2002-4491, August 2002.

[Wag25] H.A. Wagner. “Über die Entstehung des dynamischen Auftriebes von Tragflügeln.” *Zeitschrift für Angewandte Mathematik und Machanik*, **5**(1):17–35, 1925.

[WCD05] G. Winckelmans, R. Cocle, L. Dufresne, and R. Capart. “Vortex Methods and their Application to Trailing Wake Vortex Simulations.” *Comptes Rendus Physique*, **6**:467–486, 2005.

[WE12] C. Wang and J.D. Eldredge. “Low-Order Phenomenological Modeling of Leading-Edge Vortex Formation.” *Theoretical and Computational Fluids Dynamics*, August 2012.

[Wil06] D.J. Willis. *An Unsteady, Accelerated, High Order Panel Method with Vortex Particle Wakes*. PhD thesis, Massachusetts Institute of Technology, 2006.

[WM03] Z. Wang and D.T. Mook. “Numerical Aerodynamic Analysis of Formation Flight.” AIAA-2003-610, January 2003.

[WMZ06] J.-Z. Wu, H.-Y. Ma, and M.-D. Zhou. *Vorticity and Vortex Dynamics*. Springer, Berlin, 2006.

[WPB07] D.J. Willis, J. Peraire, and K.S. Breuer. “A Computational Investigation of Bio-Inspired Formation Flight and Ground effect.” In *AIAA Paper 2007-4182*, 25th AIAA Applied Aerodynamics Conference, Miami, FL, June 25–28 2007.

[WPW07] D.J. Willis, J. Peraire, and J.K White. “A Combined pFFT-Multipole Tree Code, Unsteady Panel Method with Vortex Particle Wakes.” *International Journal for Numerical Methods in Fluids*, **53**:1399–1422, 2007.

[XA04] X. Xu and P.J. Antsaklis. “Optimal Control of Switched Systems Based on Parameterization of the Switching Instants.” *IEEE Transactions on Automatic Control*, **49**(1):2–16, January 2004.

[YCE06] Y. Yang, J. Chen, J. Engel, S. Pandya, N. Chen, C. Tucker, S. Coombs, D.L. Jones, and C. Liu. “Distant Touch Hydrodynamic Imaging with an Artificial Lateral Line.” *PNAS*, **103**(50):18891–18895, 2006.